

**MEASURING NEUTRON-TRANSFER REACTIONS  
WITH FAST MASS $\approx$ 80 BEAMS TO REDUCE  
UNCERTAINTIES IN SPECTROSCOPIC FACTORS**

by

**HARRISON ELLIS SIMS**

A dissertation submitted to the

**School of Graduate Studies**

**Rutgers, The State University of New Jersey**

In partial fulfillment of the requirements

For the degree of

**Doctor of Philosophy**

**Graduate Program in Physics and Astronomy**

Written under the direction of

**Jolie A. Cizewski**

and approved by

---

---

---

---

**New Brunswick, New Jersey**

**January, 2021**

## ABSTRACT OF THE DISSERTATION

# Measuring neutron-transfer reactions with fast mass $\approx$ 80 beams to reduce uncertainties in spectroscopic factors

By Harrison Ellis Sims

Dissertation Director:

Jolie A. Cizewski

Neutron-transfer reactions with radioactive-ion beams (RIBs) probe the single-neutron components of the nuclear wave function, which are needed to deduce the direct semi-direct (DSD) component of neutron capture cross sections. With  $N=50$ ,  $^{84}\text{Se}$  is near the (weak)  $r$ -process path of nucleosynthesis, where unknown neutron-capture cross sections (expected to be dominated by DSD capture) can affect calculations of abundances. With (d,p) reactions, spectroscopic factors can be deduced by comparing experimental differential cross sections to those calculated using nuclear reaction theory. However, deduced spectroscopic factors are heavily dependent on the radius and diffuseness parameters chosen to model the single-particle bound-state potential. Using a combined method with low- and high-energy RIBs, both a peripheral and more central probe of the nucleus can constrain the single-particle asymptotic normalization coefficient (spANC) - reducing the uncertainties on the extracted spectroscopic factors. Using

this method for the first time with a heavy, neutron-rich RIB, the spectroscopic factors of low-lying states in  $^{85}\text{Se}$  have been studied through the  $^{84}\text{Se}(d,p)$  reaction. The high-energy measurement at 45 MeV/u was performed at the National Superconducting Cyclotron Laboratory, where the Oak Ridge Rutgers University Barrel Array (ORRUBA) and the Silicon Detector ARray (SIDAR) were used to detect reaction protons in coincidence with heavy-ion recoils analyzed by the S800 spectrograph. The low-energy (4.5 MeV/u) measurement was previously measured by Thomas *et al.* [Tho07] at the Holifield Radioactive Ion Beam Facility, where spectroscopic factors were extracted without a constraint on the bound-state parameters. With the combined analysis of the low- and high-energy measurements, single-particle ANCs were constrained for the  $5/2^+$  ground state and  $1/2^+$  first excited state, and spectroscopic factors were deduced to be  $0.28 \pm 0.05$  and  $0.26 \pm 0.07$  for these states, respectively. The deduced spectroscopic factors were then used as input for DSD neutron-capture cross section calculations at astrophysical energies.

The study of  $N \approx 50$  isotopes will be continued with the  $N=48$  isotope  $^{80}\text{Ge}$ . Preparation for the priority-one approved measurement of  $^{80}\text{Ge}(d,p)$  at 45 MeV/u is discussed, which is to be directly compared to a previous measurement at 3.875 MeV/u by Ahn *et al.* [Ahn19] through the combined method. The analysis of the low energy data for a range of bound-state geometries is also presented.

Looking to the future, work to prepare for the Facility for Rare Isotope Beams (FRIB, currently under construction) is presented, including a new design for the Gamma-array - ORRUBA: Dual Detectors for Experimental Structure Studies (GODDESS) setup. This will provide the opportunity to measure spectroscopic factors even further from stability.

## Acknowledgements

I consider myself very fortunate to be surrounded by the overwhelming support and love that exists in my life. This dissertation is dedicated to everyone that has filled my life with love, happiness and purpose.

To my wonderful soon-to-be-wife, Charlotte, thank you. Your unwavering love and kindness fills me with joy everyday. Your dedication and support for me (even when I'm endlessly on travel!) gave me the strength to never give up. I couldn't have done this without you!

My parents: Mum, Dad and Jan, thank you for always believing in me, and encouraging me to be the best that I can be. Growing up, you have only ever been examples of the persevering, hard-working, and warm-hearted person that I aspire to be.

My thanks also go to David Walter, who proposed, setup, and ran the experiment that I have analyzed for my PhD. You're always more than happy to help and give great advice, thank you!

My Oak Ridge advisor, Steve Pain, thank you (and sorry for!) for my endless intrusions into your office for a quick five minutes (which inevitably turn into two hours...). Thank you for mentoring me through my graduate career, from my Surrey-student days through to the end of my PhD, you have been there every step. Thank you for your perpetual help!

To the entire “Rutgers Team”, who have been there with me on never-ending experiments, thank you! Thank you for being such wonderful friends and colleagues, even when we are working forty-something hour shifts together!

Thanks go also to Goran Arbanas, for giving excellent advise and help in calculating direct neutron capture cross sections using CUPIDO.

Finally, my thanks go to my advisor, Jolie Cizewski. Thank you for believing in me, and giving me the opportunity to to be on the front line of physics! You have always fought in my corner, and made sure I have had every opportunity to succeed.

# Table of Contents

<b>Abstract</b> . . . . .	ii
<b>Acknowledgements</b> . . . . .	iv
<b>List of Tables</b> . . . . .	viii
<b>List of Figures</b> . . . . .	xi
<b>1. Introduction</b> . . . . .	1
1.1. Nuclear Structure . . . . .	2
1.2. The r process . . . . .	7
1.3. Goals of this study . . . . .	12
1.4. Structure of the dissertation . . . . .	14
<b>2. Theory</b> . . . . .	16
2.1. Reaction formalisms . . . . .	17
2.1.1. Distorted Wave Born Approximation . . . . .	17
2.1.2. Adiabatic Wave Approximation . . . . .	18
2.1.3. FRESCO parameters . . . . .	21
2.2. The optical model . . . . .	23
2.3. Asymptotic normalization coefficients . . . . .	26
2.4. The combined method . . . . .	30

<b>3.</b>	<b><math>^{84}\text{Se}(\text{d,p})^{85}\text{Se}</math></b>	<b>34</b>
3.1.	$^{84}\text{Se}(\text{d,p})^{85}\text{Se}$ at 45 MeV/u	35
3.1.1.	Inverse kinematics	35
3.1.2.	Beam development, delivery and tracking	38
3.1.3.	Silicon Detectors	41
3.1.4.	S800 mass spectrograph	46
3.1.5.	Data Acquisition	50
3.1.6.	Analysis	51
3.1.7.	Differential cross sections	66
3.2.	$^{84}\text{Se}(\text{d,p})^{85}\text{Se}$ at 4.5 MeV/u	69
3.3.	Constraining the single-particle ANC, $b_{\ell j}$	77
3.3.1.	Expanding the parameter space in $(r_0, a)$	82
3.4.	Direct neutron capture calculations	88
3.5.	Summary	91
<b>4.</b>	<b><math>^{80}\text{Ge}(\text{d,p})^{81}\text{Ge}</math> and preparation for Day-1 FRIB</b>	<b>93</b>
4.1.	$^{80}\text{Ge}(\text{d,p})^{81}\text{Ge}$ at 3.9 MeV/u	94
4.2.	Preparation for $^{80}\text{Ge}(\text{d,p})^{81}\text{Ge}$ at 45 MeV/u	96
4.2.1.	Experimental setup	98
4.2.2.	Simulations	101
4.3.	Coupling ORRUBA with GRETINA and Day-1 FRIB	103
<b>5.</b>	<b>Summary, Conclusions and Future work</b>	<b>110</b>

## List of Tables

2.1. List of parameters, a brief description, and their values used in the FRESKO input file to calculate the differential cross sections for the $^{84}\text{Se}(\text{d},\text{p})$ reaction. A more complete description of the input parameters and their purposes can be found in Reference [Tho09]. . . . .	23
2.2. Koning-Delaroche phenomenological global optical model parameters [Kon03] for the ground state transfer used to construct the adiabatic potential of Johnson and Tandy [Joh74]. . . . .	25
2.3. The same as table 2.2 but for neutron transfer to the first excited state.	25
2.4. Single particle ANCs, $b_{\ell j}$ , for a range of bound state geometries for the ground state and first excited state in $^{85}\text{Se}$ for the reaction $^{84}\text{Se}(\text{d},\text{p})$ at 4.5 MeV/u. The relative spectroscopic factor $\Delta S$ is deduced from equation 2.3, and are normalized to values for $r = 1.25$ and $a = 0.65$ : $\Delta S = b_{\ell j}^2(r_0, a)/b_{\ell j}^2(1.25, 0.65)$ . . . . .	30
3.1. Alpha energies and relative intensities from triple alpha source. . . . .	44
3.2. Extracted solid angles of each E layer detector type, per detector. Uncertainties are approximated using the difference between the Monte Carlo simulation, and the measured alpha particles. . . . .	46
3.3. Resolution and integrated counts per angular bin. Stated uncertainties are purely statistical. . . . .	58

3.4. Experimental normalization parameters . . . . .	65
3.5. Extracted single particle information from the measurement at 4.5 MeV/u for the ground and first excited (0.462 MeV) states in $^{85}\text{Se}$ using DWBA formalism, as in Ref [Tho07]. . . . .	74
3.6. Extracted single particle information from the measurement at 4.5 MeV/u for the ground and first excited (0.462 MeV) states in $^{85}\text{Se}$ using ADWA formalism. Individual fits to the cross sections are used, as well as a fit assuming the ground- and first-excited states are unresolved. . . . .	74
3.7. Extracted spectroscopic factors $S$ and many body ANCs $C_{\ell j}$ calculated using the constrained single-particle ANC $b_{\ell j}$ for the $^{85}\text{Se}$ ground state and first excited (0.462 MeV) state, using both Koning-Delaroche and Chapel Hill optical model parameters. No optical model or bound-state geometry uncertainties are included. . . . .	80
3.8. Final deduced spectroscopic factors for the ground- and first-excited states in $^{85}\text{Se}$ . FR-ADWA calculations were used for both the high- and low-energy data, and the resolved ground- and first-excited states were analyzed for low energy data. Koning-Delaroche optical model pa- rameters are used. Uncertainties include the uncertainty in optical model (calculated using Figures 3.35 and 3.36). . . . .	82
3.9. Deduced radius and diffuseness of the ground- and first-excited (0.462 MeV) state in $^{85}\text{Se}$ from the combined method using proportion- ally varying parameters. . . . .	85

3.10. Extracted spectroscopic factors for the  $5/2^+$  ground state and  $1/2^+$  first-excited state at 0.462 MeV using various analyses. Spectroscopic factors deduced through the combined method, and individually for the 4.5 and 45 MeV/u reactions (using standard bound-state potential parameters) are shown. Both DWBA and ADWA formalisms are used. . . . . 88

## List of Figures

1.1.	Single-particle level diagram derived using the Woods-Saxon potential ( <i>right</i> ). Levels produced with no spin-orbit term, and with a very diffuse surface, are also shown. Taken from Ref. [Dob96]. . . . .	4
1.2.	Observed solar r-process isotopic abundances (dots, deduced as solar abundance minus the calculated s-process abundances), and calculated r-process predictions. Theoretical predictions cover a range of neutron densities, and are for a specific nuclear mass model, ETFSI-Q. Figure taken from [Cow06]. . . . .	9
1.3.	Sensitivity measure (F, on a scale of 1-20) of the final weak r-process abundance pattern on neutron capture rates in the $A \approx 80$ region; stable isotopes are represented by black dots. Fifty-five neutron capture rate studies ran for a range of distinct astrophysical conditions [Sur14]. . . .	10

1.4.	Comparison of calculated neutron-capture cross sections for tin isotopes at 30 keV. Direct-semidirect DSD calculations with experimental energies and spectroscopic factors [Man19] (black diamonds), Hauser-Feshbach model calculations [Chi08] (green squares), Calculated $^{132}\text{Sn}$ direct capture using the theoretical spectroscopic factor [Rau98] (black X) and DSD calculations with theoretical excitation energies and spectroscopic factors (red circles) [Chi08]. $^{124}\text{Sn}$ DSD calculations using spectroscopic factors of Ref. [Tom11] for all $\ell = 1$ levels having $S \geq 0.01$ is given by the blue plus. Figure adopted from Ref. [Man19]. . . . .	11
1.5.	Level schemes of states in $^{84}\text{Se}$ and $^{85}\text{Se}$ below 1.5 MeV. . . . .	13
2.1.	Cartoon of the entrance ( <i>left</i> ) and exit ( <i>right</i> ) channels for a (d,p) reaction. DWBA calculations assume an interaction between the deuteron and the target, while ADWA decomposes the deuteron and therefore the interaction between proton - target and neutron - target. . . . .	18
2.2.	Calculations of the $^{84}\text{Se}(d,p)^{85}\text{Se}(g.s.)$ at 4.5 MeV/u transfer, using FR-ADWA (solid) and DWBA (dashed). DWBA calculations were performed using Lohr and Haeberli [Loh74] OMPs for the deuteron entrance potential, FR-ADWA target-nucleon potentials were taken from Johnson and Tandy [Joh74]. Calculations used either Koning-Delaroche (red) [Kon03] or Chapel Hill (blue) [Var91] OMPs for the proton - $^{85}\text{Se}$ potential. . . . .	20

2.3.	Differential cross sections calculated in the center of mass frame for $^{84}\text{Se}(d,p)^{85}\text{Se}$ . (a) $\ell=2$ transfer to the ground state at 45 MeV/u. (b) $\ell=0$ transfer to the first excited state at 45 MeV/u. (c) $\ell=2$ transfer to the ground state at 4.5 MeV/u. (d) $\ell=0$ transfer to the first excited state at 4.5 MeV/u. Each transfer calculation was run with DWBA using Daehnick deuteron OMPs [Dae80] ( <i>pink</i> ), Local energy approximation - ADWA ( <i>blue</i> ), Zero range - ADWA with Johnson-Soper potential ( <i>red</i> ), and Finite range - ADWA with Johnson-Tandy potential ( <i>green</i> ). All calculations used Koning-Delaroche optical model parameters. Calculations run with TWOFNR [Tos19] and FRESCO [Tho06]. . . . .	22
2.4.	Single-particle wavefunction $\varphi_\ell(r)$ ( <i>blue</i> ), with the tail represented as a spherical Hankel function ( <i>dashed</i> ), normalized by the single-particle ANC $b_{\ell j}$ ( <i>solid</i> ). Adopted from reference [Wal18]. . . . .	26
2.5.	Extracted spectroscopic factor $S$ , and many-body ANC, $C_{\ell j}$ as a function of the single-particle ANC, $b_{\ell j}$ for the reaction $^{86}\text{Kr}(d,p)^{87}\text{Kr}(\text{g.s.})$ at 5.5 MeV/u. Data taken by Haravu <i>et al.</i> [Har70] and analyzed by Walter [Wal18]. . . . .	27
2.6.	Differential cross section calculations as described in section 2.1, using Koning-Delaroche global optical model parameters for the $\ell = 2$ transfer to the ground state in $^{85}\text{Se}$ for a range of bound state geometries, assuming unit spectroscopic factors. Johnson and Tandy [Joh74] potentials are used within the finite-range adiabatic wave approximation formalism. Calculated using FRESCO [Tho06]. . . . .	29

2.7.	(a) Extracted many-body ANCs and (b) spectroscopic factors for a range of single-particle ANCs for the $^{86}\text{Kr}(\text{d},\text{p})$ reaction at 5.5 (red) [Har70] and 35 MeV/u (blue) [Wal19]. FR-ADWA analysis with Koning-Delaroche optical model parameters was used for both energies. Error bars represent experimental systematic uncertainties, uncertainty in the FR-ADWA calculation and also least squares fit to the data with statistical uncertainties. Figure adopted from Ref [Wal19]. . . . .	32
3.1.	3D CAD drawing of the experiment setup. Beam direction is left to right, MCPs located upstream of the target, followed by SIDAR and ORRUBA. Downstream of the target, two ORRUBA detectors were deployed to measure elastic scattering. . . . .	35
3.2.	Galilean addition of velocities to boost from the lab frame to the center of mass frame for the reaction $m_p(m_t, m_e)m_R$ in inverse kinematics. Elastic scattering (a) - where $m_p = m_R$ and $m_t = m_e$ - and stripping reactions (b) such as (d,p). The laboratory (blue) and center of mass frame (red, indicated with prime) are both shown. The center of mass velocity is given by $V_{CM}$ , and the scattering angle of the ejectile is given by $\zeta$ . In both cases the heavy beam is incident from the right. . . . .	36
3.3.	ADWA-predicted differential cross sections for the $^{84}\text{Se}(\text{d},\text{p})^{85}\text{Se}(\text{g.s.})$ at 4.5 and 45 MeV/u - demonstrating the boost from the center of mass frame to the laboratory frame. Note that for the high energy reaction, relativistic effects are accounted for. . . . .	37
3.4.	Schematic diagram of the Coupled Cyclotron facility and the A1900 fragment separator at the NSCL. Figure adopted from Reference [Sto05]. . .	39

3.5.	Reconstructed position spectrum using alpha particles incident through a mask onto the MCP face. The “notch” indicates the orientation of the mask. The mask holes are 1mm in diameter, and spaced 2.5mm apart. . . . .	40
3.6.	(Top) 3D rendering of silicon detector setup surrounding target. (Bottom) 2D schematic detailing detector locations upstream of the target. Beam direction is from left to right. . . . .	42
3.7.	Particle Identification Plot (PID) of reaction products seen in one of the SIDAR detectors. $\Delta E$ is the energy deposited in the thin layer and $E$ residual is the energy deposited in the thick layer. Separation by mass is seen of protons, deuterons and tritons. The color scale shows the non-gated spectra of the charged particles detected in SIDAR; events where a coincident $^{85}\text{Se}$ recoil was detected in the S800 are shown in red. . . . .	43
3.8.	(a) Raw response of a single strip on a SIDAR detector to alpha particles from the triple alpha source, and a pedestal run with no detector thresholds for zero-point energy calibration. (b) Linear interpolation of four calibration points for the same detector to convert from ADC channel to incident particle energy [MeV]. Error bars represent the uncertainty in extracting the mean peak positions from the fits to the alpha peaks. . . . .	45
3.9.	Number of alphas per 0.75mm across one ORRUBA detector face recorded ( <i>blue</i> ), and calculated through Monte Carlo ( <i>red</i> ). (a) Downstream ORRUBA barrel, and (b) upstream ORRUBA barrel. . . . .	46

3.10. Simulated magnetic rigidity of the $^{85}\text{Se}$ recoil (red) at the S800 beam blocker. The centroid of the unreacted $^{84}\text{Se}$ beam is shown in purple. Beam-blocker positions to stop the $^{84}\text{Se}$ beam at 1% (blue) and 0.5% (green) momentum dispersions are also shown. Adopted from Reference [Pai18b] . . . . .	48
3.11. (a) Schematic showing the S800 mass spectrograph in relation to the experimental target position. (b) Cartoon of the focal plane detectors deployed [Per20]. . . . .	48
3.12. Energy response of the ion chamber grids (a) uncalibrated, and (b) gain matched relative to each other. . . . .	49
3.13. Logic diagram of the ORRUBA and S800 Data Acquisition (DAQ) setup. Logic signals are denoted by the thin blue lines, whereas the digitized data is represented by the thick green arrows. . . . .	52
3.14. Proton energy spectrum detected in SIDAR with $^{84}\text{Se}$ beam incident on a $\text{CD}_2$ target (blue) and $\text{CH}_2$ target (red). The $\text{CH}_2$ proton energy spectrum was scaled using a linear fit to the $\text{CD}_2$ data between 10 and 14 MeV - a region corresponding to negative excitation energy for $^{84}\text{Se}(\text{d},\text{p})$ protons and therefore a good estimation of the background. Uncertainties in the scaled data are statistical. . . . .	53
3.15. Energy loss in S800 ion chamber vs time of flight between the S800 E1 scintillator and cyclotron RF to provide PID and recoil tagging. The color scale represents all data seen in S800; coincidences with protons seen in ORRUBA and SIDAR are red. . . . .	54

3.16. Energy and angle of protons observed in the silicon detectors in coincidence with a recoil in the S800. A kinematic line of the predicted ground state transfer is overlaid. <i>inset</i> , Q value spectrum from the upstream ORRUBA barrel and SIDAR data. The ground state Q value of 2.312 MeV is highlighted. . . . .	56
3.17. Q value spectra for each angular bin analyzed. The ground state (Q=2.312 MeV) fit (green) and the first excited state (Q=1.85 MeV) (blue) are fit with means and widths fixed according to the VIKAR Monte Carlo simulation. Fits to states at higher excitation energies are also included, such that their yields are not included in fits to the ground- and first-excited states. . . . .	59
3.18. VIKAR Simulated kinematics of $^{84}\text{Se}(d,p)^{85}\text{Se}(\text{g.s.})$ at 45 MeV/u. Input parameters are as follows: Beam spot size = 6mm, Beam divergence = $1^\circ$ , momentum dispersion = 1%. No position reconstruction from beam tracking was used in order to remain consistent with the experiment. . .	60
3.19. Time of flight paths used for beam composition determination. Two time-of-flight paths used: Cyclotron RF - Upstream MCP and XF scintillator - Upstream MCP. Adopted from [Sco16]. . . . .	61
3.20. Time-of-flight between the Upstream MCP and the Cyclotron RF measured against the time of flight between the Upstream MCP and the XF scintillator. The two main beam species identified are $^{84}\text{Se}$ and $^{84}\text{Br}$ . . .	61

3.21. Projection of Figure 3.20 onto diagonal axis to calculate percentage composition of beam species via Gaussian fits. The red line is the total fit, dashed lines show individual contributions of $^{84}\text{Se}$ (blue), $^{84}\text{Br}$ (green) and traces of other unidentified contaminants (cyan, magenta). . . . .	62
3.22. Upstream MCP acquisition “stop” spectrum, where the starts were from an OR of the silicon detectors and both of the MCPs. The large broad peak ( <i>left</i> ) is from the silicon starts, the sharp peak is from the MCP starts. The full scale is $1\ \mu\text{s}$ . . . . .	62
3.23. Total (all beam species) rate as a function of time over the experiment. Uncertainties are statistical, and too small to be seen. . . . .	64
3.24. Q value spectrum in SIDAR for background subtracted particle singles (blue) and S800 coincident events (red). . . . .	66
3.25. Absolute differential cross section as a function of center-of-mass angle for the $^{84}\text{Se}(\text{d,p})^{85}\text{Se}(\text{g.s.})$ reaction at 45 MeV/u (points) with normalized FR-ADWA calculated cross sections for a range of bound-state parameters.	67
3.26. Absolute differential cross section as a function of center-of-mass angle for the $^{84}\text{Se}(\text{d,p})^{85}\text{Se}(\text{1st Ex} - 0.462\ \text{MeV})$ reaction at 45 MeV/u (points) with normalized FR-ADWA calculated cross sections for a range of bound-state parameters. . . . .	68
3.27. Absolute differential cross section for the $^{85}\text{Se}$ ground state (points) with normalized FR-ADWA (red) and DWBA (blue) calculated cross sections for $^{84}\text{Se}(\text{d,p})$ at 4.5 MeV/u. Data taken from Ref [Tho07]. $\chi^2/\text{degree of freedom (DOF)}$ is 1.90 for the DWBA fit, and 6.17 for the ADWA fit. . . . .	70

3.28. Same as Figure 3.27 but for the $^{85}\text{Se}$ first excited state at 0.462 MeV. $\chi^2$ /degree of freedom (DOF) is 4.60 for the DWBA fit, and 1.57 for the ADWA fit. . . . .	71
3.29. Energy - detector strip systematics for $^{84}\text{Se}(d,p)$ at 4.5 MeV/u. Data taken from SIDAR (a) and the S1 detector (b). Figure taken from Ref [Tho07]. . . . .	72
3.30. $^{84}\text{Se}(d,p)$ at 4.5 MeV per nucleon observed differential cross section assuming unresolved ground and first excited (0.462 MeV) states (points). A $\chi^2$ minimization of the total FR-ADWA predicted cross sections to that observed yields the spectroscopic factor for each state. The individual predicted cross sections are also included to show the relative contributions. The red band represents the uncertainty in the deduced spectroscopic factors. . . . .	73
3.31. $\chi^2$ /D.o.F. produced for each combination of spectroscopic factors when fitting the unresolved ground and first excited states. . . . .	75
3.32. (a) $^{84}\text{Se}(d,p)$ transfer to $^{85}\text{Se}$ ground state at 4.5 MeV/u, with normalized FR-ADWA predicted cross sections calculated with a range of bound state geometries. (b) Same as (a), but for the $^{85}\text{Se}$ first excited (0.462 MeV) state. (c) Transfer cross sections to the “unresolved” ground and first excited state, with two-component normalized FR-ADWA predicted cross sections overlaid. The range of $r_0$ , $a$ values used for each analysis is shown in the (a) legend. Data taken from Ref [Tho07]. . . . .	76

3.33. FR-ADWA analysis results for the $^{85}\text{Se}$ $5/2^+$ ground state at 4.5 MeV/u (red) and 45 MeV/u (blue) using Koning-Delaroche optical model parameters for the theoretical calculations. (a) Spectroscopic factors as a function of single particle ANC. (b) Many body ANC as a function of single particle ANC. Error bars in the low energy measurement include the target thickness and fitting uncertainties, but not the uncertainties due to the choice in optical model. The high energy error bars are a combination in quadrature of the systematic uncertainties stated in Table 3.4, and the statistical uncertainty of the fitting analyses. . . . .	78
3.34. Same as Figure 3.33, but for the first excited state in $^{85}\text{Se}$ . . . . .	78
3.35. Comparison of deduced spectroscopic factors, using FR-ADWA calculated cross sections with the resolved low energy data, FR-ADWA fits treating the low energy data as unresolved, and DWBA fits to the individual cross sections for both the low- and high-energy data. These were calculated using both Koning-Delaroche (blue), and Chapel Hill (orange) optical model parameters. . . . .	81
3.36. Same as Figure 3.35, but for the first excited (0.462 MeV) state in $^{85}\text{Se}$ . . . . .	81

3.37. Spectroscopic factor $S_{\ell j}$ , and ANC $C_{\ell j}^2$ surfaces as a function of both bound state radius $r_0$ and diffuseness $a$ parameters for the $^{84}\text{Se}(d,p)^{85}\text{Se}$ ground state ( $5/2^+$ ) reaction. (a) and (b) Spectroscopic factors for the high and low energy reaction respectively. (c) and (d) Many-body ANC for the high and low energy reaction respectively. Where the surfaces of the high- and low-energy reactions cross is given by a red line. The points from the proportionally varying $(r_0, a)$ parameters (shown in Table 2.4, and used to calculate the crossing values in Figure 3.33) are denoted as red triangles. . . . .	83
3.38. Same as Figure 3.37, but for the $^{85}\text{Se}$ first excited state (0.462 MeV). . .	84
3.39. Single-particle ANC $b_{\ell j}$ for the $5/2^+$ ground state as a function of bound state radius parameter $r_0$ . Lines of constant diffuseness are overlaid. The shaded region is the constrained $(r_0, a)$ surface crossing deduced in Figure 3.37, and the black square is the crossing value that is constrained using proportionally varying $(r_0, a)$ parameters, as in Figure 3.33. The uncertainty in the “proportional value” point corresponds to the uncertainty calculated for the constrained $b_{\ell j}$ . . . . .	86
3.40. Same as Figure 3.39, but for the $^{85}\text{Se}$ first excited state (0.462 MeV). . .	86
3.41. Single-particle ANC $b_{\ell j}$ for the $5/2^+$ ground state (color scale) as a function of bound state radius $r_0$ and diffuseness $a$ parameters. The constrained surface between the high and low energy measurements is shown, as well as the $(r_0, a)$ of the extracted spectroscopic factor using the combined method. The uncertainty in the “proportional value” point corresponds to the uncertainty calculated for the constrained $b_{\ell j}$ . . . . .	87

3.42.	Same as Figure 3.41, but for the first excited state. . . . .	87
3.43.	(a) Individual DSD reaction rates for $^{84}\text{Se}(n,\gamma)$ to the $5/2^+$ ground state, using both the canonical (light blue) and newly constrained (dark blue) $(r_0, a)$ parameters (as seen in Table 3.9) for the bound-state potential. (b) The same as (a), but for the $1/2^+$ first excited (0.426 MeV) state - orange is canonical, and red is newly constrained $(r_0, a)$ parameters. (c) Sum of $^{84}\text{Se}$ neutron capture cross sections to the ground- and first excited-states for direct-semi direct capture (orange), and direct capture only (cyan) using the newly constrained values for $(r_0, a)$ . All uncertainties represent the uncertainty in the deduced spectroscopic factors. . . . .	90
4.1.	$^{80}\text{Ge}(d,p)$ transfer cross section to the unresolved doublet at 700 keV compared to FR-ADWA predictions assuming $3s_{1/2}$ and $2d_{5/2}$ configurations for the 679 keV and 711 keV states, respectively. Fits are to the first 5 data points only. Data from [Ahn19]. . . . .	95
4.2.	$^{80}\text{Ge}(d,p)$ transfer cross section to the unresolved doublet at 700 keV compared to FR-ADWA predictions assuming $3s_{1/2}$ and $2d_{5/2}$ configurations for a range of radius and diffuseness parameters. Fits are only to the first 5 data points. . . . .	96
4.3.	Deduced spectroscopic factors and many-body ANCs from the $^{80}\text{Ge}(d,p)$ measurement at 3.787 MeV/u as a function of single-particle ANC for the $1/2^+$ and $5/2^+$ states at 679 keV and 711 keV respectively. . . . .	97

4.4. Proposed setup for the $^{80}\text{Ge}(\text{d},\text{p})$ reaction at 45 MeV/u. ORRUBA and QQQ5 detectors surround the target at backward angles, with two ORRUBA detectors upstream for elastic scattering monitoring. All detectors will be deployed in a dE-E configuration. Beam direction is left to right. . . . .	98
4.5. ( <i>left</i> ) Photograph of Gas Tracking Detector from the beam's perspective (Courtesy of Steve Pain). ( <i>right</i> ) Position reconstruction from wire grid anodes. . . . .	99
4.6. ( <i>Top</i> ) FWHM of the 679 keV state as a function of target thickness for a variety of momentum dispersions with and without beam tracking implemented for the ORRUBA barrels. ( <i>Bottom</i> ) Same as the top, but for the QQQ5 detectors. . . . .	102
4.7. ( <i>Left</i> ) Predicted momentum spread of $^{80}\text{Ge}$ at the target as a function of momentum acceptance, calculated using LISE++. ( <i>Right</i> ) Fraction of expected counts relative to 1% dp/p momentum acceptance and 1 mg/cm <sup>2</sup> target thickness. . . . .	103
4.8. 3D rendering of GODDESS, full view. Beam direction is left to right. GRETINA surrounds ORRUBA inside a new custom scattering chamber, with a custom pipe designed to house gas tracking detectors located immediately upstream. . . . .	107
4.9. 3D rendering of GODDESS, zoomed in on the ORRUBA barrel. Beam direction is left to right. . . . .	107
4.10. Machine-shop drawing of newly designed GODDESS chamber - side view, with connecting flanges and detector mounting ring shown. . . . .	108

4.11. Machine-shop drawing of newly designed GODDESS chamber - cross section view. . . . .	109
4.12. ( <i>Left</i> ) 3D rendering of the custom chamber designed to house gas tracking detectors upstream of the target. ( <i>Right</i> ) Photo of the gas tracking chamber being manufactured using a 5-axis machine at the University of Tennessee. . . . .	109

# Chapter 1

## Introduction

Understanding the origin of the elements in our universe has been a continual goal of the scientific community. From the synthesis of the lightest elements during the Big Bang, to the violent explosive stellar phenomena forming the heaviest and most exotic elements; our ambition to discover our place in the universe has driven us to probe the most extreme environments. The synthesis of elements heavier than iron occurs predominantly via neutron capture reactions and subsequent beta decays. Approximately half of these owe their existence to the *rapid* neutron capture process (r-process). Recently, the observation of gravitational waves and gamma-ray bursts in coincidence from neutron-star mergers has provided the first direct piece of evidence that these may be a site for the main r-process [Pia17; Abb17]. Indeed, subsequent observations of the resulting kilonova from GW170817 showed strong rare-earth element signatures.

The r-process proceeds from a seed nucleus, up the extreme neutron-rich side of the nuclear landscape. Neutron rich ( $> 10^{20}$  neutrons/cm<sup>3</sup>) environments cause nuclei to capture neutrons more frequently than they  $\beta$  decay back to stability, resulting in the *rapid* synthesis of unstable nuclei. Once the available neutrons have been exhausted,  $\beta$  decay begins to dominate over neutron capture and the radioactive nuclei decay back towards stability.

The short-lived nature of neutron-rich nuclei introduces tremendous challenges to

our understanding of their nucleosynthesis, as they cannot effectively be made into robust targets. The advancement of modern accelerator facilities means that we are able to produce some of these exotic nuclei as radioactive ion beams (RIBs), enabling measurements of their structure and spectroscopic information. Heavier, and more neutron-rich elements however are still not producible at the required intensities, meaning that models in these regions still rely on extrapolation.

## 1.1 Nuclear Structure

For the last 100 years, the structure of the nucleus has been examined through the lens of nuclear reactions [Rut19]. One-nucleon transfer reactions, in particular, are excellent probes into the single-particle nature of specific states of interest. The probability of transferring a single nucleon via a direct reaction is directly proportional to the spectroscopic factor (a measure of how single-particle-like the state is) of the discrete state that the reaction is populating (or removing from, for pickup reactions). Understanding the single-particle nature of neutron-rich nuclei, especially around closed shells, is therefore important to our goal of informing neutron capture rates for r-process nucleosynthesis.

The emergence of single-particle structure stems directly from the formalism of protons and neutrons occupying discrete orbitals: the Shell Model. Evidence for nuclear shell structure is seen through emerging patterns in observables such as natural abundances, the binding energy of valence nucleons [Joh04] and the excitation energy of the first  $2^+$  state in even-even nuclei [For53]. These patterns indicate stability for a particular “magic” number of protons and neutrons: 2, 8, 28, 50, 82 and 126 [May55].

The fermionic properties of protons and neutrons are responsible for the structure of the nucleus - without the Pauli exclusion principle, nucleons could never form into

structured objects. This is the same principle applied to the atomic structure of electrons, giving rise to electron orbitals, where closed-shell atoms are noble gases. There is, however, a dramatic difference between the two phenomena; the Schrödinger equation can generally be solved for atomic orbitals, due to the fact that an external force is applied to them - the nucleus' attractive Coulomb force. Nuclear shell structure arises from the strong force of *other* nucleons. This becomes an increasingly difficult many-body problem as we increase the number of nucleons present. The complex many-body potential can, however, be modelled to give an approximate mean-field potential using effective interactions, provided *and* experienced by the nucleons.

As a first approximation, the harmonic oscillator is used to demonstrate the closed shells, and the degeneracy that exists in each state. The degeneracy of each state is governed by the Pauli exclusion principle; once all the possible spin and angular momentum configurations are occupied for an energy level, no more can be added. This produces magic numbers that replicate those observed in nature for the first 3 shell closures (2, 8, 20), but deviates at higher nucleon numbers. Including a more realistic potential, along with spin-orbit coupling, is necessary to reproduce the observed shell closures. The Woods-Saxon potential is significantly more appropriate in replicating the mean field of the nuclear potential. It does not require an infinite amount of energy to remove a nucleon, and closely mimics the nuclear charge and mass distribution, falling to zero at large radii. The potential is given by:

$$V(r) = \frac{-V_0}{1 + e^{\frac{(r-R)}{a}}} \quad (1.1)$$

Here, the mean radius is approximated as  $R = r_0 \times A^{1/3}$ fm, and the diffuseness of the potential is  $a$ . The values chosen for these parameters depend on the nucleus;

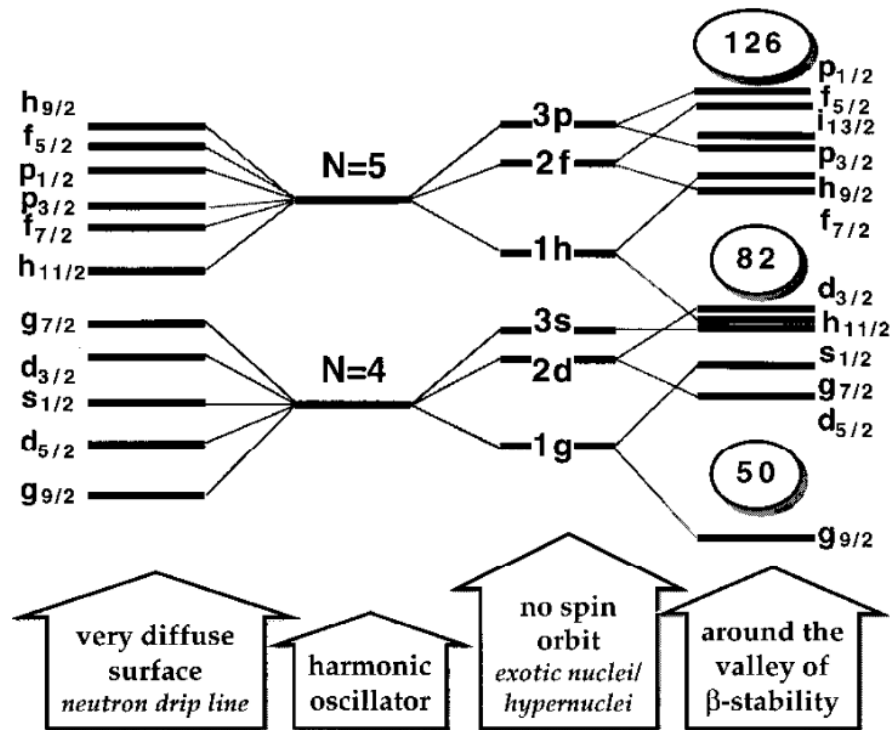


Figure 1.1: Single-particle level diagram derived using the Woods-Saxon potential (*right*). Levels produced with no spin-orbit term, and with a very diffuse surface, are also shown. Taken from Ref. [Dob96].

commonly used values are  $r_0 = 1.25$  fm and  $a = 0.65$  fm. Figure 1.1 shows the level spacing for the Woods-Saxon potential, with and without spin-orbit coupling. The spin-orbit term introduces a splitting of the single particle levels according to their total angular momentum. The correct magic numbers are reproduced when the appropriate underlying physics is taken into account.

That all nuclei with even numbers of neutrons and protons have  $0^+$  ground states and most have  $2^+$  first excited states, suggests that the pairing of nucleons is important in configuring the many-body wavefunction of discrete states. The observed properties of discrete states are generally constructed as a mixing of shell-model configurations, not purely a single one. The spectroscopic factor,  $S$ , is a measure of the single-particle strength in a particular state. Formally defined, this is the square of the normalization of the radial overlap function between a nuclear state, and a valence nucleon coupled to the core nucleus.

Transferring a neutron to a “core” nucleus  $A$  to form a composite nucleus  $B = A + \nu$  through the reaction  $A(d,p)B$ , we define the core in state  $I_A$  to have a wavefunction  $\Phi_{I_A}^A(\xi_A)$ , and the composite nucleus in state  $I_B$  to have  $\Phi_{I_B}^B(\xi_A, \mathbf{r})$ , where  $(\xi_A, \mathbf{r})$  is the core + neutron coordinates. The single-particle overlap function  $\phi_{I_A:I_B}(\mathbf{r})$  can then be calculated as [Tho09]:

$$\phi_{I_A:I_B}(\mathbf{r}) = \langle \Phi_{I_A}^A(\xi_A) | \Phi_{I_B}^B(\xi_A, r) \rangle \quad (1.2)$$

Each state in the composite nucleus  $B$  can be constructed as a superposition over all mutually orthogonal core states with the corresponding overlap function:

$$\Phi_{I_B}^B(\xi_A, \mathbf{r}) = \sum_{I_A} \phi_{I_A:I_B}(\mathbf{r}) \Phi_{I_A}^A(\xi_A) \quad (1.3)$$

These overlap functions are not individually normalized, rather that their summation over all core states is normalized. Let the radial part of the overlap function be defined as  $u_{\ell_j}^{IAIB}$ . Each individual radial overlap function can then be written as a product of a normalized radial wavefunction  $\nu_{\ell_j}^{IAIB}$  and a *spectroscopic amplitude*,  $A_{\ell_j}^{IAIB}$ .

$$u_{\ell_j}^{IAIB} = A_{\ell_j}^{IAIB} \nu_{\ell_j}^{IAIB} \quad (1.4)$$

The spectroscopic factor is then the square modulus of the spectroscopic amplitude.

$$S_{\ell_j}^{IAIB} = |A_{\ell_j}^{IAIB}|^2 \quad (1.5)$$

This represents a measure of how much a state in the nucleus  ${}^A X$  resembles a closed core plus a nucleon  ${}^{A-1} X + \nu$ . A purely single-particle state would exhibit a spectroscopic factor of unity, while any fragmentation into other degrees of freedom yields a spectroscopic factor less than one. Pure single-particle states are generally observed in nuclei which are one nucleon above being magic (or indeed doubly magic [Jon11]), as the closed shell acts as an inert core for the valence nucleon.

Single-particle motion, however, is not the only contributor to the properties of nuclear states. Collective vibrations and rotations of nucleons within the nucleus must be included. As opposed to the single-particle states, which are a result of the valence nucleon properties, these excitations are attributed to the collective motions of mostly surface nucleons within the nucleus. Nuclei near closed shells are generally spherical in shape, such that their collective behavior is vibrational in nature. Nuclei further from shell closures begin to exhibit deformations in their shape, and so rotational excitations must also be considered. Nuclei generally owe their individual structure to both collective and single-particle motion.

The predictive power of the shell model is greatest for stable nuclei, due to the abundance of data that constrains models in this region. The lack of constraints on nucleon interactions in nuclei further from stability (particularly away from shell closures) inhibits the shell model from predicting the single-particle structure in all regions of the nuclear chart. The large valence spaces of single-particle states needed to model heavy, neutron-rich nuclei also restricts shell model calculations. Of particular importance to the goals of this work is the evolution of shell structure as we move away from stability, and towards more exotic, neutron-rich nuclei. Figure 1.1 presents one such prediction for a very diffuse surface at the neutron drip line [Dob96].

An excellent example of shell structure away from stability is the doubly magic  $^{132}\text{Sn}$ , with  $Z=50$  and  $N=82$ . Jones *et al.* investigated the single-particle configuration of  $^{133}\text{Sn}$  via a (d,p) reaction on an unstable beam of  $^{132}\text{Sn}$  [Jon10]. By populating the single-particle states just above the neutron shell closure, information on the robustness of the doubly-closed core can be extracted. The spectroscopic factors of the low-lying states in  $^{133}\text{Sn}$  were all found to be unity within uncertainties, demonstrating that  $^{133}\text{Sn}$  can be modelled as an inert  $^{132}\text{Sn}$  core, plus a valence neutron.

## 1.2 The r process

The r-process is responsible for synthesizing approximately half of the elements heavier than iron. At early stages in the r-process, large neutron-capture rates can build up neutron-rich isotopes to the point along an isotopic chain at which photo-disintegration rates compete with neutron capture [Qia03]. The decrease in neutron separation energy observed in closed-shell-plus-one nuclei ( $\approx 3\text{-}4$  MeV) significantly increases photo-disintegration rates, meaning that points of  $(n,\gamma) \rightleftharpoons (\gamma,n)$  equilibrium accumulate

around closed shells. Once the ratio of free neutrons to seed nuclei falls below one,  $(n,\gamma) \rightleftharpoons (\gamma,n)$  equilibrium fails and freeze-out occurs, such that the remaining neutron-rich isotopes beta decay back towards stability [Beu08; Arc11; Rol89].

Observing solar abundance patterns has traditionally provided a direct insight into nuclear-synthetic processes. Observed r-process abundance patterns are shown in Figure 1.2. Three distinct peaks, around  $A \approx 80$ , 130 and 195 directly correspond to closed neutron shells at  $N = 50$ , 82 and 126, respectively.

Observations of a large dispersion of  $[\text{Sr}/\text{Ba}]$  (the ratio of observed Sr to Ba abundances) in low metallicity stars suggest more than one astrophysical environment is responsible for populating the  $A \approx 80$  and 130 r-process final abundance peaks [Wan05]. Indeed, a “hot” r-process (thought to occur in core-collapse supernovae) is believed to be responsible for the  $A \approx 80$  abundance peak. The neutrino-driven wind associated with these explosive events is predicted to interact with the supernovae ejecta [Woo94], reducing the amount of r-process nucleosynthesis that can take place and stifling the rapid neutron-capture reactions from proceeding all the way up the nuclear chart. This results in only a *weak* r-process, producing nuclei in the  $A \approx 80$  region, occurring in this environment.

Research into the synthesis of  $A \approx 80$  nuclei is complicated by the limited availability of nuclear physics data on short-lived, radioactive nuclei. Beta decay, photodisassociation and neutron-capture rates of neutron-rich nuclei at astrophysical energies all affect the final r-process abundance patterns. Modelling the final r-process abundance pattern based on these data, and comparing to solar observations, is therefore a useful metric for inferring the sensitivity of the final abundance patterns to the nuclear physics and astrophysics that are used in the models. Figure 1.2 shows the observed

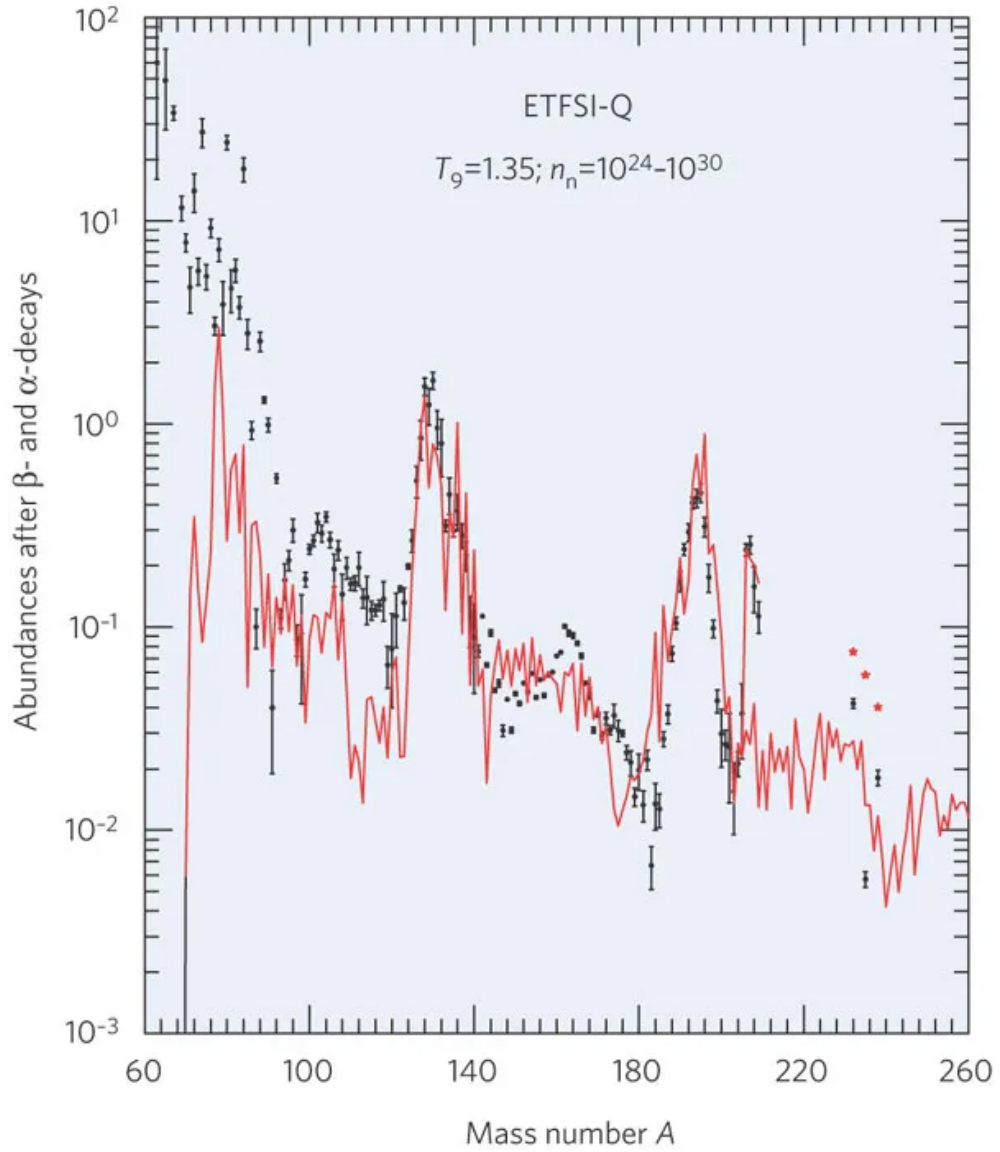


Figure 1.2: Observed solar r-process isotopic abundances (dots, deduced as solar abundance minus the calculated s-process abundances), and calculated r-process predictions. Theoretical predictions cover a range of neutron densities, and are for a specific nuclear mass model, ETFSI-Q. Figure taken from [Cow06].

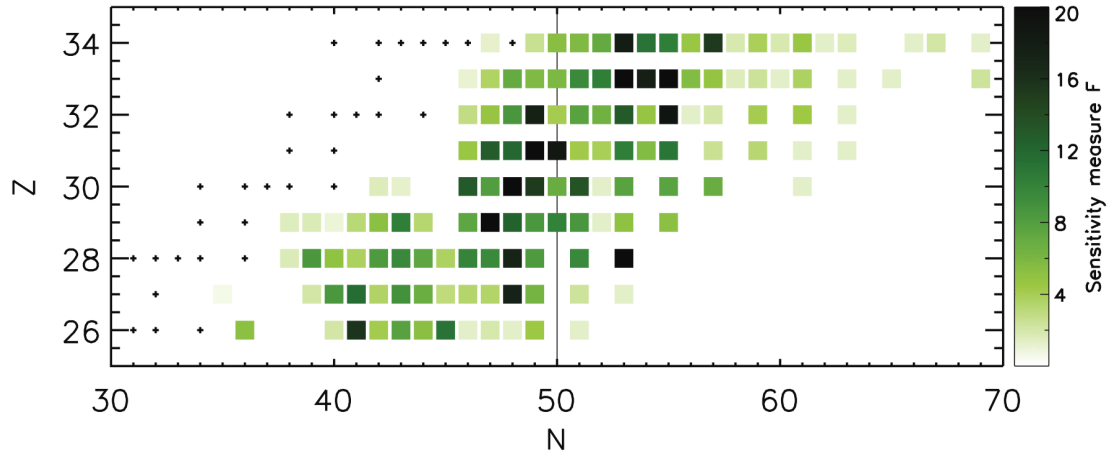


Figure 1.3: Sensitivity measure ( $F$ , on a scale of 1-20) of the final weak r-process abundance pattern on neutron capture rates in the  $A \approx 80$  region; stable isotopes are represented by black dots. Fifty-five neutron capture rate studies ran for a range of distinct astrophysical conditions [Sur14].

r-process solar abundance pattern compared to prediction. The prediction of the  $A \approx 80$  abundance peak deviates from observation. This indicates the existence of multiple different r-process sites, as well as demonstrating the lack of nuclear data in this region.

A sensitivity study into the importance of neutron-capture rates in  $A \approx 80$  nuclei on final r-process abundance patterns was conducted by Surman *et al.* [Sur14]. Current nuclear data sets of the participating nuclei were used to examine neutron-capture cross sections in the context of a hot, weak r-process and create a baseline abundance pattern. The neutron capture rates of approximately 300 nuclei in the  $A \approx 80$  region were then individually varied by a constant factor. The resulting abundance deviations from the baseline were taken to be a measure of the sensitivity of the final abundance pattern to the neutron-capture rates on the individual nuclei, as seen in Figure 1.3 [Sur14].

Sensitivity is highest around the closed shells. The points of equilibrium between neutron capture and photo-disassociation define the r-process path and “waiting points”. Individual neutron-capture rates become more important during freeze-out,

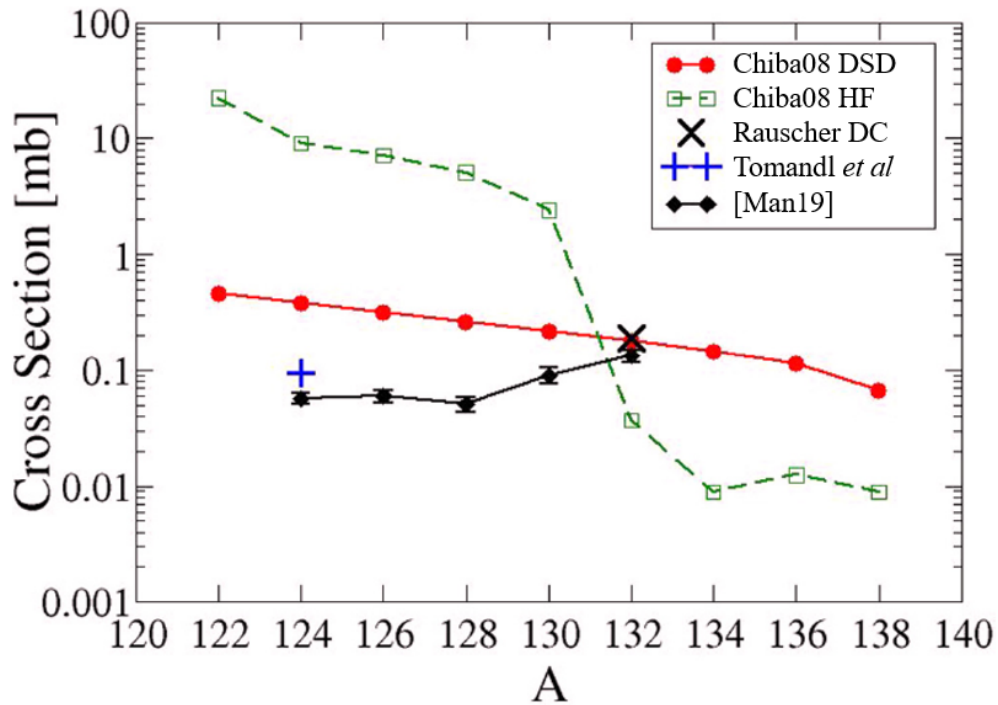


Figure 1.4: Comparison of calculated neutron-capture cross sections for tin isotopes at 30 keV. Direct-semidirect DSD calculations with experimental energies and spectroscopic factors [Man19] (black diamonds), Hauser-Feshbach model calculations [Chi08] (green squares), Calculated  $^{132}\text{Sn}$  direct capture using the theoretical spectroscopic factor [Rau98] (black X) and DSD calculations with theoretical excitation energies and spectroscopic factors (red circles) [Chi08].  $^{124}\text{Sn}$  DSD calculations using spectroscopic factors of Ref. [Tom11] for all  $\ell = 1$  levels having  $S \geq 0.01$  is given by the blue plus. Figure adopted from Ref. [Man19].

where  $\beta$  decay begins to dominate, and the radioactive nuclei near these closed-shell waiting points decay back towards stability. Extended half-lives in some of these nuclei and their daughters allow subsequent  $(n,\gamma)$  reactions to take place, shifting the final abundance pattern accordingly. Neutron capture on these specific isotopes particularly affects the final abundance pattern, yielding a high sensitivity measure to  $(n,\gamma)$ .

The majority of nuclei near or on the valley of stability have large neutron separation ( $S_n$ ) energies, and consequently a high level density for neutron capture. Therefore neutron capture can proceed via *compound* nuclear reactions, which generally can be modelled via statistical methods, such as Hauser-Feshbach [Hau52]. Nuclei near-closed-shells with a lower  $S_n$  however do not exhibit the same high density of states, and so neutron capture reactions can be more likely to proceed *directly* to a discrete state followed by gamma-ray emission, rather than via a compound nucleus. Figure 1.4 shows this trend for neutron-rich Sn isotopes, where the dominant process for  $(n,\gamma)$  reactions is predicted to be statistical for tin isotopes below the doubly magic  $^{132}\text{Sn}$ , but is direct for  $^{132}\text{Sn}$  and above [Chi08].

Direct neutron-capture  $(n,\gamma)$  cross sections depend on the transferred angular momentum, excitation energies, parities and spectroscopic factors of states in the final nucleus, and cannot typically be modelled accurately without robust experimental data. Therefore more nuclear data with reduced uncertainties are needed for these nuclei if we are to further understand the synthesis of elements in our universe.

### 1.3 Goals of this study

This research aims to provide reduced uncertainties of spectroscopic factors for the  $5/2^+$  ground state and  $1/2^+$  first-excited state (0.462 MeV) in  $^{85}\text{Se}$  (as shown in Figure

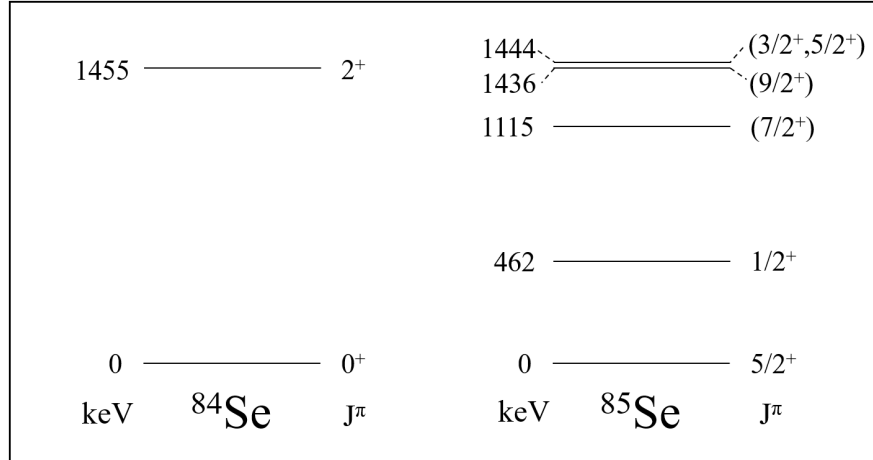


Figure 1.5: Level schemes of states in  $^{84}\text{Se}$  and  $^{85}\text{Se}$  below 1.5 MeV.

1.5, a nucleus which bridges the gap of being important to both nuclear astrophysics and nuclear structure. Indeed, the structure of this  $N=50$  closed-shell-plus-one-neutron nucleus can be used to deduce a direct neutron-capture rate that is important for understanding the weak  $r$ -process.

The dominant uncertainty associated with the extraction of spectroscopic factors is the undetermined final bound-state potential. As spectroscopic factors are a measure of the single-particle strength of a state, they are closely related to the sometimes poorly constrained parameterization of the single-particle bound-state potential. By measuring neutron transfer to states in  $^{85}\text{Se}$  at two distinct energies, a combined analysis can be used to constrain the previously unknown bound-state geometry ( $r_0, a$ ). Therefore, by constraining the bound-state geometry, significant reductions in the uncertainties of the extracted spectroscopic factors can be achieved.

A measurement of the  $^{84}\text{Se}(d,p)$  reaction at 4.5 MeV/u was previously performed in 2007 using the Holifield Radioactive Ion Beam Facility (HRIBF) at Oak Ridge National Laboratory (ORNL) [Tho07], where spectroscopic factors were extracted for the ground state and the first-excited state using a Distorted Wave Born Approximation (DWBA)

formalism. To complement this, a more recent measurement of the same reaction was performed at a higher energy of 45 MeV/u at the National Superconducting Cyclotron Laboratory at Michigan State University. Both the recent measurement at 45 MeV/u and the earlier measurement at 4.5 MeV/u have been analyzed in this work using the more appropriate ADiabatic Wave Approximation (ADWA).

This was the first use of the combined method with an N=50 radioactive beam. The use of a radioactive beam (produced via fragmentation - see section 3.1.2) introduced significant experimental challenges for the high energy measurement: low beam rates, low recoil acceptance for background reduction, and the limitations associated with inverse kinematics. Constraints on the bound-state geometry of the ground- and first-excited states in  $^{85}\text{Se}$  have been deduced, and spectroscopic factors extracted with reduced uncertainties. These are the necessary ingredients for deducing direct-capture cross sections.

#### 1.4 Structure of the dissertation

The structure of this dissertation is as follows:

Chapter Two introduces the reaction theory necessary for single-particle spectroscopy through (d,p) reactions, and goes into detail regarding the formalism of the combined method.

Chapter Three outlines the details of the  $^{84}\text{Se}(d,p)$  combined measurement. The experimental setup of the high-energy measurement will be reviewed, and the analysis tools used will be discussed. The re-analysis of the low-energy measurement at 4.5 MeV/u using the finite-range ADWA formalism is also discussed, and used in conjunction with the high energy measurement to constrain the final bound-state potential,

and therefore reduce uncertainties on the extracted spectroscopic factors.

Chapter Four details the further study of r-process, near-closed-shell nuclei with  $^{80}\text{Ge}$  ( $N=48$ ) beams. Preparation for the measurement of  $^{80}\text{Ge}(d,p\gamma)$  at 45 MeV/u is presented, including a previous study of the reaction at 3.875 MeV/u [Ahn19]. Future prospects to inform  $(n,\gamma)$  reactions on nuclei near the r-process path using GODDESS and the Facility for Rare Isotope Beams (FRIB) is also discussed.

Finally, Chapter Five summarizes the results of this dissertation, and describes a future possible measurement of  $^{87}\text{Se}(d,p\gamma)$  to infer  $(n,\gamma)$  cross sections even further from stability.

## Chapter 2

### Theory

Transfer reactions such as (d,p) are sensitive probes of the single-particle structure of radioactive nuclei. By measuring the absolute differential cross section of the ejected particles, spectroscopic information on the discrete state that the nucleon was transferred to can be extracted. From an experimental perspective, the spectroscopic factor  $S_{\ell j}$  can be represented as:

$$\left(\frac{d\sigma}{d\Omega}\right)_{Exp} = S_{\ell j} \left(\frac{d\sigma}{d\Omega}\right)_{Theory} \quad (2.1)$$

where  $\left(\frac{d\sigma}{d\Omega}\right)_{Theory}$  is the theoretically-calculated angular differential cross section, and  $\left(\frac{d\sigma}{d\Omega}\right)_{Exp}$  is the experimentally-observed differential cross section. The theoretically calculated differential cross section assumes a specific single-particle configuration for the final bound state. This means that the difference in differential cross section that is observed from the theoretical prediction informs the single-particle strength of the wavefunction. The extracted spectroscopic factor therefore depends on the theoretically calculated cross section, such that uncertainties in the predicted cross section translate directly to uncertainties in the spectroscopic factor. It is therefore important that constraints are made on aspects of the reaction formalism that introduce systematic errors in the calculated cross sections. This chapter will detail the methods used to mitigate the uncertainties associated with the unknown single-particle bound-state potential, as well as the advantages and disadvantages of the reaction formalisms necessary to

compute these cross sections.

## 2.1 Reaction formalisms

Theoretical calculations of single-particle transfer reactions are critical for interpreting the characteristics of experimentally observed states. Spin-parities are assigned by matching the shape of the observed differential cross section to that predicted with reaction theory for a transfer to a specific neutron configuration. The spectroscopic strength of a state is then deduced by normalizing the theoretical differential cross section to the experimental. This section will outline the relevant reaction formalisms and their applications within the context of (d,p) reactions.

### 2.1.1 Distorted Wave Born Approximation

Historically, single-particle transfer reactions are analyzed and interpreted through the Distorted Wave Born Approximation (DWBA). Arising from first order perturbation theory and Fermi's golden rule, the Born approximation is at the foundation of DWBA. This assumes that the scattering potential  $V(r)$  is weak, and so plane waves and spherically symmetric scattered waves are used. The scattering amplitude is then directly proportional to the Fourier transform of the scattering potential with respect to the transferred momentum. The *distortion* of this comes with the separation of the scattering potential into two parts,  $U_1 + U_2$ .  $U_1$  describes the elastic scattering channel and  $U_2$  applies to the absorption part. Here, the dominating interaction is elastic scattering, with the absorption acting as a perturbation.

This method for calculating cross sections assumes the transfer proceeds through a single step, which takes an effective deuteron - target interaction for the incident wave,

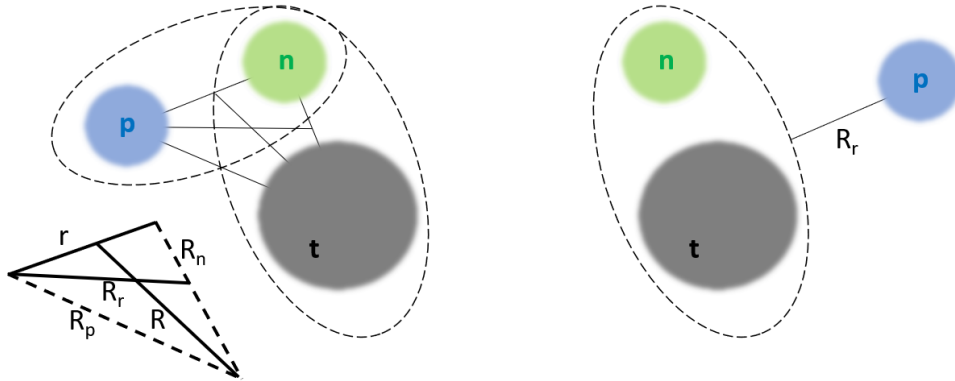


Figure 2.1: Cartoon of the entrance (*left*) and exit (*right*) channels for a (d,p) reaction. DWBA calculations assume an interaction between the deuteron and the target, while ADWA decomposes the deuteron and therefore the interaction between proton - target and neutron - target.

and a proton - recoil interaction for outgoing wave. Though DWBA has long been the favorite method for analyzing (d,p) reactions, there is no explicit consideration of the deuteron breakup within the framework. With a binding energy of 2.2 MeV (compared to its  $\sim 2$  GeV mass) the deuteron is very loosely bound, and should be regarded instead as a proton and neutron.

### 2.1.2 Adiabatic Wave Approximation

To address this issue, the ADiabatic Wave Approximation (ADWA) was developed to model the reaction as a three-body system. Where for DWBA the incident channel consisted of the deuteron - target interaction, ADWA splits the wavefunction into three: proton, neutron and target. The *adiabatic* assumption is that the relative motion of the proton and neutron,  $\dot{r}$ , is much slower than the motion between the target and the nucleons  $\dot{R}$ , as described in Figure 2.1.

Johnson and Soper [Joh70] proposed a zero range (ZR) ADWA, which assumes no relative distance between the proton and neutron within the deuteron. A finite range

(FR) version of ADWA was then developed by Johnson and Tandy [Joh74], which takes the relative p-n locations into account. A local-energy approximation can also be used to “smear” the potential locations, replicating the effects of finite range calculations.

A study by Nguyen et al [Ngu10] compared ZR- and FR-ADWA for a large number of (d,p) ground state transfer reactions, with the condition that the shape of the observed angular distribution was well described by ADWA. An error of 10% was observed for low-energy (sub-coulomb) reactions, which increased to greater than 50% for higher energies ( $E > 20$  MeV/u for  $A > 50$  and  $E > 30$  MeV/u for heavier nuclei) when disregarding finite-range effects. While this study focused only on transfers to the ground state, similar trends are expected for transfers to excited states.

Schmitt *et al.* [Sch12] compared DWBA and FR-ADWA angular distributions for the reaction  $^{10}\text{Be}(d,p)^{11}\text{Be}$  using multiple beam energies. It was observed that the DWBA extracted spectroscopic factors were strongly dependent on the choice of optical model potentials (OMP) compared to those extracted through ADWA. This is because nucleon OMPs are simpler and better constrained than for the deuteron, which has to approximate the breakup via its imaginary potential. Calculations of the  $^{84}\text{Se}(d,p)^{85}\text{Se}(\text{g.s.})$  at 4.5 MeV/u transfer were performed using two appropriate sets of OMPs for the N-n outgoing channel, using both DWBA and ADWA. Differences in cross section between Koning-Delaroche [Kon03] and Chapel Hill [Var91] OMPs within the context of the DWBA formalism are higher than those using ADWA, as shown in Figure 2.2. The shape of the cross section is also more consistent between OMPs for ADWA, whereas DWBA shows larger differences, particularly at smaller scattering angles.

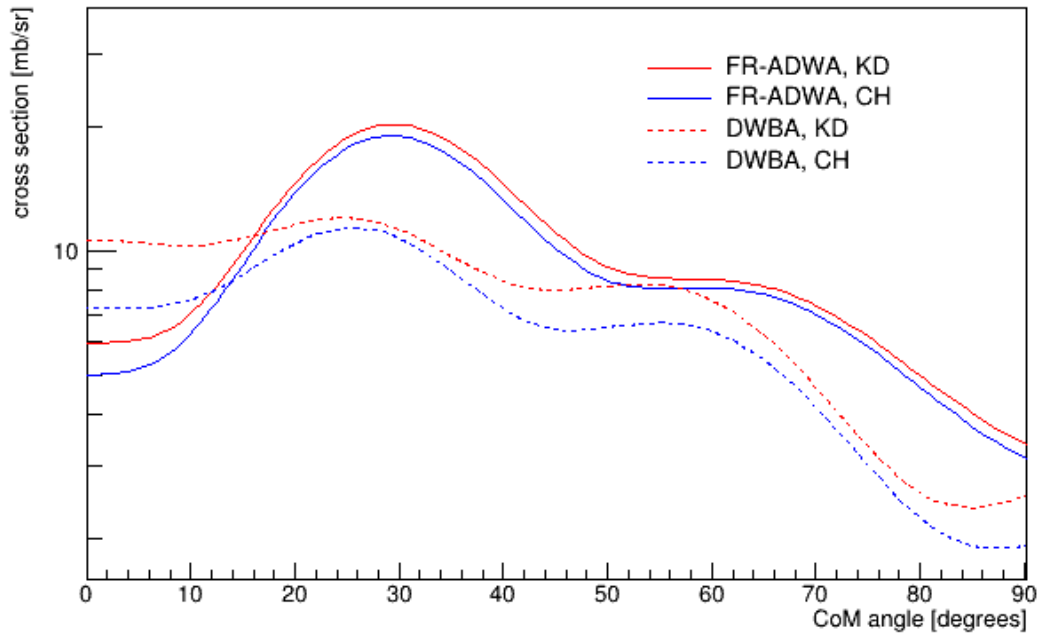


Figure 2.2: Calculations of the  $^{84}\text{Se}(d,p)^{85}\text{Se}(\text{g.s.})$  at 4.5 MeV/u transfer, using FR-ADWA (solid) and DWBA (dashed). DWBA calculations were performed using Lohr and Haeberli [Loh74] OMPs for the deuteron entrance potential, FR-ADWA target-nucleon potentials were taken from Johnson and Tandy [Joh74]. Calculations used either Koning-Delaroche (red) [Kon03] or Chapel Hill (blue) [Var91] OMPs for the proton -  $^{85}\text{Se}$  potential.

Schmitt also observed that ADWA extracted spectroscopic factors were systematically smaller than with DWBA - a critical insight showing the importance of including deuteron breakup.

Figure 2.3 shows the predicted differential cross sections for  $^{84}\text{Se}(d,p)^{85}\text{Se}$  to the ground state and first-excited state at 4.5 MeV/u and 45 MeV/u, using the range of reaction theory formalisms discussed above. Unit spectroscopic factors were used.

This work concurs with the findings of Nguyen *et al.* - the discrepancy between the zero range and the finite range calculations drastically increases at higher energies. The local energy approximation is also only appropriate at describing the more peripheral reactions at lower beam energies. The effects of DWBA vs ADWA observed by Schmitt can also be seen here. A systematic under-prediction of the cross section peak by DWBA will yield a systematically higher spectroscopic factor, relative to that produced when deuteron breakup is taken into account.

The findings displayed here, and by Nguyen and Schmitt *et al.* suggest that a full treatment of the finite range ADWA formalism is needed, for both the low- and high-energy measurements to be analyzed in a consistent formalism. FR-ADWA provides an appropriate theoretical foundation for the extraction of spectroscopic information.

### 2.1.3 FRESCO parameters

The FRESCO general-purpose reaction code [Tho06] calculates most nuclear reactions which can be expressed in a coupled-channel form. As a result of this vast capability, many input variables are required to accurately model the reaction of interest. In general, if a chosen variable is not in an appropriate range for the reaction, FRESCO will prompt the user to change it. Once these variables are in an appropriate range, the

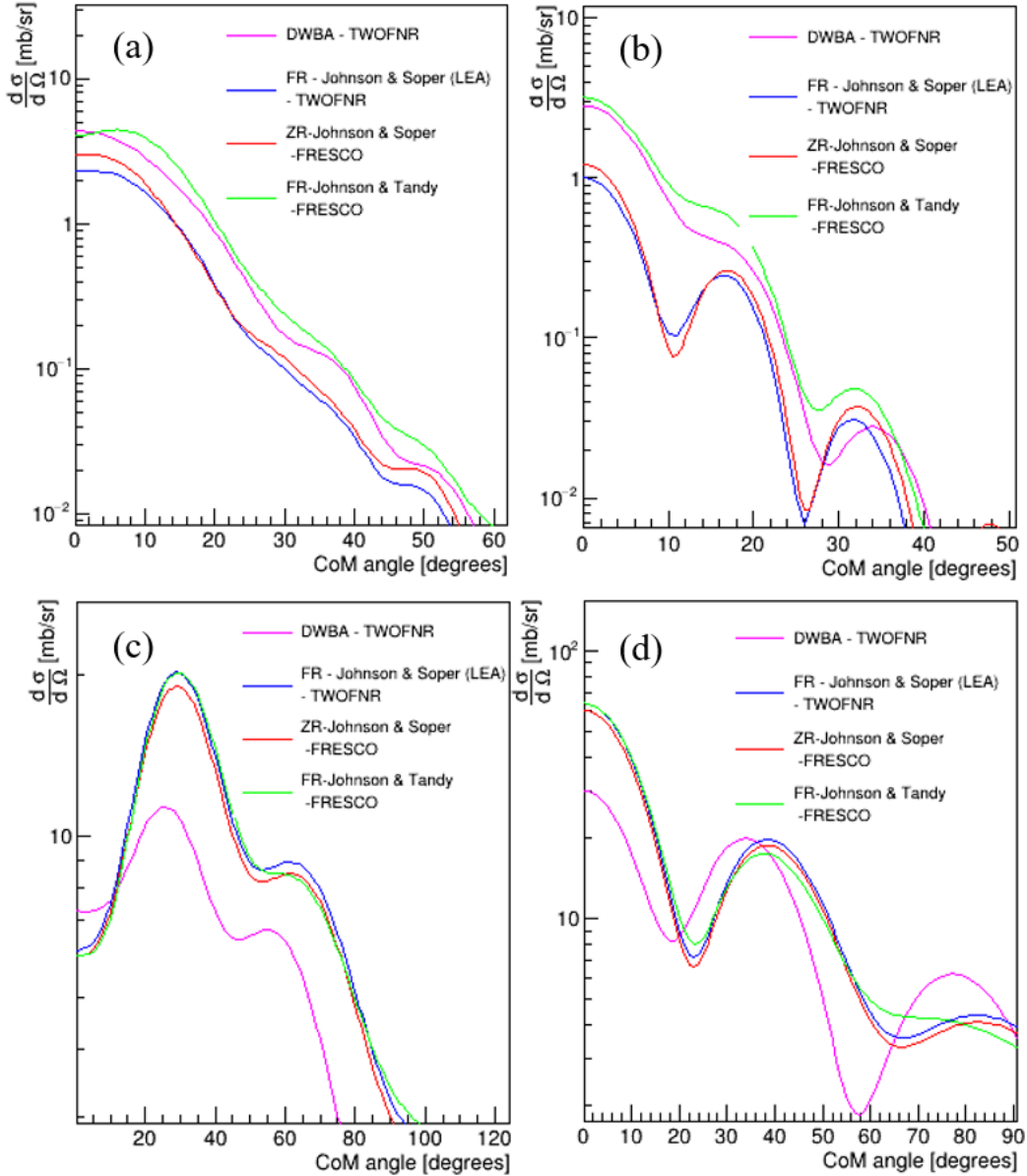


Figure 2.3: Differential cross sections calculated in the center of mass frame for  $^{84}\text{Se}(d,p)^{85}\text{Se}$ . (a)  $\ell=2$  transfer to the ground state at 45 MeV/u. (b)  $\ell=0$  transfer to the first excited state at 45 MeV/u. (c)  $\ell=2$  transfer to the ground state at 4.5 MeV/u. (d)  $\ell=0$  transfer to the first excited state at 4.5 MeV/u. Each transfer calculation was run with DWBA using Daehnick deuteron OMPs [Dae80] (*pink*), Local energy approximation - ADWA (*blue*), Zero range - ADWA with Johnson-Soper potential (*red*), and Finite range - ADWA with Johnson-Tandy potential (*green*). All calculations used Koning-Delaroche optical model parameters. Calculations run with TWOFNR [Tos19] and FRESCO [Tho06].

calculated cross section becomes relatively insensitive to their values. Table 2.1 shows the variables used to calculate the cross sections produced in this work.

Table 2.1: List of parameters, a brief description, and their values used in the FRESKO input file to calculate the differential cross sections for the  $^{84}\text{Se}(d,p)$  reaction. A more complete description of the input parameters and their purposes can be found in Reference [Tho09].

Variable label	Brief description	Value
hcm	Integration step	0.05
rmatch	radius at which the integrated wave function gets matched to the asymptotic form	30
rintp	step in $R$ for non-local Kernal	0.1
hnl	non-local step	0.1
rnl	non-local range	6.5
centre	center of the non-local interaction	0.0
jtmin	lower limit for angular momentum	0
jtmax	upper limit for angular momentum (defines the number of partial waves)	35
absend	controls the convergence, if less than zero then the calculation uses full J-interval	-1.0
thmin	lower limit for angular range	0
thmax	upper limit for angular range	180
thinc	incremental steps of theta	1.0
iter	number of iterations	1
elab	equivalent deuteron energy [MeV]	88.596
& Overlap: nm	number of nodes (including origin)	2 (g.s. - $2d_{5/2}$ ) 3 ( $1^{st}$ Ex - $3s_{1/2}$ )
& Coupling: kind	specifies transfer coupling (5 = zero-range, 6 = LEA, <sup>1</sup> 7 = finite-range)	7
IP1	post (0) or prior (1) representation	0
IP2	full (-1), no (0), full real (1) remnant used	-1

<sup>1</sup> Local Energy Approximation

## 2.2 The optical model

The optical model provides a mean-field approximation to the many-body potential between the target and the projectile consisting of a real  $V(r)$  and imaginary  $iW(r)$  part, accounting for the elastic scattering and absorption, respectively. The real part includes Coulomb  $V_C$ , volume  $V$  and spin-orbit  $V_{so}$  terms, and the imaginary part

has volume  $W$  and surface  $W_D$  terms. All of these terms have the typical form of a Woods-Saxon potential given in equation 1.1, except for the Coulomb term which goes as  $1/r$ .

The choice in optical model used to generate the interaction potential introduces uncertainties in the calculated cross section. The degree of sensitivity of the cross section to the choice in optical model is also dependent on the reaction formalism used, and the applicability of the chosen model, as discussed in section 2.1.2. From large sets of elastic scattering data, global optical model parameterizations are compiled for appropriate mass and reaction-energy ranges. As we consider more exotic nuclei, where elastic scattering may not have been measured, extrapolations of these global sets are a current option.

The primary optical model parameterization used in this study is that of Koning-Delaroche [Kon03], as shown in Tables 2.2 and 2.3. These global optical model parameters were constructed with large data sets of elastic scattering, and are appropriate for the energy range 1 keV to 200 MeV, and mass range  $24 \leq A \leq 209$ . These are the most extensive neutron-nucleus optical model parameters that are currently available in literature. To quantify uncertainties due to the choice in optical model, the more limited parameterizations from Chapel Hill [Var91] were also used to calculate the differential cross sections.

Table 2.2: Koning-Delaroche phenomenological global optical model parameters [Kon03] for the ground state transfer used to construct the adiabatic potential of Johnson and Tandy [Joh74].

	$V$ [MeV]	$r_0$ [fm]	$a_0$ [fm]	$W$ [MeV]	$r_w$ [fm]	$a_w$ [fm]	$W_s$ [MeV]	$r_{ws}$ [fm]	$a_{ws}$ [fm]	$V_{so}$ [MeV]	$r_{so}$ [fm]	$a_{so}$ [fm]	$W_{so}$ [MeV]	$r_{soi}$ [fm]	$a_{soi}$ [fm]
n	35.640	1.211	0.665	4.233	1.211	0.665	3.822	1.273	0.531	4.976	1.038	0.590	-0.316	1.038	0.590
p	44.244	1.211	0.665	4.594	1.211	0.665	5.829	1.273	0.562	5.012	1.038	0.590	-0.297	1.038	0.590
$^{85}\text{Se}+p$	29.706	1.212	0.665	9.285	1.212	0.665	2.223	1.273	0.563	4.169	1.038	0.590	-0.849	1.038	0.590

Table 2.3: The same as table 2.2 but for neutron transfer to the first excited state.

	$V$ [MeV]	$r_0$ [fm]	$a_0$ [fm]	$W$ [MeV]	$r_w$ [fm]	$a_w$ [fm]	$W_s$ [MeV]	$r_{ws}$ [fm]	$a_{ws}$ [fm]	$V_{so}$ [MeV]	$r_{so}$ [fm]	$a_{so}$ [fm]	$W_{so}$ [MeV]	$r_{soi}$ [fm]	$a_{soi}$ [fm]
n	35.640	1.211	0.665	4.233	1.211	0.665	3.822	1.273	0.531	4.976	1.038	0.590	-0.316	1.038	0.590
p	44.244	1.211	0.665	4.594	1.211	0.665	5.829	1.273	0.562	5.012	1.038	0.590	-0.297	1.038	0.590
$^{85}\text{Se}+p$	29.832	1.212	0.665	9.250	1.212	0.665	2.245	1.273	0.563	4.177	1.038	0.590	-0.843	1.038	0.590

### 2.3 Asymptotic normalization coefficients

The spectroscopic factor is defined as the square of the normalization of the radial overlap function between the nuclear bound state and the core nucleus plus a valence nucleon - predominantly located in the interior of the nucleus [Cas00]. However, most (d,p) reactions (with beam energies  $\lesssim 6$  MeV/u) probe only the tail of the wavefunction. At large radii, the nuclear wavefunction  $\Psi_{\ell j}$  can effectively be modelled as a Hankel function  $h_{\ell}(ikr)$ , normalized to the amplitude of the tail by the many-body asymptotic normalization coefficient (ANC),  $C_{\ell j}$  [Tho09].

$$\Psi_{\ell j} \rightarrow C_{\ell j} h_{\ell}(ikr) \quad (2.2)$$

The peripheral nature of low-energy transfer reactions makes these useful probes for understanding the radial behavior of the wavefunction and extracting the ANC.

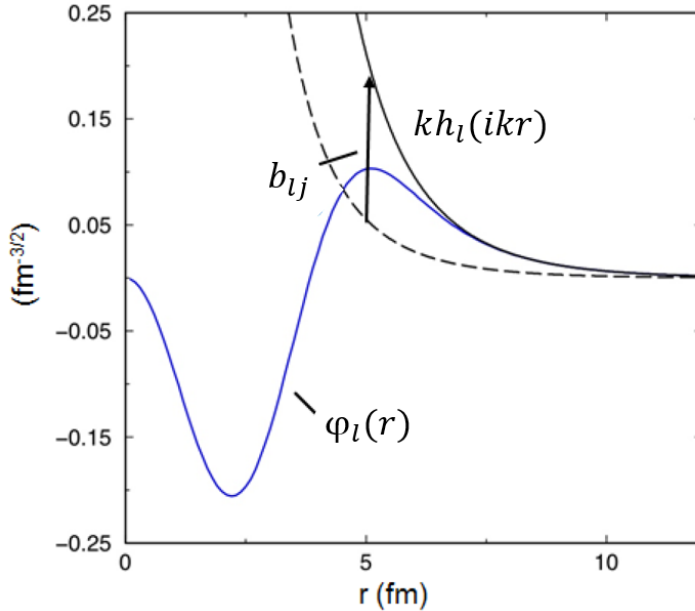


Figure 2.4: Single-particle wavefunction  $\varphi_{\ell}(r)$  (blue), with the tail represented as a spherical Hankel function (dashed), normalized by the single-particle ANC  $b_{\ell j}$  (solid). Adopted from reference [Wal18].

The tail of a single-particle wavefunction can also be modelled in the same fashion,

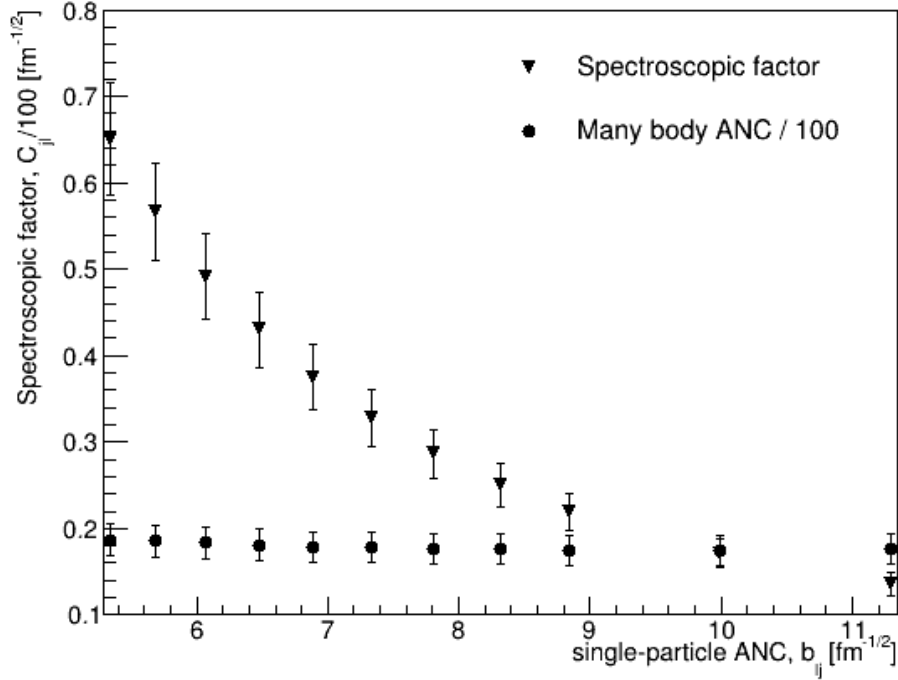


Figure 2.5: Extracted spectroscopic factor  $S$ , and many-body ANC,  $C_{\ell j}$  as a function of the single-particle ANC,  $b_{\ell j}$  for the reaction  $^{86}\text{Kr}(d,p)^{87}\text{Kr}(\text{g.s.})$  at 5.5 MeV/u. Data taken by Haravu *et al.* [Har70] and analyzed by Walter [Wal18].

with its own *single-particle* ANC (spANC),  $b_{\ell j}$ , as shown in Figure 2.4. Changes in the shape of the single-particle Woods-Saxon bound state potential (*i.e.* radius  $r_0$  and diffuseness  $a$  parameters) affects the shape of the single-particle wavefunctions, yielding different values for  $b_{\ell j}(r_0, a)$ . The degree to which the many-body (nuclear) ANC corresponds to the spANC is once again given by the strength of the single-particle configuration, the spectroscopic factor,  $S_{\ell j}$  [Tho09].

$$C_{\ell j}^2 = S_{\ell j} b_{\ell j}^2 \quad (2.3)$$

Therefore, there is an intimate relationship between the extracted spectroscopic information, the parameters used to describe the single-particle potential, and the differential cross sections measured for these reactions.

Figure 2.5 shows the extracted spectroscopic factors and many-body ANCs as a

function of the single-particle ANC for the  $^{86}\text{Kr}(\text{d,p})$  reaction at 5.5 MeV/u [Har70; Wal19]. As the asymptotic form of the overlap function is proportional to  $C_{\ell_j}$  (as shown in Equation 2.2), the peripheral cross section becomes proportional to  $C_{\ell_j}^2 = S_{\ell_j} b_{\ell_j}^2$ , and not the spectroscopic factor alone. This is reflected in Figure 2.5, where the many-body ANC is independent of the choice in shape of the bound-state potential, and so is reliably extracted. From equation 2.3, the extracted spectroscopic factor is therefore sensitive to the chosen shape of the bound-state potential (and hence, the single-particle radial wavefunction and single-particle ANC), as can be seen in Figure 2.5.

Figure 2.6 shows another example of the sensitivity of (d,p) cross section predictions to bound-state geometries: the calculated differential cross sections for  $^{84}\text{Se}(\text{d,p})^{85}\text{Se}(\text{g.s.})$  at 4.5 MeV/u assuming unit spectroscopic factors. Calculations were performed using a range of  $r_0, a$ :  $1.000 \leq r_0 \leq 1.375$  and  $0.520 \leq a \leq 0.715$ . This range was used to make sure that the crossing point between the high- and low-energy measurements, and its uncertainty, are fully included.

From Equation 2.1, spectroscopic factors relative to those deduced for canonical values of the radius and diffuseness ( $r_0=1.25, a=0.65$ ) can be deduced by comparing relative normalizations at the peak of each cross section for different single-particle ANCs. Table 2.4 shows the range of spectroscopic factors possible for the range of bound-state parameters stated above, using Equation 2.3. Clearly, measures to constrain the bound-state geometry - and therefore the single-particle ANC - must be adopted if reduced uncertainties on spectroscopic factors are to be achieved.

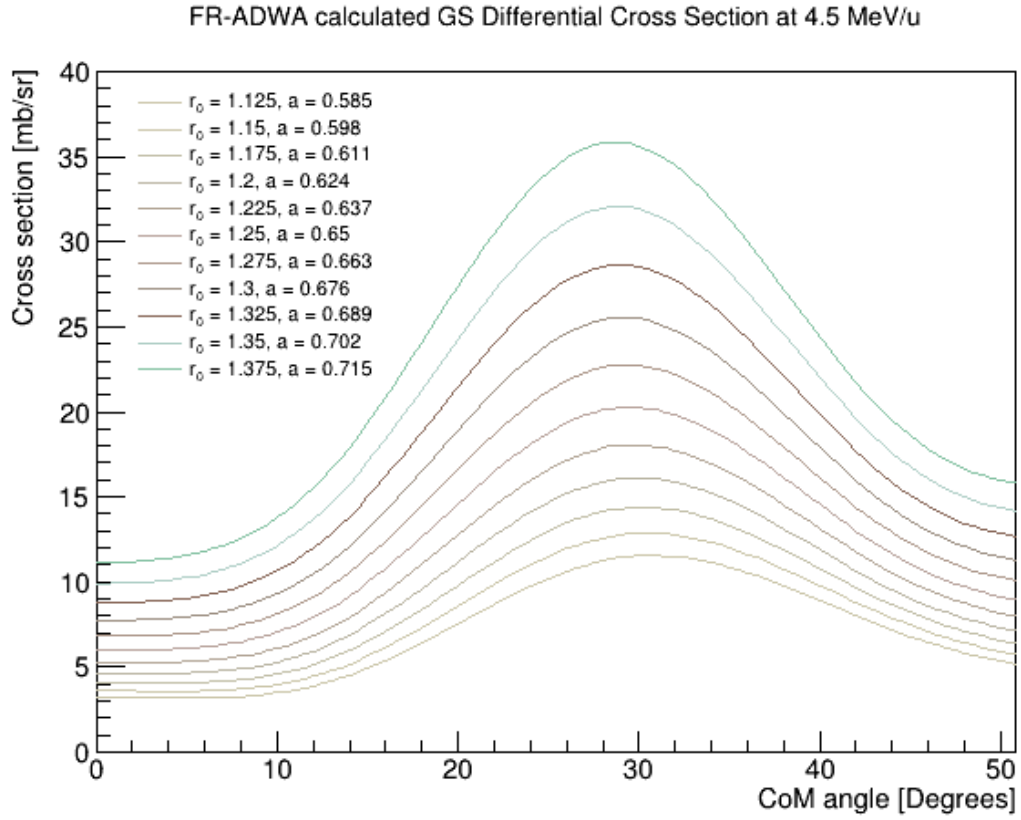


Figure 2.6: Differential cross section calculations as described in section 2.1, using Koning-Delaroche global optical model parameters for the  $\ell = 2$  transfer to the ground state in  $^{85}\text{Se}$  for a range of bound state geometries, assuming unit spectroscopic factors. Johnson and Tandy [Joh74] potentials are used within the finite-range adiabatic wave approximation formalism. Calculated using FRESKO [Tho06].

Table 2.4: Single particle ANCs,  $b_{\ell j}$ , for a range of bound state geometries for the ground state and first excited state in  $^{85}\text{Se}$  for the reaction  $^{84}\text{Se}(d,p)$  at 4.5 MeV/u. The relative spectroscopic factor  $\Delta S$  is deduced from equation 2.3, and are normalized to values for  $r = 1.25$  and  $a = 0.65$ :  $\Delta S = b_{\ell j}^2(r_0, a)/b_{\ell j}^2(1.25, 0.65)$ .

Bound state parameters		5/2 <sup>+</sup> g.s.		1/2 <sup>+</sup> 1 <sup>st</sup> Ex	
$r_o$ [fm]	$a$ [fm]	$b_{\ell j}$ [fm <sup>-1/2</sup> ]	$\Delta S$	$b_{\ell j}$ [fm <sup>-1/2</sup> ]	$\Delta S$
1.000	0.520	2.28	0.29	6.56	0.39
1.025	0.533	2.43	0.33	6.88	0.43
1.050	0.546	2.60	0.37	7.21	0.47
1.075	0.559	2.77	0.43	7.56	0.52
1.100	0.572	2.95	0.48	7.93	0.57
1.125	0.585	3.13	0.54	8.31	0.63
1.15	0.598	3.33	0.61	8.71	0.69
1.175	0.611	3.55	0.70	9.13	0.76
1.2	0.624	3.77	0.79	9.57	0.83
1.225	0.637	4.00	0.88	10.02	0.91
1.25	0.65	4.25	1	10.50	1
1.275	0.663	4.51	1.12	11.01	1.10
1.3	0.676	4.78	1.27	11.54	1.21
1.325	0.689	5.07	1.43	12.09	1.33
1.35	0.702	5.38	1.61	12.67	1.46
1.375	0.715	5.70	1.79	13.27	1.60

## 2.4 The combined method

The uncertainty of transfer cross sections associated with our ignorance of the single-particle potential's radius and diffuseness is largely neglected when deducing spectroscopic information. This becomes increasingly important in weakly-bound radioactive nuclei, where single-particle potentials are expected to deviate from the standard values. Historically, no attempts have been made to constrain the asymptotic region of the wavefunction: single-particle parameters were adjusted such that closed-shell nuclei yielded pure single-particle configurations. From equation 2.3, this forces the many-body ANC to have an arbitrary value.

The effort to constrain the single-particle ANC through simultaneous analysis at both high- and low-energies began with Nunes and Mukhamedzhanov [Muk05].

They proposed measuring the same reaction at two energies: one low ( $\sim 5$  MeV/u), which probes the peripheral region of the wavefunction and another at higher energy ( $\sim 45$  MeV/u) which probes deeper into the nuclear interior. The low-energy measurement provides a reliable extraction of the many-body ANC, as only the asymptotic tail contributes to the cross section. Because there is no sensitivity to the details of the interior wavefunction at low energies, there is no sensitivity to the potential used to calculate the single-particle wavefunction. For the high-energy measurement, the many-body ANC extracted from the analysis will have a larger sensitivity to the bound-state parameters (and therefore  $b_{\ell j}$ ), as this reaction probes deeper than the asymptotic region alone. As the many-body ANC is a characteristic of the nucleus - not the probe - the correct  $b_{\ell j}$  for the given state should produce a consistent value for  $C_{\ell j}$  *regardless* of the beam energy.<sup>1</sup> A constraint can then be made on  $b_{\ell j}$  that gives the same value for  $C_{\ell j}$  using both the high- and low-energy probes.

This was first demonstrated by Mukhamedzhanov, Nunes and Mohr [Muk08], where data from the previously measured  $^{48}\text{Ca}(d,p)$  reaction was analyzed in the context of the “combined method” at multiple energies. The authors were able to constrain a region for the single-particle ANC - reducing uncertainties on the deduced spectroscopic factors for the ground state and first excited state.

A recent study on  $^{86}\text{Kr}$  by Walter *et al.* [Wal19] demonstrates the effectiveness of this method for N=50 nuclei. A measurement of  $^{86}\text{Kr}(d,p)$  at 33 MeV/u was compared to a previous measurement by Haravu *et al.* [Har70] at 5.5 MeV/u. Both reactions were analyzed within the Finite-Range ADiabatic Wave Approximation (FR-ADWA)

---

<sup>1</sup>A caveat of this is that the reaction formalism (and potential parameters) used to produce the theoretical cross section must be appropriate at both of the reaction energies investigated.

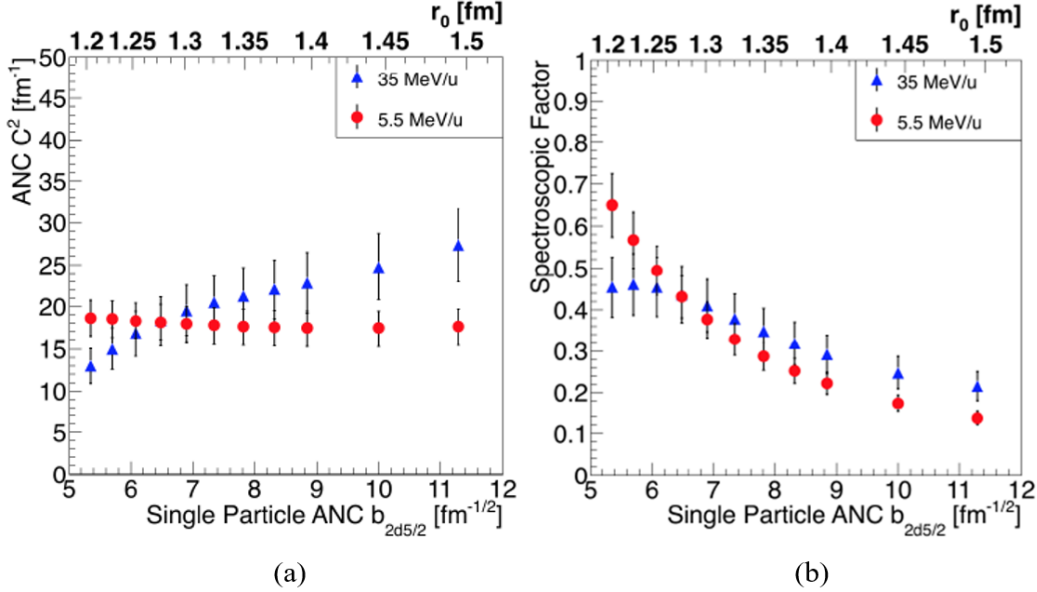


Figure 2.7: (a) Extracted many-body ANCs and (b) spectroscopic factors for a range of single-particle ANCs for the  $^{86}\text{Kr}(d,p)$  reaction at 5.5 MeV/u (red) [Har70] and 35 MeV/u (blue) [Wal19]. FR-ADWA analysis with Koning-Delaroche optical model parameters was used for both energies. Error bars represent experimental systematic uncertainties, uncertainty in the FR-ADWA calculation and also least squares fit to the data with statistical uncertainties. Figure adopted from Ref [Wal19].

formalism. Through the combined method framework, Walter constrained the  $5/2^+$ - $2d_{5/2}$  ground state single-particle ANC to  $6.46^{+1.12}_{-0.57} \text{ fm}^{-1/2}$ , and the spectroscopic factor and many-body ANC to  $0.44^{+0.09}_{-0.13}$  and  $18 \pm 2 \text{ fm}^{-1}$ , respectively. These single-particle ANCs correspond to a bound-state configuration with radius and diffuseness  $1.27^{+0.07}_{-0.04} \text{ fm}$  and  $0.66^{+0.04}_{-0.02} \text{ fm}$ , respectively. Figure 2.7 shows the extracted many-body ANCs and spectroscopic factors as a function of single-particle ANC for both the low- and high-energy measurements.

The present study is the first demonstration of the combined method with radioactive nuclei around the  $N=50$  closed-shell, analyzing the  $^{84}\text{Se}(d,p)^{85}\text{Se}$  reaction at 4.5 and 45 MeV/u. The previous measurement of this reaction at 4.5 MeV/u by Thomas *et al.* [Tho07] extracted spectroscopic factors and nuclear ANCs for the  $5/2^+$  ground state

and  $1/2^+$  first excited state assuming the standard bound state geometry ( $r_0=1.25$ ,  $a=0.65$ ) and using the Distorted Wave Born Approximation (DWBA) reaction formalism. Without a constraint on the single-particle wavefunction, the uncertainty in the extracted spectroscopic factor due to the unknown single-particle ANC can be larger than all other uncertainties associated with the analysis (typically on the order of  $\sim 20\%$ ).

In the present work, the low-energy measurement has been re-analyzed within the FR-ADWA framework, and combined with a recent measurement at 45 MeV/u at the National Superconducting Cyclotron Laboratory (NSCL) using the Oak Ridge Rutgers University Barrel Array (ORRUBA) and the Silicon Detector ARray (SIDAR) coupled to the S800 magnetic spectrograph, in order to veto other unwanted reaction channels.

## Chapter 3

### $^{84}\text{Se}(\text{d,p})^{85}\text{Se}$

The  $^{84}\text{Se}(\text{d,p})$  reaction was measured at 45 MeV/u in inverse kinematics at the National Superconducting Cyclotron Laboratory (NSCL) using the Oak Ridge Rutgers University Barrel Array (ORRUBA) and the Silicon Detector ARray (SIDAR) coupled to the S800 mass spectrograph.

Used in combination with the published study at 4.5 MeV/u by Thomas *et al.* [Tho07], constraints were made on the bound-state geometry of single-particle states in  $^{85}\text{Se}$ , reducing uncertainties in the extracted spectroscopic factors. This chapter will detail the experimental techniques necessary to perform this measurement and the data analysis used to extract absolute differential cross sections for the  $^{85}\text{Se}$  ground- and first-excited (0.462 MeV) state. Differential cross sections from both this high-energy (45 MeV/u) measurement and the earlier low-energy (4.5 MeV/u) measurement will be compared to FR-ADWA calculations to constrain the bound-state geometry and deduce spectroscopic factors.

Ideally, transfer reactions are measured using light projectiles incident on heavy targets. This is known as “normal kinematics”, and is typically used for reactions on stable nuclei. This, however, cannot easily be used to study radioactive nuclei. Their short-lived nature makes them an inappropriate choice for a target, as they promptly decay away before the reaction can be effectively measured. A heavy Radioactive Ion

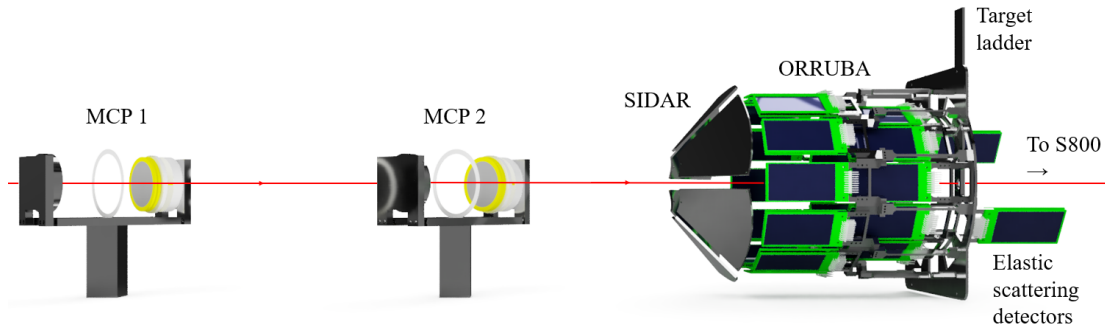


Figure 3.1: 3D CAD drawing of the experiment setup. Beam direction is left to right, MCPs located upstream of the target, followed by SIDAR and ORRUBA. Downstream of the target, two ORRUBA detectors were deployed to measure elastic scattering.

Beam (RIB) incident on a light target is therefore necessary to measure these reactions.

Inverting the laboratory reference frame in this fashion is known as *inverse kinematics*.

### 3.1 $^{84}\text{Se}(d,p)^{85}\text{Se}$ at 45 MeV/u

The radioactive  $^{84}\text{Se}$  beam was produced via fragmentation and delivered to the experimental target area for a total of 7 days, where two Multi Channel Plate (MCP) detectors (used for beam normalization) preceded the  $1200 \mu\text{g}/\text{cm}^2$   $\text{CD}_2$  target. Surrounding the target at backward angles were ORRUBA and SIDAR, which were positioned at large target-detector distances to maintain sufficient Q value resolution with the large ( $\approx 6$  mm diameter) beam spot. These detected the light reaction products, while the heavy recoil nucleus ( $^{85}\text{Se}$ ) continued to the S800 magnetic spectrograph for background suppression.

#### 3.1.1 Inverse kinematics

Performing a measurement in inverse kinematics changes the laboratory reference frame entirely compared to a normal kinematics experiment, as the center-of-mass of the

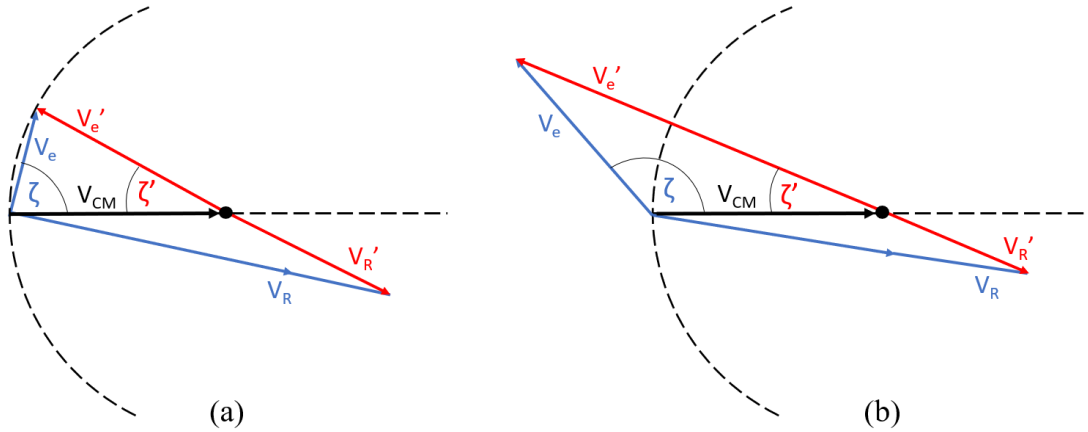


Figure 3.2: Galilean addition of velocities to boost from the lab frame to the center of mass frame for the reaction  $m_p(m_t, m_e)m_R$  in inverse kinematics. Elastic scattering (a) - where  $m_p = m_R$  and  $m_t = m_e$  - and stripping reactions (b) such as (d,p). The laboratory (blue) and center of mass frame (red, indicated with prime) are both shown. The center of mass velocity is given by  $V_{CM}$ , and the scattering angle of the ejectile is given by  $\zeta$ . In both cases the heavy beam is incident from the right.

system is moving at a velocity close to that of the beam itself. Figure 3.2 shows the Jacobian boosting the ejectile proton to large scattering angles in the laboratory frame for (d,p) reactions. For the  $^{84}\text{Se}(d,p)$  measurement, a *relativistic* Jacobian to convert to and from the center-of-mass frame is necessary, as the 45 MeV/u beam has a velocity of  $0.3c$ . Figure 3.3 shows the angular distribution in the center-of-mass and laboratory frame for the 4.5 and 45 MeV/u transfers to the ground state. The boost to large backward angles is clear for both reaction energies; however the increased velocity of the center-of-mass frame in the high energy reaction emphasizes this effect. These backward angles are therefore critical for measurements in inverse kinematics - particularly at higher beam energies.

Another effect from inverse kinematics is the specific energy - angle relationship that arises. Conserving energy and momentum in the system yields a kinetic energy for the proton, dependent on its scattering angle. In general for stripping reactions such as

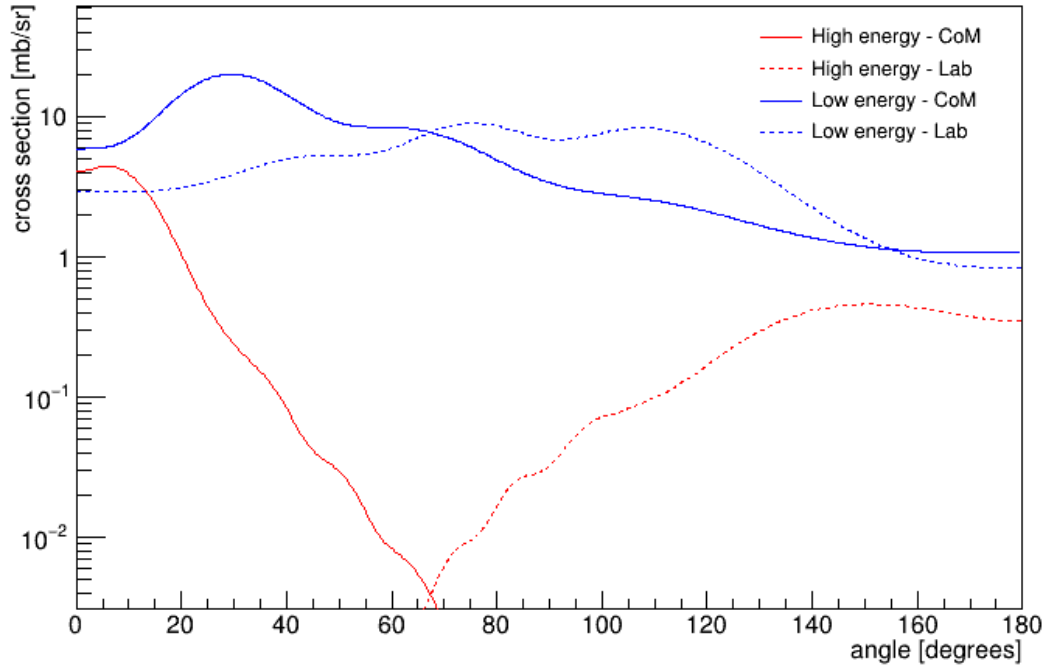


Figure 3.3: ADWA-predicted differential cross sections for the  $^{84}\text{Se}(d,p)^{85}\text{Se}(g.s.)$  at 4.5 and 45 MeV/u - demonstrating the boost from the center of mass frame to the laboratory frame. Note that for the high energy reaction, relativistic effects are accounted for.

(d,p) in inverse kinematics, the energy increases with decreasing laboratory scattering angle. Note that the rate at which the energy increases is directly proportional to the beam energy. For normal kinematics, the energy - angle relationship is essentially flat. Introducing angular dependence to the proton energy therefore increases the sensitivity of the extracted center-of-mass energy to the measured scattering angle. Therefore, a good Q value (or excitation energy) resolution in the center of mass frame requires good energy *and* angular resolution in the laboratory frame.

Another challenge presented is the reduction in the observed separation of excited states. This “kinematic compression” typically reduces the observed separation of states by a factor of three for (d,p) reactions, but can range as large as a factor of 10 for some combinations of beam energy and Q value [Pai20].

The challenges outlined above: backward angle focusing, increased sensitivity to uncertainty in measured scattering angle, and kinematic compression all necessitate the coverage of backward scattering angles with high position (angular) and energy resolution charged-particle detectors.

### 3.1.2 Beam development, delivery and tracking

The unstable  $^{84}\text{Se}$  beam was produced at the NSCL via the projectile fragmentation method, as shown in Figure 3.4. Initially, a stable primary beam of ionized ( $q=14+$ )  $^{86}\text{Kr}$  was produced in a superconducting electron-cyclotron-resonance (SC-ECR) ion source, and injected into the coupled K500 and K1200 cyclotrons to fully strip and accelerate the beam to 140 MeV/u. The accelerated (and fully ionized,  $q=34+$ ) primary beam of  $^{86}\text{Kr}$  was incident on a 345 mg/cm<sup>2</sup> thick Be production target to produce  $^{84}\text{Se}$  (amongst other, unwanted nuclei) at the entrance to the A1900 fragment separator. To achieve beam purification, the A1900 uses magnetic rigidity in combination with energy-loss analysis. A degrader wedge of 150 mg/cm<sup>2</sup> thick Al was deployed at the image 2 position, providing dispersion between ions with similar  $A/q$ , but different  $Z$ . These are then separated out in the second half of the spectrometer. The purified beam of  $^{84}\text{Se}$  is then delivered to the focal plane. Collimator slits are used in the experiment to minimize contamination as much as possible, and dictate the momentum dispersion of the beam at the experimental target. The momentum dispersion of this measurement was set to 1%.

Downstream of the A1900, the beam passes through two Micro Channel Plate (MCP) detectors, deployed to track the angle and position of the beam, to infer the interaction position at the target, and reduce uncertainties in the measured scattering

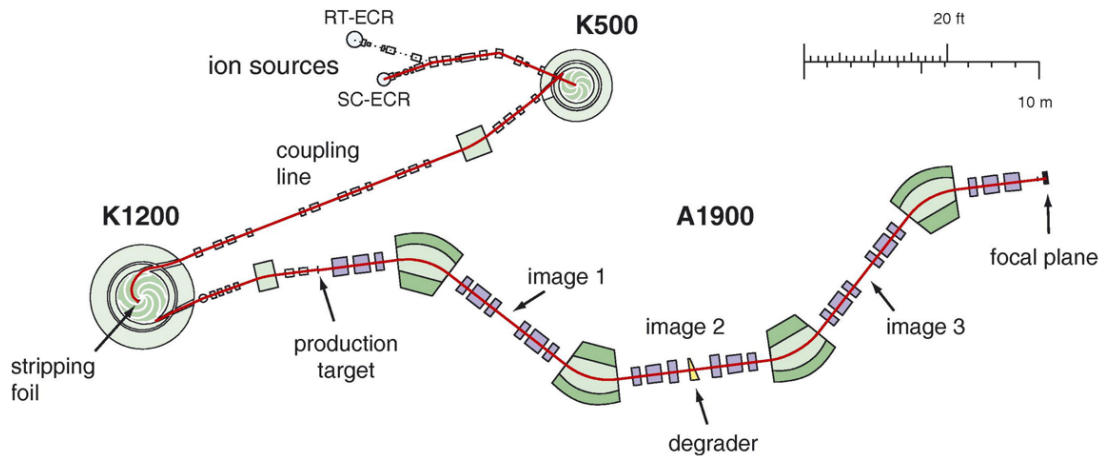


Figure 3.4: Schematic diagram of the Coupled Cyclotron facility and the A1900 fragment separator at the NSCL. Figure adopted from Reference [Sto05].

angle. The setup of these detectors are similar to those found in Reference [Sha00], where the beam passes through a thin (0.1 mil) aluminized mylar foil. Scattered electrons are directed and focused towards the face of the MCP using electric and magnetic fields. Once the electrons hit the face of the MCP, the chevron micro channel plates cause an avalanche of electrons onto the back resistive plate where there is an anode contact on each corner. The contacts each measure the signal from the electron avalanche, such that an x-y position can be reconstructed by comparing the relative signal strengths. This setup requires precise tuning of the electric and magnetic field and gain matching of the 4 anodes, in order to extract position information. Unfortunately, the position reconstruction was unsuccessful in this commissioning experiment of the MCP. This may be due to the fact that permanent magnets were used (rather than electromagnets), which does not provide adjustable strength. This meant that the magnetic field could not be optimized for the setup, and so the electrons may not have retained their initial position from the foil.

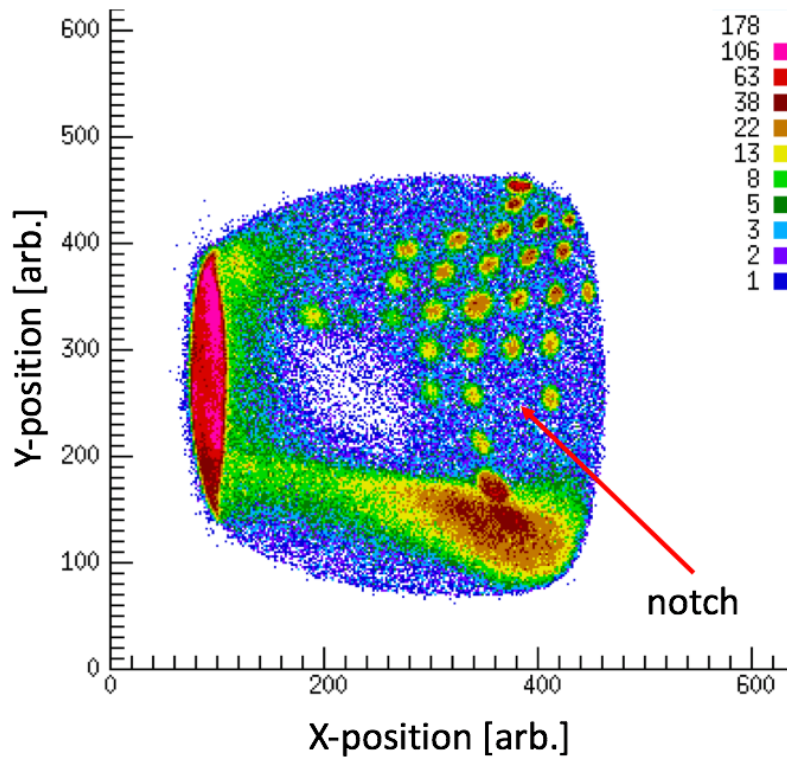


Figure 3.5: Reconstructed position spectrum using alpha particles incident through a mask onto the MCP face. The “notch” indicates the orientation of the mask. The mask holes are 1mm in diameter, and spaced 2.5mm apart.

Figure 3.5 shows a position spectrum achieved offline by impinging alpha particles *directly* onto the face of the MCP with a mask of 1 mm diameter holes, to demonstrate the position sensitivity.

The MCPs provided 4 ns timing resolution with 98.3(8)% efficiency. This enabled time-of-flight measurements and high-efficiency beam counting - both of which are essential for normalizing the extracted differential cross sections. The XF scintillator is located at the exit of the A1900 analysis line, just before the experimental setup. This was not used to measure the beam rate, as it degrades with time - it must be “shimmed” periodically to maintain sufficient efficiency. This was still used in determining the beam composition, but not in calculating the total flux.

### 3.1.3 Silicon Detectors

Figure 3.6 shows the experimental setup of the silicon detectors between the MCP detectors and the S800 magnetic spectrograph. Silicon detectors were positioned around the target to measure the scattering angle and energy of the ejectile protons. The radially segmented Silicon Detector ARray (SIDAR) [Bar01] was deployed at the most backward angles, to detect protons between  $159^\circ$  and  $171^\circ$  in the laboratory frame. At larger scattering angles, two barrels of ORRUBA (Oak Ridge - Rutgers University Barrel Array) [Pai09] measured protons between  $125^\circ$  and  $156^\circ$  [Wal18]. Though both barrels of ORRUBA were positioned upstream of the target (and therefore covering angles larger than  $90^\circ$ ), the two barrels will be referred to as “Upstream” and “Downstream”, with respect to one another.

For both ORRUBA and SIDAR, telescope configurations using energy loss (dE) and residual energy (E) layers of silicon detectors was implemented. For SIDAR, thicknesses of  $65\mu m$  or  $100\mu m$  were used for the dE layer, and  $1000\mu m$  was used for the E layer. For the upstream ORRUBA barrel, the dE layer used BB10 detectors ( $65\mu m$ ) and the E layer used SuperX3 detectors ( $1000\mu m$ ). The downstream ORRUBA barrel was comprised of X3 detectors ( $500\mu m$ ) for the dE layer, and SuperX3s for the E layer once again.

The SuperX3 detectors use four resistive strips on the front side, to provide position sensitivity in the z axis (corresponding to a polar angle measurement). When a charged particle is incident, the relative strength of the signals at each contact provides the position, whereas the energy is calculated via the sum of the two signals. This allows for the system to use a relatively low number of channels, while maintaining  $\sim 1^\circ$  polar angle resolution. Four non-resistive, perpendicular strips in the azimuthal direction

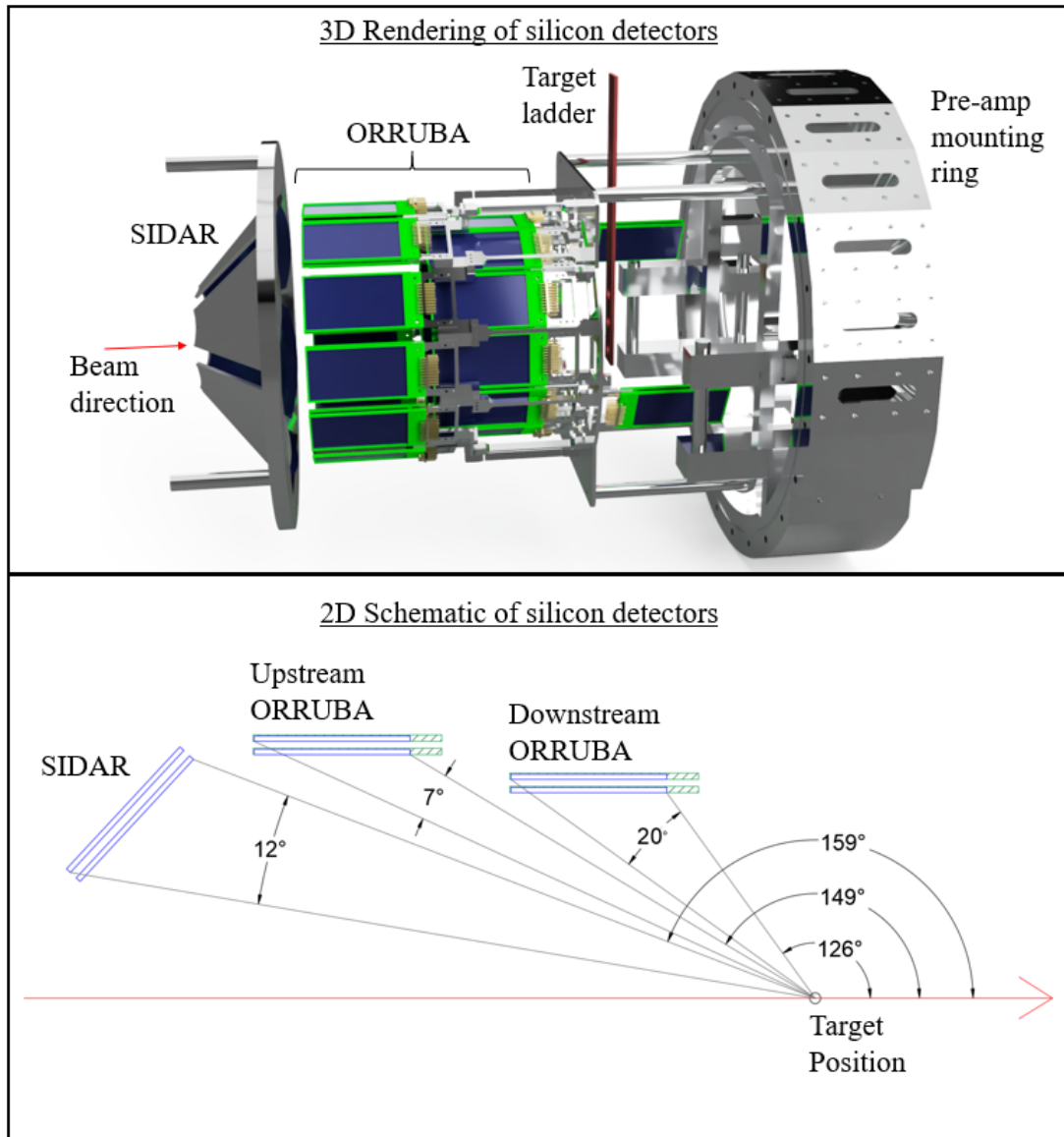


Figure 3.6: (Top) 3D rendering of silicon detector setup surrounding target. (Bottom) 2D schematic detailing detector locations upstream of the target. Beam direction is from left to right.

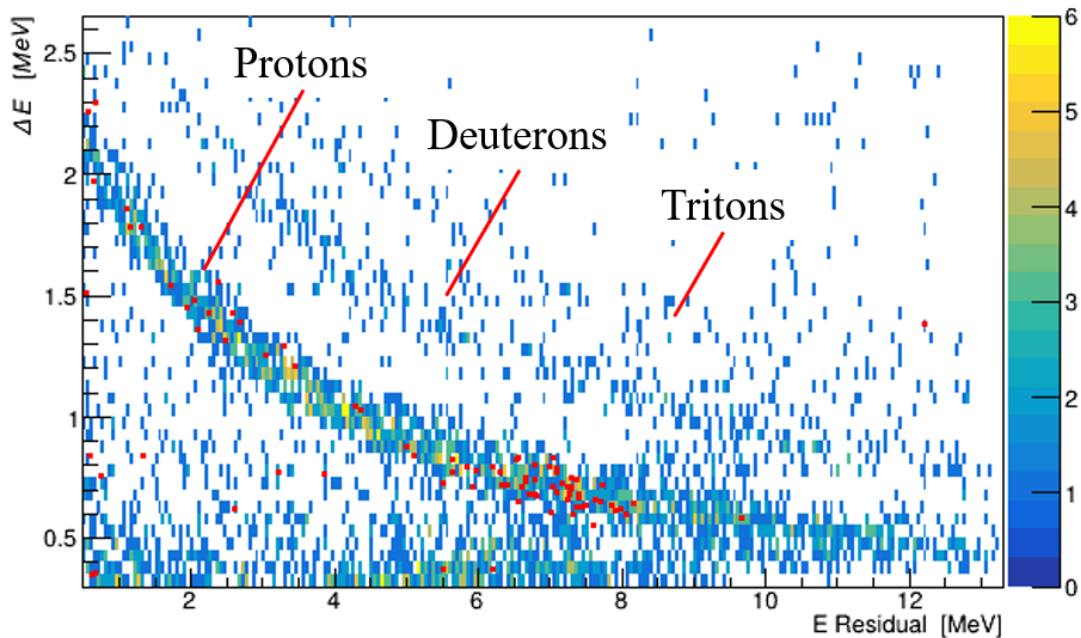


Figure 3.7: Particle Identification Plot (PID) of reaction products seen in one of the SIDAR detectors.  $\Delta E$  is the energy deposited in the thin layer and E residual is the energy deposited in the thick layer. Separation by mass is seen of protons, deuterons and tritons. The color scale shows the non-gated spectra of the charged particles detected in SIDAR; events where a coincident  $^{85}\text{Se}$  recoil was detected in the S800 are shown in red.

are used on the back-sides of the SuperX3 detectors. SIDAR is comprised of six YY1 detectors, which use 16 radially segmented non-resistive strips (both in the E and  $dE$  layers).

As previously mentioned, the ejectile proton energy increases with decreasing scattering angle; therefore the downstream barrel is required to be thicker to ensure the protons deposit their full energy at these angles. The measurement of energy loss with respect to total energy allows for particle identification based on the unique Bragg curves associated with each particle species. This enables deuterons or tritons originating from different reaction channels to be vetoed event-by-event. Figure 3.7 shows the Particle Identification spectrum (PID) for one SIDAR detector.

The detectors were calibrated using alpha particles from a triple-alpha radioactive source containing  $^{244}\text{Cm}$ ,  $^{241}\text{Am}$  and  $^{239}\text{Pu}$ . Running the ADCs briefly with no energy thresholds applied enabled a calibration point to be made for zero incident energy. Table 3.1 summarizes the alpha energies produced by the source, which together with the zero point calibration provided a calibration function for the range of proton energies expected from the measurement. Figure 3.8 shows the calibration procedure for non-resistive silicon strips. To calibrate the resistive-strips, the two contacts at either end of the strip must first be gain matched, before a calibration from ADC channel to energy can be made.

Table 3.1: Alpha energies and relative intensities from triple alpha source.

Isotope	Alpha energy [MeV]	relative intensity
$^{244}\text{Cm}$	5.805	76.9%
$^{244}\text{Cm}$	5.763	23.1%
$^{241}\text{Am}$	5.486	84.8%
$^{241}\text{Am}$	5.443	13.1%
$^{239}\text{Pu}$	5.157	70.77%
$^{239}\text{Pu}$	5.144	17.11%

For these calibrations, the source was placed inside the scattering chamber, at the target position. The isotropic,  $0.172\ \mu\text{Ci}$  source can then be used to measure the solid angle of each detector from the perspective of the target. Because the E layer measures the detector-proton interaction point (and therefore the polar scattering angle), the solid angles are of these detectors. Due to the incident angle of the incoming protons, some will hit the E layer, but not the dE (and vice versa). To account for this, only the (polar) angular range where protons *must* pass through both layers (a condition in the analysis) are included in the solid-angle measurements. To check the solid-angle measurements, a calculation of the ORRUBA barrel solid angle was performed using the Monte Carlo method. The simple rectangular shape of the ORRUBA detectors made

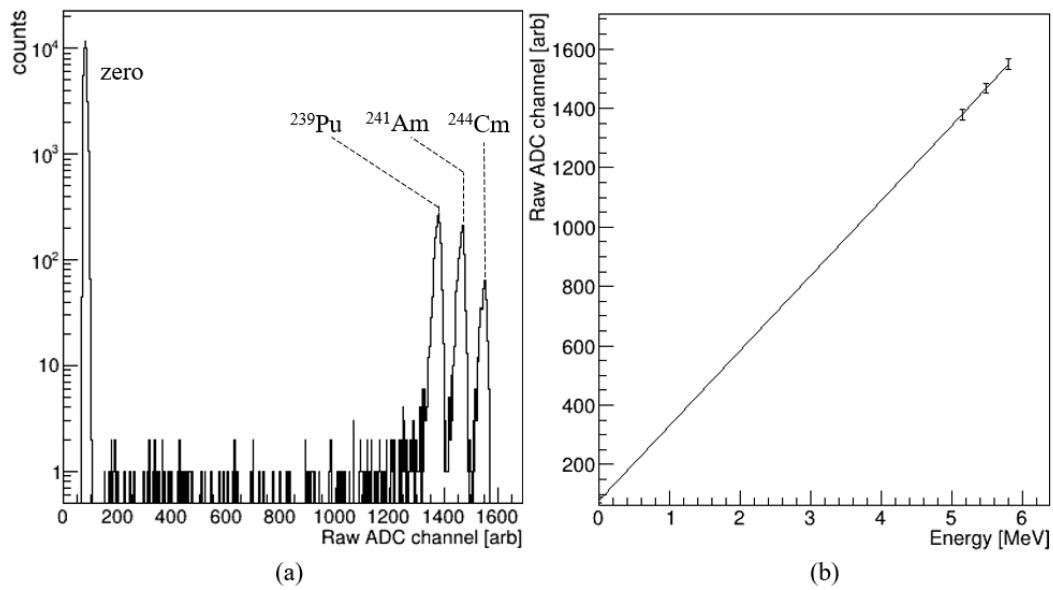


Figure 3.8: (a) Raw response of a single strip on a SIDAR detector to alpha particles from the triple alpha source, and a pedestal run with no detector thresholds for zero-point energy calibration. (b) Linear interpolation of four calibration points for the same detector to convert from ADC channel to incident particle energy [MeV]. Error bars represent the uncertainty in extracting the mean peak positions from the fits to the alpha peaks.

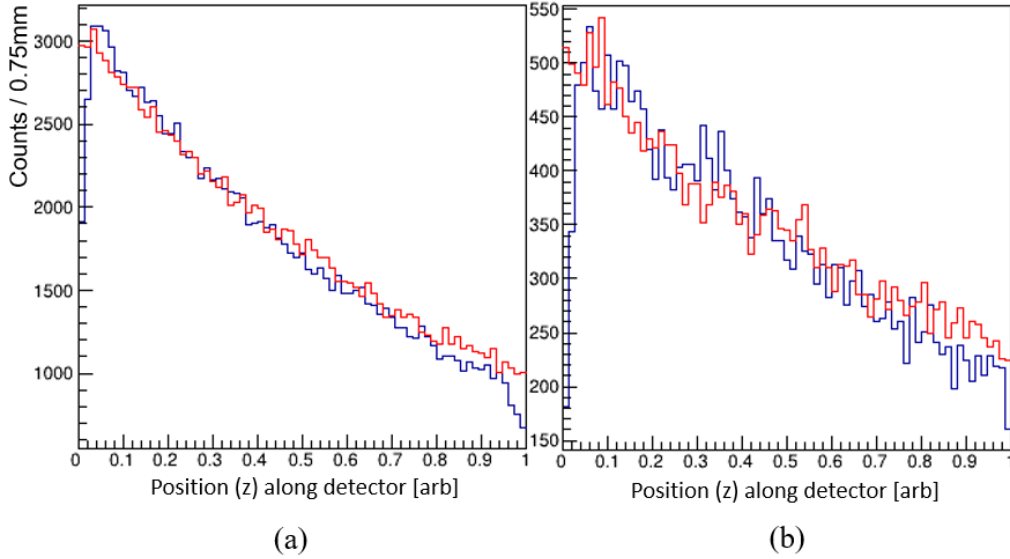


Figure 3.9: Number of alphas per 0.75mm across one ORRUBA detector face recorded (*blue*), and calculated through Monte Carlo (*red*). (*a*) Downstream ORRUBA barrel, and (*b*) upstream ORRUBA barrel.

them the appropriate choice for the cross check. The comparisons shown in Figure 3.9 are in agreement for both detector barrels. The extracted solid angles for each detector set are given in table 3.2.

Table 3.2: Extracted solid angles of each E layer detector type, per detector. Uncertainties are approximated using the difference between the Monte Carlo simulation, and the measured alpha particles.

Detector type	Solid angle per detector [sr]	Number of detectors
SIDAR	0.033(1)	6
Upstream ORRUBA	0.0204(8)	12
Downstream ORRUBA	0.111(2)	12

### 3.1.4 S800 mass spectrograph

The S800 magnetic spectrograph was required for this experiment to veto any unwanted reaction channels. In particular, reactions between the beam and the carbon in the target (fusion evaporation) generate an overwhelming number of protons, dominating

over the (d,p) reaction protons. Detecting the  $^{85}\text{Se}$  recoil using the S800 in coincidence with the reaction protons eliminates this background.

Figure 3.11 shows a schematic of the S800 with respect to the target position, and the detectors located at the focal plane. The S800 is a three-story tall, high-resolution and large-acceptance magnetic spectrograph, capable of separating and tracking heavy-recoil nuclei based on their magnetic rigidity for coincidence measurements with the proton from the (d,p) reaction. Located directly downstream of the target, two large dipole magnets precede gas and scintillator detectors at the focal plane. The gas detectors consist of two Cathode Readout Drift Chambers (CRDCs), used for recoil tracking, and an ion chamber for energy-loss measurements. The “E1” scintillator is located at the back of the focal plane.

A beam blocker located on the high-rigidity side of the magnet is used to block the unreacted beam, as the gas detectors limit the detection rate to  $\sim 5$  kHz. Without the beam blocker, the focal plane detectors would be overwhelmed by the unreacted beam. Due to the 1% momentum dispersion of the beam, there is an overlap between the unreacted  $^{84}\text{Se}$  beam (momentum centroid at 24.60 GeV/c), and the  $^{85}\text{Se}$  recoils of interest (momentum centroid at 24.71 GeV/c). As a result of this, the beam blocker stops the majority of  $^{85}\text{Se}$ , as well as the unwanted  $^{84}\text{Se}$ , in order stay under the S800 rate limit. Figure 3.10 shows a simulation of the  $^{85}\text{Se}$  magnetic rigidity, with the centroid of the unreacted beam shown in purple. The beam-blocker position necessary to block the unreacted  $^{84}\text{Se}$  beam with a 1% (blue) and 0.5% (green) momentum dispersion is also shown. Everything to the left of the beam-blocker positions is blocked from reaching the S800 focal plane. The beam blocker was retracted as far as possible for the measurement, pushing the focal-plane detection rate to its limit.

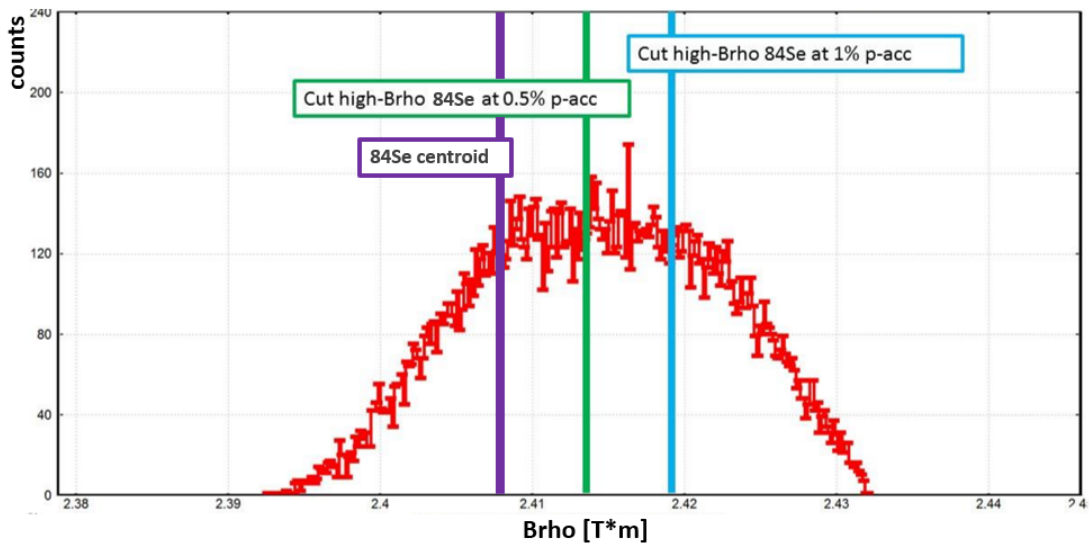


Figure 3.10: Simulated magnetic rigidity of the  $^{85}\text{Se}$  recoil (red) at the S800 beam blocker. The centroid of the unreacted  $^{84}\text{Se}$  beam is shown in purple. Beam-blocker positions to stop the  $^{84}\text{Se}$  beam at 1% (blue) and 0.5% (green) momentum dispersions are also shown. Adopted from Reference [Pai18b]

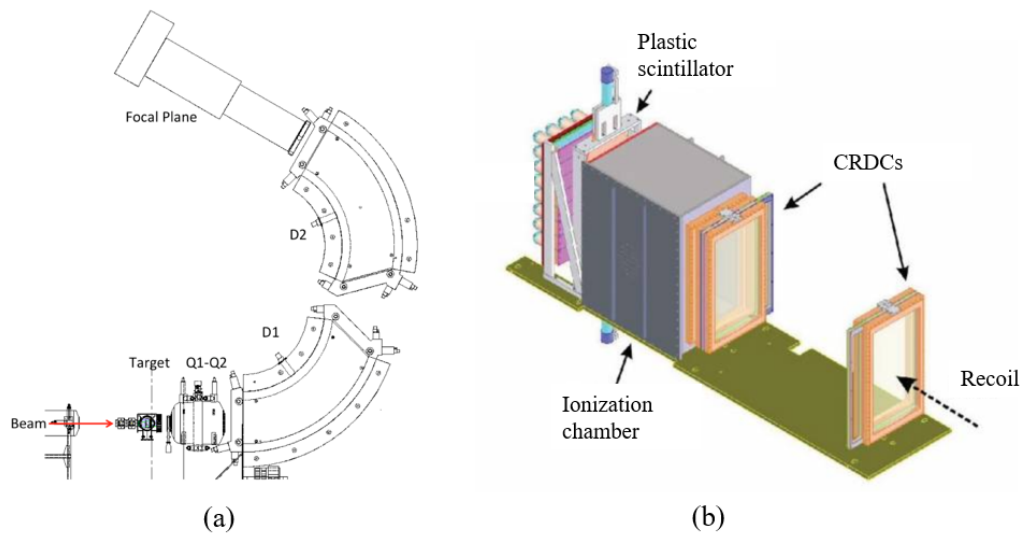


Figure 3.11: (a) Schematic showing the S800 mass spectrograph in relation to the experimental target position. (b) Cartoon of the focal plane detectors deployed [Per20].

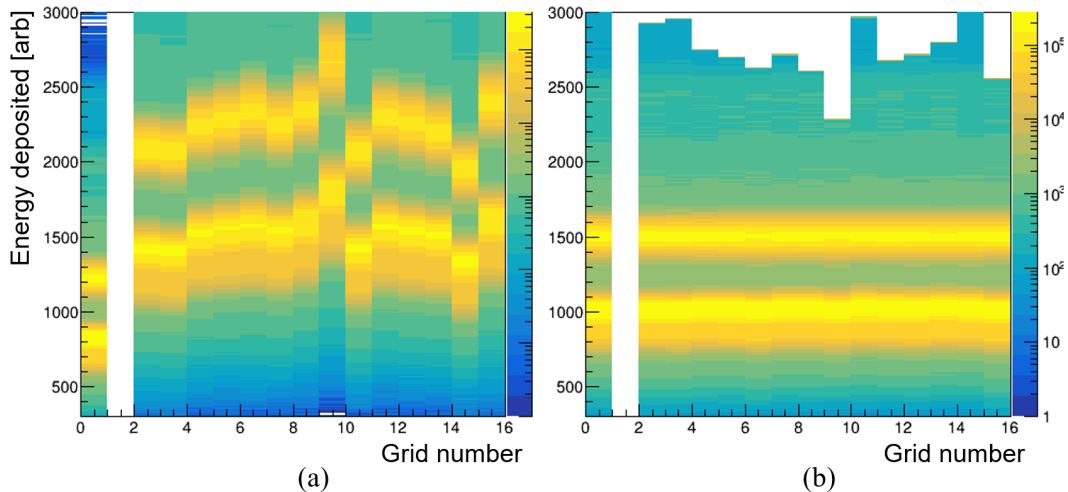


Figure 3.12: Energy response of the ion chamber grids (a) uncalibrated, and (b) gain matched relative to each other.

The CRDCs are only capable of tracking recoils in the non-dispersive plane, as the dispersive plane includes a degeneracy from the recoil energy. As no recoil total-energy measurement was used in this experiment, the tracking was not sufficient to provide the beam-target interaction position, and so was not used for this analysis. However, the S800 is fitted with a full-energy measuring Hodoscope at the back of the focal plane, which was not used for this experiment. In future experiments, this could be turned on to measure the full energy of the recoil, informing the S800 CRDC tracking in the dispersive plane.

The ionization chamber consists of perpendicular grids of anodes and cathodes held at voltage surrounded by P10 gas (90% argon, 10% methane) at a typical pressure of 300 torr. The recoil ionizes the gas as it passes through, depositing a specific amount of energy according to the mass, charge and energy of the recoil. Each anode segment has an associated pre-amplifier and shaping amplifier. The anodes therefore need to be gain matched to infer the relative energy loss of different isotopes. Figure 3.12 shows the gain-matched energy spectrum compared to the raw.

The E1 scintillator at the back of the S800 provides a timing reference for time-of-flight measurements, relative to a given time from either the cyclotron RF signal, the XF scintillator in the A1900, the MCPs or the silicon detectors in ORRUBA and SIDAR. These timing signals are used as a proxy for the beam energy, and are combined with the energy loss in the ion chamber for recoil identification.

### 3.1.5 Data Acquisition

The configuration of this experiment required the merging of two data acquisitions (DAQs): ORRUBA using ORPHAS and the S800 using the NSCL DAQ. A logic diagram of the setup is shown in Figure 3.13. The DAQ trigger is produced from an OR of the triggers from the ORRUBA detectors, and the (prescaled by  $2^{14}$ ) MCP detectors. The trigger used to start a V775 TDC operated in common start mode, with a  $1 \mu\text{s}$  full scale. Delayed “stops” from the ORRUBA detectors, prescaled MCPs, XF scintillator, cyclotron RF and E1 scintillator are then recorded in the TDC, to deconvolve the different trigger types. This also allows for timing measurements between different detectors, providing time-of-flight measurements of the beam. Counting the prescaled MCP self-stops (where the acquisition is both started and stopped by the MCP) provides a measurement of the beam current.

When a trigger starts the acquisition, the CAEN V785 Analogue to Digital Converter (ADC) is put in peak-sensing mode to digitize the detected signals. The gate for this was  $\approx 2 \mu\text{s}$ , with a shaping time of  $0.5 \mu\text{s}$ . A “busy” signal is then sent back to the trigger logic, such that additional signals are vetoed while the event is being recorded. The vetoed master ORRUBA trigger is then sent to the S800 DAQ. The S800 acts as a slave to the ORRUBA master, such that only when the master ORRUBA trigger is

sent to the S800 is data processed from the focal-plane detectors and read out using the NSCL DAQ.

The events from the two otherwise independently operating data acquisition systems are synchronized by means of timestamping. Timestamps originate from the ORRUBA DAQ, using the 10 MHz clock from the SIS3820 Scaler module. A veto from the ORRUBA DAQ trigger module ensures the master 10MHz clock is only running when the ORRUBA DAQ is not busy. The livetime of the ORPHAS DAQ was determined using the vetoed and raw 100 Hz clock. The S800 livetime is accounted for in the calculation of the S800 acceptance. The master clock is then sent to the S800 DAQ to timestamp the S800 data. These timestamps are then used to merge the events from ORRUBA and the S800.

Digitized ORRUBA data is written directly to disk, and broadcast via TCP/IP to “RON BOX1”, which formats the ORRUBA data so that it can be processed in the Master Event Builder (MEB) to provide online data analysis. The S800 data is already in a readable format, and so is sent straight to the MEB. The merged data is then written to disk, and sent directly to DAQ computers for online analysis.

### **3.1.6 Analysis**

In the present study, a radioactive beam of  $^{84}\text{Se}$  was incident on a  $1200 \mu\text{g}/\text{cm}^2$   $\text{CD}_2$  target, with the reaction protons detected in coincidence with the heavy recoil. SIDAR (Silicon Detector ARray) and ORRUBA were both deployed upstream of the target to capture the backward-angle focused reaction protons.

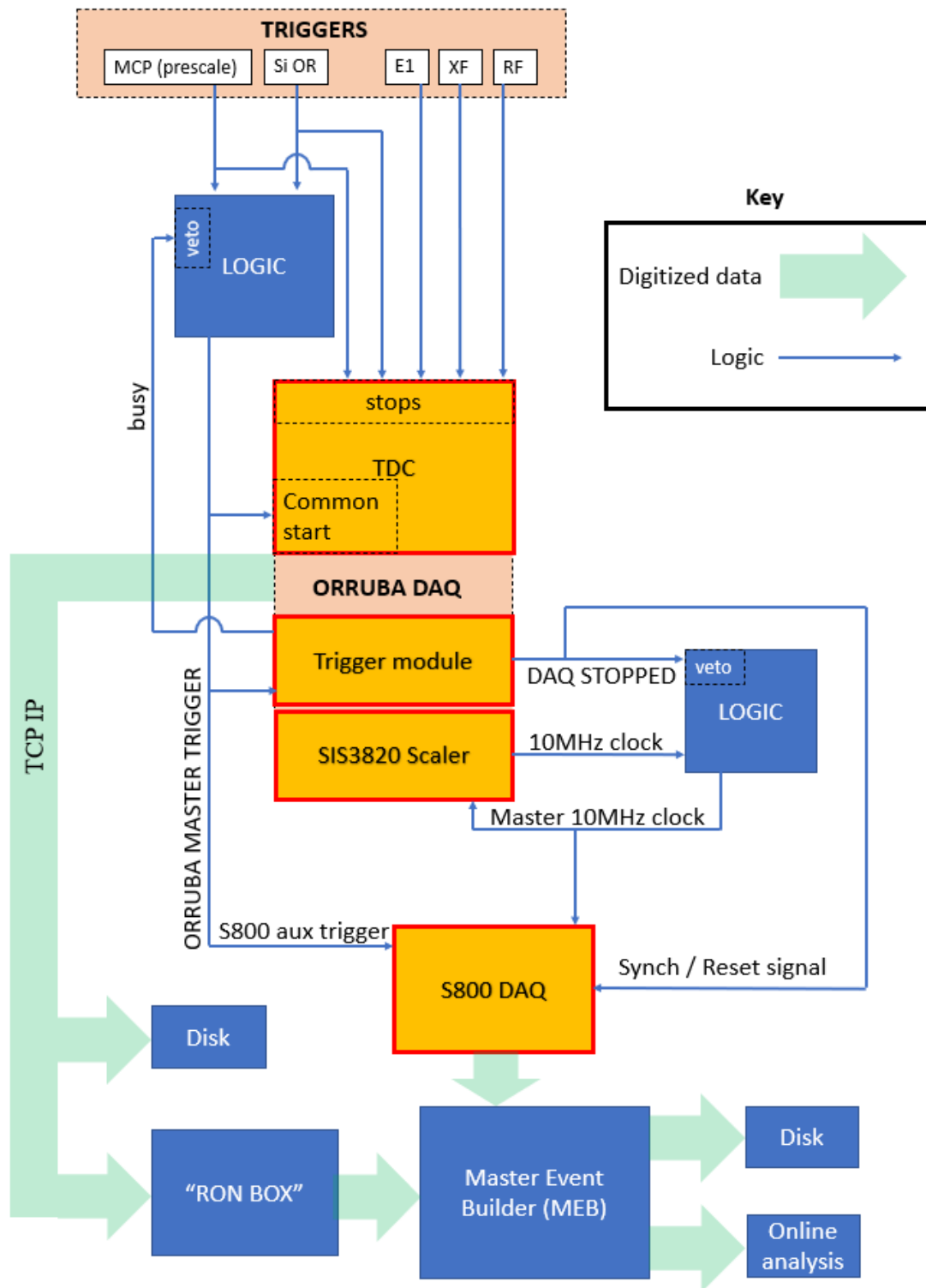


Figure 3.13: Logic diagram of the ORRUBA and S800 Data Acquisition (DAQ) setup. Logic signals are denoted by the thin blue lines, whereas the digitized data is represented by the thick green arrows.

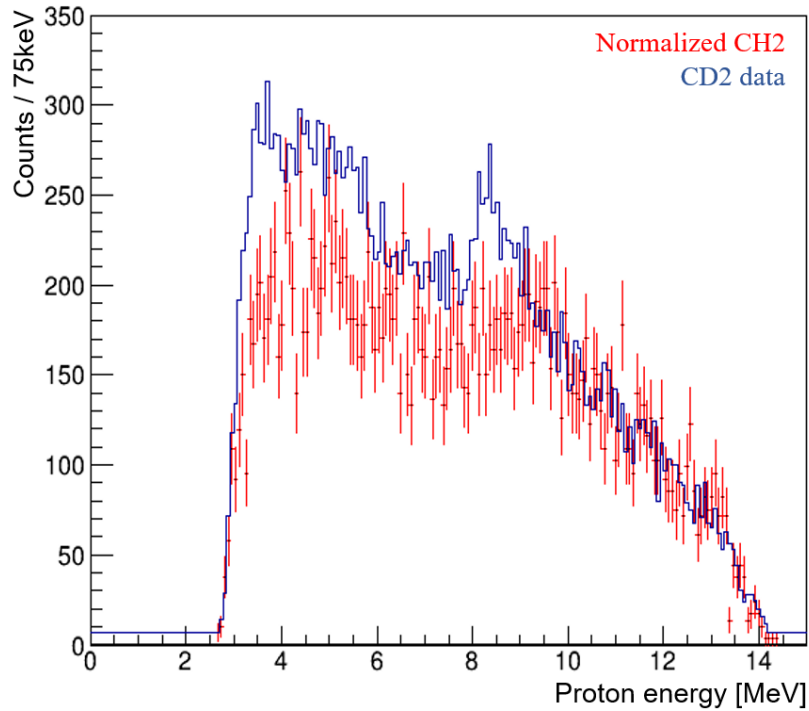


Figure 3.14: Proton energy spectrum detected in SIDAR with  $^{84}\text{Se}$  beam incident on a  $\text{CD}_2$  target (blue) and  $\text{CH}_2$  target (red). The  $\text{CH}_2$  proton energy spectrum was scaled using a linear fit to the  $\text{CD}_2$  data between 10 and 14 MeV - a region corresponding to negative excitation energy for  $^{84}\text{Se}(\text{d,p})$  protons and therefore a good estimation of the background. Uncertainties in the scaled data are statistical.

Recoil tagging from the S800 provided significant background rejection. The dominating contribution to the background is from reactions between the beam and the carbon in the target. To further understand the background spectrum, data were recorded using a non-deuterated ( $\text{CH}_2$ ) target for 10 hours. Figure 3.14 shows the proton energy spectrum for a subset of strips in SIDAR using the  $\text{CD}_2$  target, overlaid with the (scaled) data taken using the  $\text{CH}_2$  target. At proton energies above  $\approx 9$  MeV, no (d,p) transfer data is expected, as this corresponds to an unphysical negative excitation energy. In this region, the background  $\text{CH}_2$  data was normalized to the magnitude of the  $\text{CD}_2$  data. The shape of the background spectrum is in good agreement with that from the  $\text{CD}_2$  target at proton energies larger than 9 MeV; the (d,p) protons from the

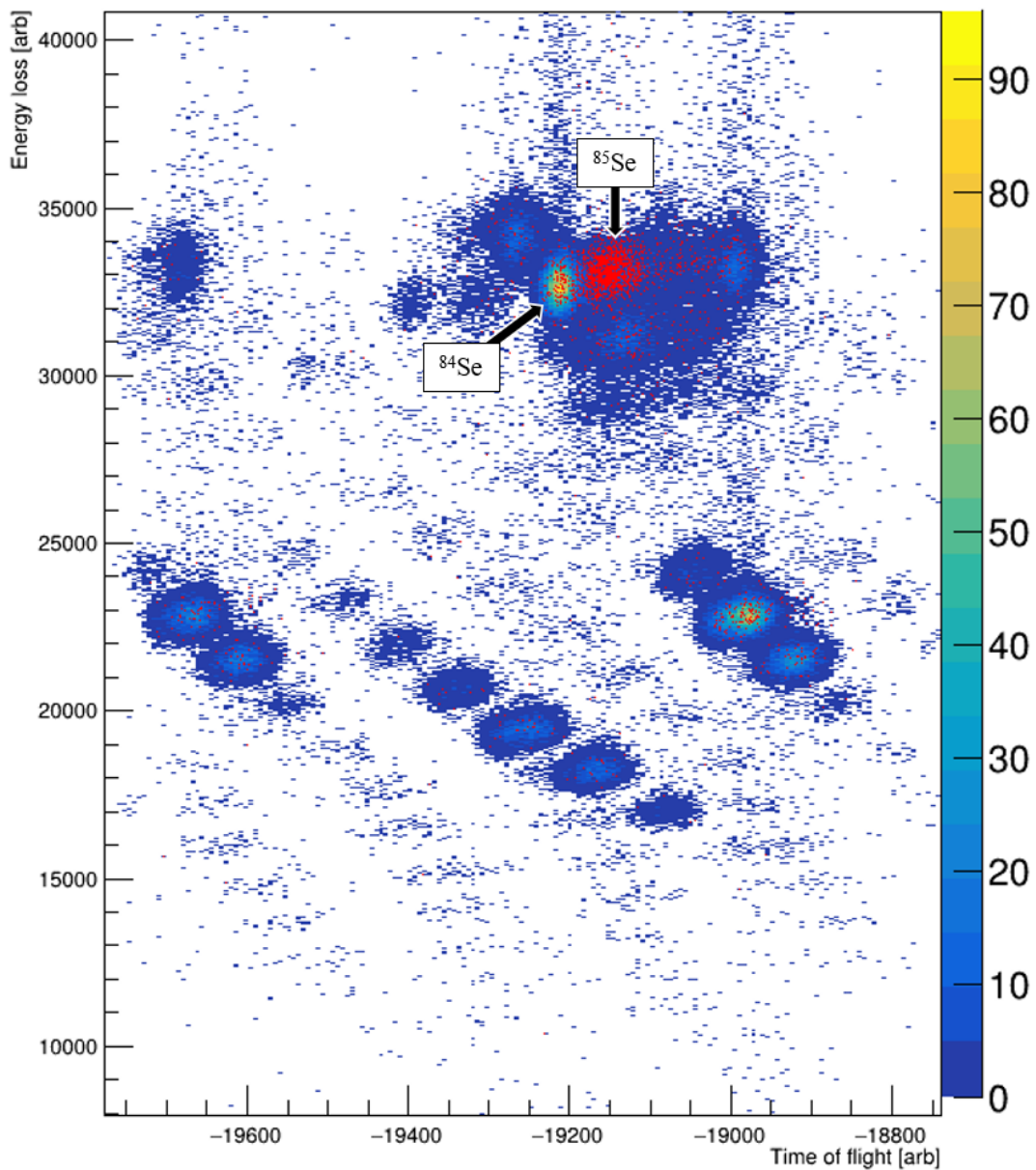


Figure 3.15: Energy loss in S800 ion chamber vs time of flight between the S800 E1 scintillator and cyclotron RF to provide PID and recoil tagging. The color scale represents all data seen in S800; coincidences with protons seen in ORRUBA and SIDAR are red.

CD<sub>2</sub> target clearly stand out at  $\approx 8$  MeV. Although the (d,p) transfer peaks can be seen in the CD<sub>2</sub> data, the statistics of the particle-singles data is insufficient to do a background-subtracted analysis after dividing the data into angular bins. Requiring a <sup>85</sup>Se recoil nucleus to veto any other reaction channels is therefore critical to extracting the neutron-transfer cross section.

A PID spectrum from the S800 isolating <sup>85</sup>Se from other reaction products is shown in Figure 3.15. Energy loss in the ionization chamber, and time of flight between the E1 scintillator at the S800 focal plane and the cyclotron RF signal were measured for the recoil particles. Coincidences between a recoil seen in the S800, and protons in ORRUBA and SIDAR are shown in red, and locate the <sup>85</sup>Se for recoil tagging.

Challenges were, however, encountered when measuring the ejectile protons in coincidence with the <sup>85</sup>Se recoil. As described in section 3.1.4, overlap between the unreacted <sup>84</sup>Se and the <sup>85</sup>Se recoil in magnetic rigidity significantly restricts the opening of the beam blocker. As a result of the initially conservative placement of the beam blocker, only the final 40% of the data have the recoil coincidence available. Proton singles were recorded for the entire experiment.

Gating on the <sup>85</sup>Se directly in the S800, and recording the energy and scattering angle of the ejectile proton in coincidence removes the background originating from other reactions between the beam and carbon in the target, as the <sup>85</sup>Se recoil would not be measured in coincidence otherwise. Figure 3.16 shows the energy - angle systematics for the <sup>85</sup>Se coincidence gated protons. Converting to the center-of-mass frame, the reaction Q value can be reconstructed event-by-event using the beam energy, proton energy, scattering angle and masses for the reaction X<sub>1</sub>(X<sub>2</sub>,X<sub>3</sub>)X<sub>4</sub> [Mar68].

$$Q = M_1 + M_2 - M_3 - \left( M_1^2 + M_2^2 + M_3^2 + 2M_2E_1 - 2E_3(E_1 + M_2) + 2P_1P_3\cos(\theta) \right)^{1/2} \quad (3.1)$$

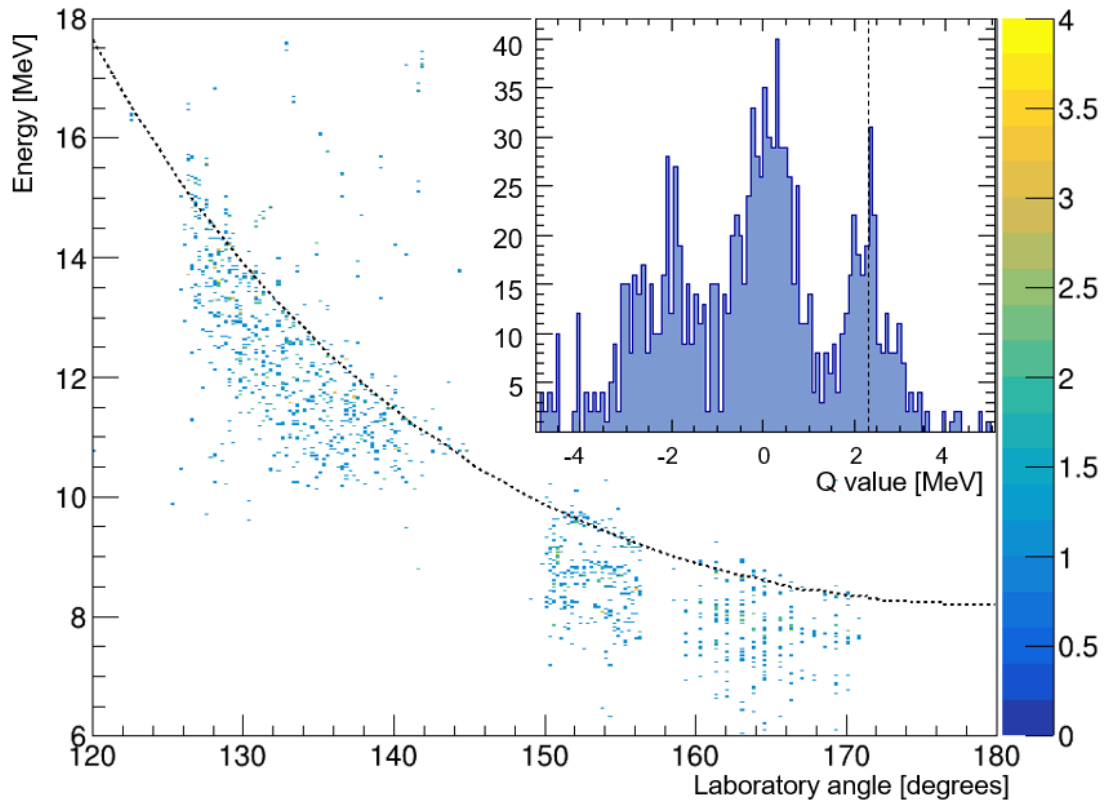


Figure 3.16: Energy and angle of protons observed in the silicon detectors in coincidence with a recoil in the S800. A kinematic line of the predicted ground state transfer is overlaid. *inset*, Q value spectrum from the upstream ORRUBA barrel and SIDAR data. The ground state Q value of 2.312 MeV is highlighted.

Figure 3.16 (*inset*) shows the Q value spectrum for the data with a scattering angle of more than  $150^\circ$  in the laboratory frame. Equation 3.1 shows that the Q-value resolution is sensitive to the energy and angular resolution of the detected protons. An increase in the observed width of the states is therefore predicted at larger scattering angles because the angular resolution becomes a greater component of the Q value resolution due to the steeper kinematics. The decreasing distance between the target and the detector faces at these angles also reduces the angular resolution. An uncertainty in the reaction energy due to the finite thickness of the target is also a contributing factor that affects the resolution across all scattering angles. This has a smaller contribution, however, than other parameters such as the momentum dispersion of the beam.

The expected Q-value resolution as a function of scattering angle is calculated using the Monte Carlo simulation code VIKAR v4.2 [Pai18a], as shown in Figure 3.18. This information fixes the widths used in the fits to the states - reducing the uncertainty in the yields for each angular bin. A detailed spectroscopic analysis has only been applied to the  $5/2^+$  ground state and  $1/2^+$  first excited state. At higher excitation energies, the density of states is too high for the resolving power of the experiment. The fits to ground state (Q=2.312 MeV) and first-excited state (Q=1.85 MeV) in the polar-angle segmented Q value spectra, using fixed centroids and widths are shown in Figure 3.17. The resolution can be seen to worsen as a function of decreasing laboratory angle, reflecting the larger sensitivity of the Q value to the measurement of the scattering angle. Fits to additional excited states at energies of 1.531 MeV, 2.003 MeV and 2.451 MeV are also included, to ensure that no strength from these excited states is being stolen from the fits to the ground- and first-excited state (or vice versa). These excited states were chosen in the fits because states with the same spin-parities in

neighboring isotones show stronger spectroscopic factors, such that it is reasonable to expect some spectroscopic strength in these states in  $^{85}\text{Se}$ .

Table 3.3: Resolution and integrated counts per angular bin. Stated uncertainties are purely statistical.

Angular bin	Detector	FWHM (keV)	5/2 <sup>+</sup> counts	1/2 <sup>+</sup> counts
158° - 171°	SIDAR	650	37 ± 7	12 ± 5
149° - 156.5°	Up ORRUBA	750	28 ± 7	14 ± 6
136° - 147°	Down ORRUBA	960	30 ± 11	15 ± 11
126° - 136°	Down ORRUBA	1200	40 ± 12	23 ± 14

Yields extracted for the ground- and first-excited state as a function of angle must then be normalized to the beam flux, target thickness, detector solid angle and S800 acceptance to produce an absolute differential cross section:

$$\frac{d\sigma}{d\Omega} = \frac{10^{27}}{n_B n_T \epsilon_{S800}} \frac{dN(\theta_i)}{d\Omega(\theta_i)} \frac{\Delta\Omega_i^{lab}}{\Delta\Omega_i^{cm}} \quad (3.2)$$

Equation 3.2 shows the differential cross section calculated from the number of ejected protons detected per steradian  $\frac{dN(\theta_i)}{d\Omega(\theta_i)}$ , normalized by the integrated beam current  $n_B$  and target density  $n_T$ , detector solid angle  $\Delta\Omega_i^{lab}$  and S800 acceptance  $\epsilon_{S800}$ . A relativistic Jacobian  $\frac{\Delta\Omega_i^{lab}}{\Delta\Omega_i^{cm}}$  boosts the solid angle from the lab frame to the center of mass frame.

Extracting the integrated beam flux of  $^{84}\text{Se}$  requires knowledge of both the total beam current and the beam purity. For the present study, the purity and total current was recorded for the entire experiment through time-of-flight measurements and prescaled counting from the MCPs. The beam time-of-flight was recorded in two ways: between the XF-scintillator and the upstream MCP, and between the Cyclotron RF and the upstream MCP.

The upstream MCP to cyclotron RF time-of-flight includes a flight path of the beam at the pre-degrader energy, and the post-degrader energy (before and after the beam

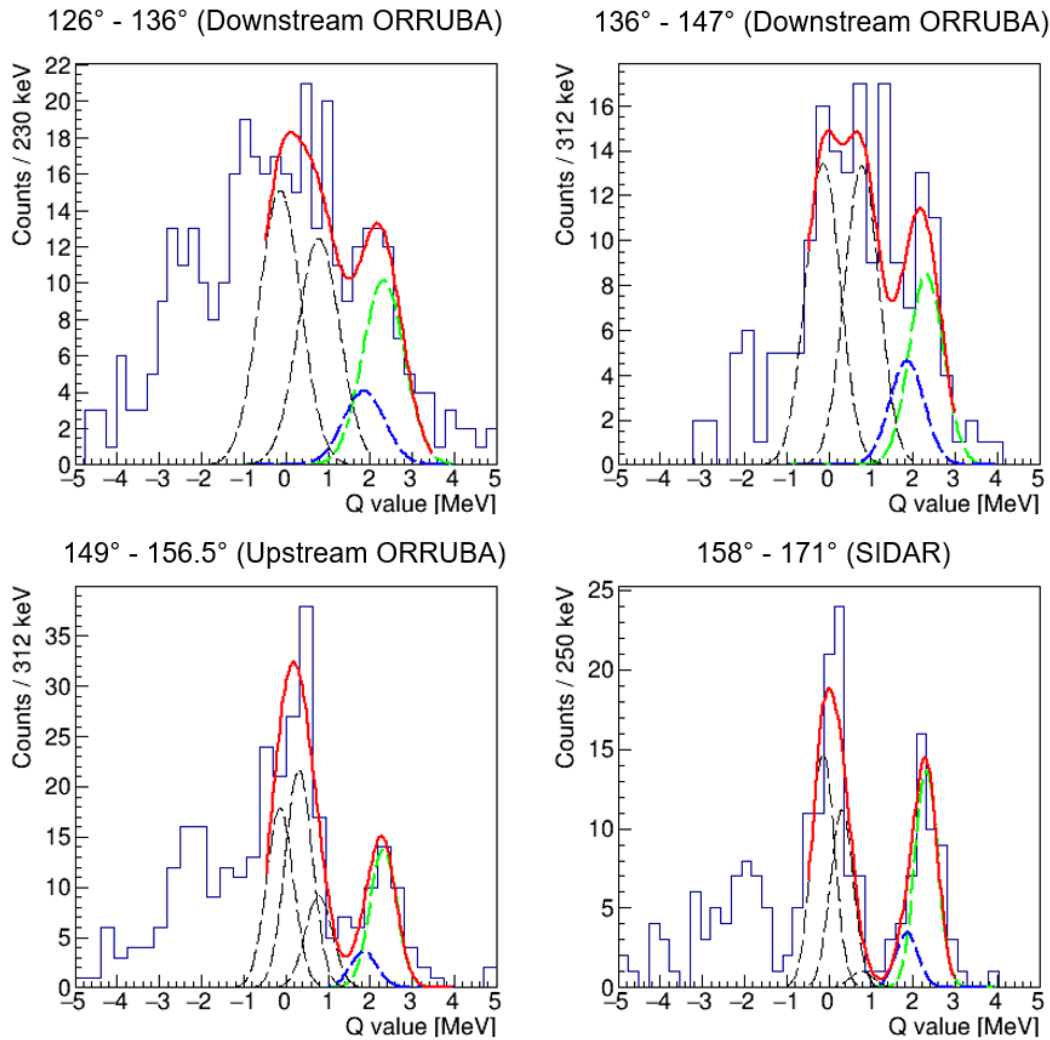


Figure 3.17: Q value spectra for each angular bin analyzed. The ground state ( $Q=2.312$  MeV) fit (green) and the first excited state ( $Q=1.85$  MeV) (blue) are fit with means and widths fixed according to the VIKAR Monte Carlo simulation. Fits to states at higher excitation energies are also included, such that their yields are not included in fits to the ground- and first-excited states.

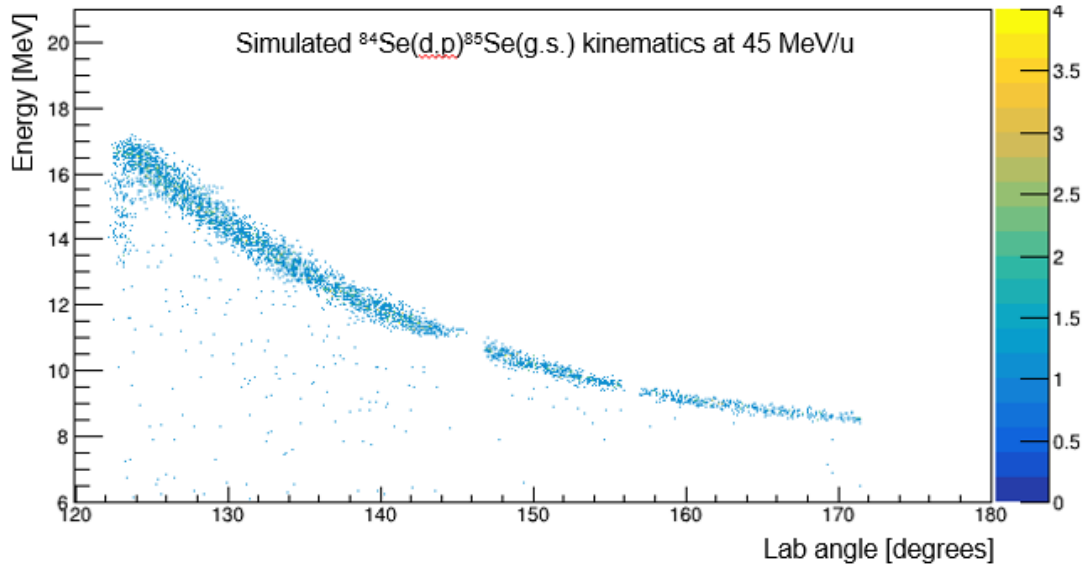


Figure 3.18: VIKAR Simulated kinematics of  $^{84}\text{Se}(d,p)^{85}\text{Se}(g.s.)$  at 45 MeV/u. Input parameters are as follows: Beam spot size = 6mm, Beam divergence =  $1^\circ$ , momentum dispersion = 1%. No position reconstruction from beam tracking was used in order to remain consistent with the experiment.

passes through the degrader wedge at the image-two position). The upstream MCP to XF scintillator flight path only includes the post-degrader energy of the beam. An event-by-event comparison of the two time-of-flights provides separation of the beam species. The relationship between the two time-of-flight measurements is displayed in Figure 3.20. The main components of the beam composition were identified to be  $^{84}\text{Se}$  and  $^{84}\text{Br}$ , by examining the S800 particle identification spectrum (as in Figure 3.15) when gating on the different beam component peaks. Projecting Figure 3.20 onto a diagonal axis, the purity of these beam components can be extracted through Gaussian fits, shown in Figure 3.21. The beam composition was 76.4(3)%  $^{84}\text{Se}$  and 14.3(3)%  $^{84}\text{Br}$ , with traces of other beam contaminants making up the final 9.3%.

The integrated beam flux was calculated using the prescaled (down-scaled by  $2^{14}$  to not overload the DAQ) upstream MCP rate. The data acquisition is started with an

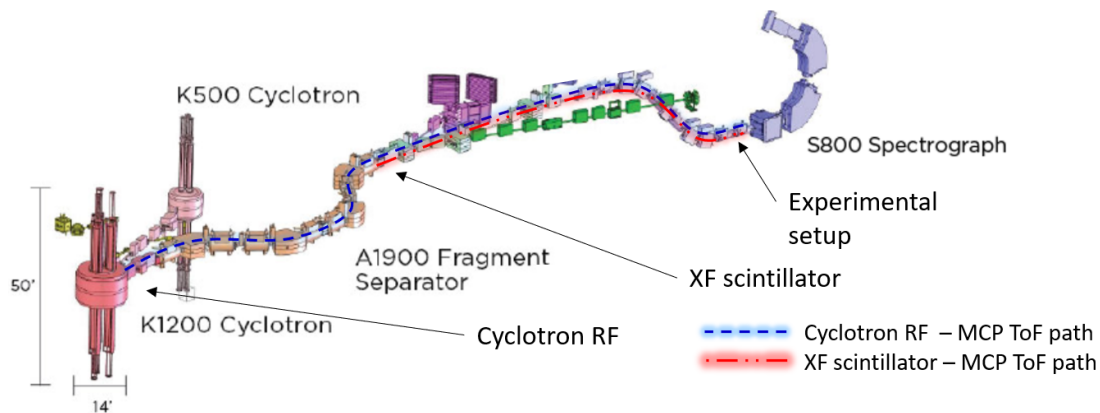


Figure 3.19: Time of flight paths used for beam composition determination. Two time-of-flight paths used: Cyclotron RF - Upstream MCP and XF scintillator - Upstream MCP. Adopted from [Sco16].

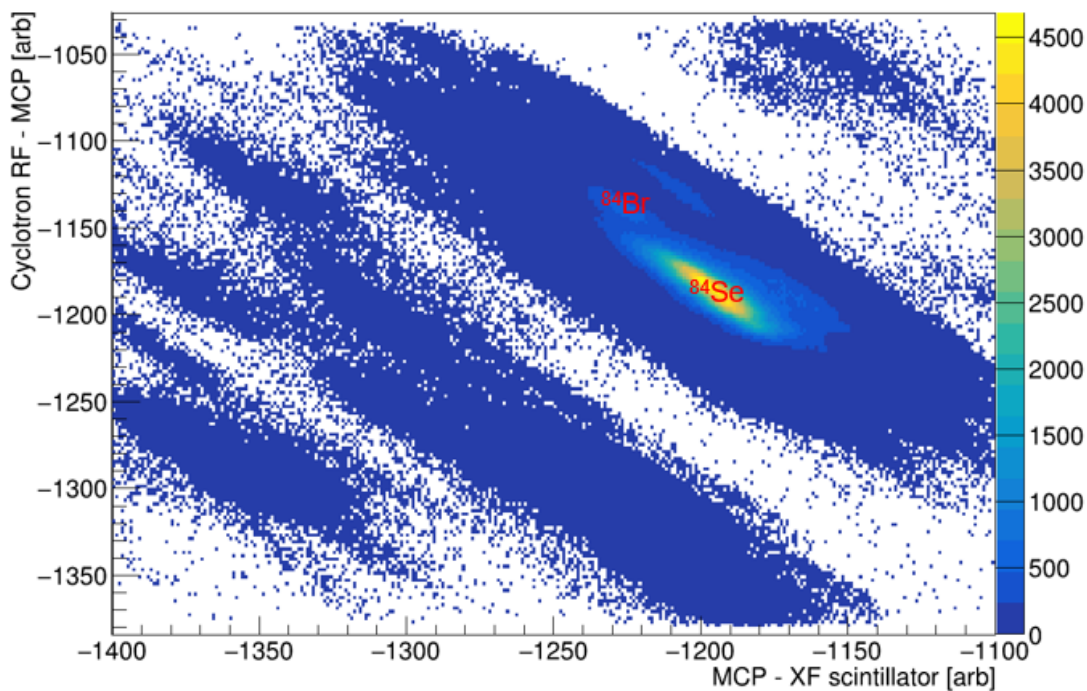


Figure 3.20: Time-of-flight between the Upstream MCP and the Cyclotron RF measured against the time of flight between the Upstream MCP and the XF scintillator. The two main beam species identified are  $^{84}\text{Se}$  and  $^{84}\text{Br}$ .

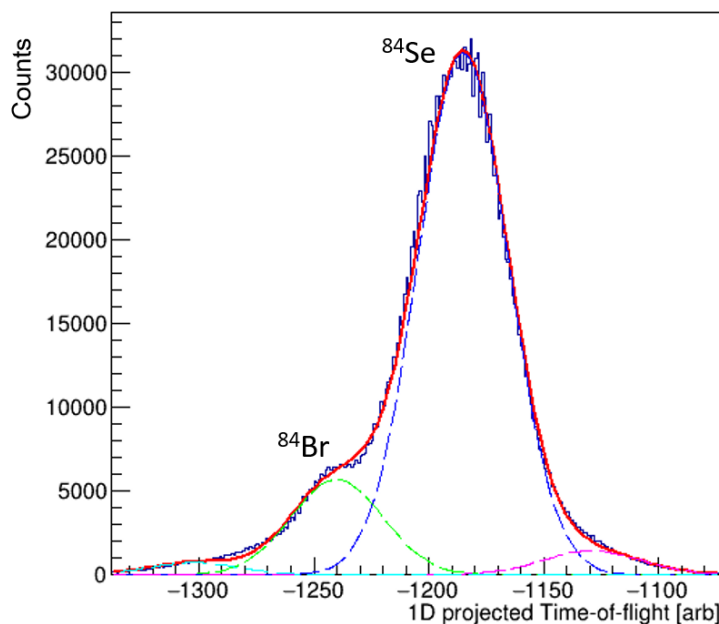


Figure 3.21: Projection of Figure 3.20 onto diagonal axis to calculate percentage composition of beam species via Gaussian fits. The red line is the total fit, dashed lines show individual contributions of  $^{84}\text{Se}$  (blue),  $^{84}\text{Br}$  (green) and traces of other unidentified contaminants (cyan, magenta).

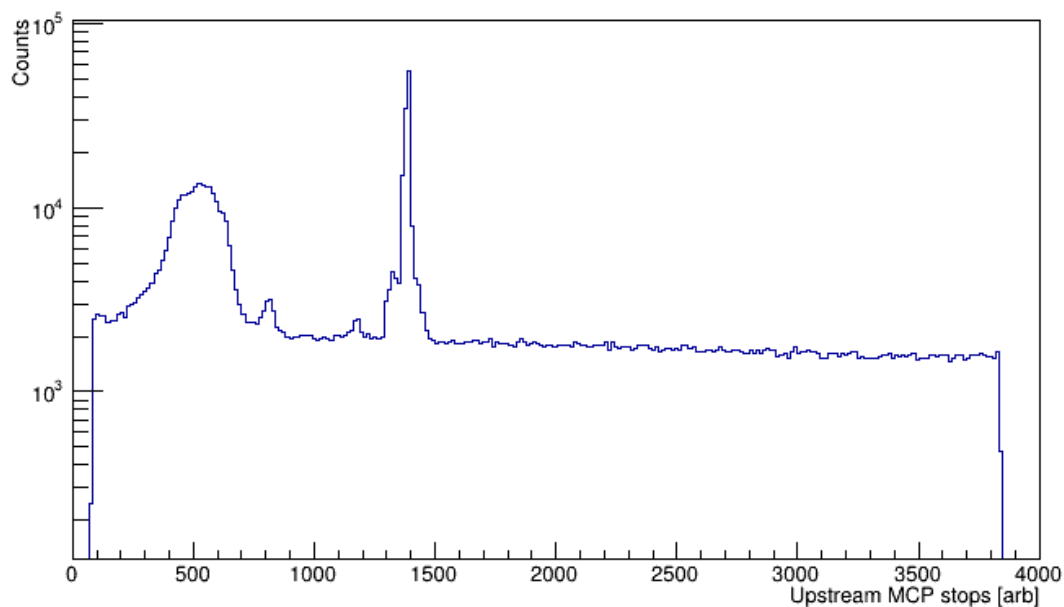


Figure 3.22: Upstream MCP acquisition “stop” spectrum, where the starts were from an OR of the silicon detectors and both of the MCPs. The large broad peak (*left*) is from the silicon starts, the sharp peak is from the MCP starts. The full scale is  $1\ \mu\text{s}$ .

OR of the triggers from the two MCPs and the silicon detectors. After the acquisition has been started, the trigger from each detector set can then be recorded as the acquisition “stop”. The “stop” spectrum from the upstream MCP is shown in Figure 3.22, where the broad peak describes the slow timing signal from the silicon starts, and the sharp peak is a result of the fast MCP starts. Gating on events where the acquisition was started by the MCP, the total number of beam particles that pass through can be calculated. Random acquisition start events are flat and predictable, and so are subtracted with negligible uncertainty. The efficiency of the upstream MCP was calculated to be 98.3(8)% using the percentage of events observed in the upstream MCP when a signature was seen in the downstream MCP as well as a proton detected in the silicon, as a beam particle must have been present.

The beam intensity was recorded for the duration of the experiment, allowing for a dynamic calculation of the  $^{84}\text{Se}$  rate on target. Figure 3.23 shows the rate as a function of time over the experiment. Contributions to the uncertainty originate from the beam purity fit uncertainty and uncertainty in the MCP efficiency. This gives the integrated  $^{84}\text{Se}$  beam on target as  $3.21 \pm 0.03 \times 10^{10}$  particles.

The areal density of the  $\text{CD}_2$  target was deduced to be  $1200 \pm 130 \mu\text{g}/\text{cm}^2$ , by measuring the energy loss of alpha particles (from the triple-alpha source described in Table 3.1) through the target using a  $1000\mu\text{m}$  thick SuperX3 detector. Solid deuterated polyethylene targets generally are not *fully* deuterated - a small percentage remains as hydrogen. For lower energy reactions this can be quantified through elastic scattering; however, the large reaction energy in this measurement makes this impossible, as the elastic scattering cannot be modelled as Rutherford scattering. For this measurement, a hydrogen percentage of  $5\% \pm 2\%$  was assumed, consistent with previous measurements

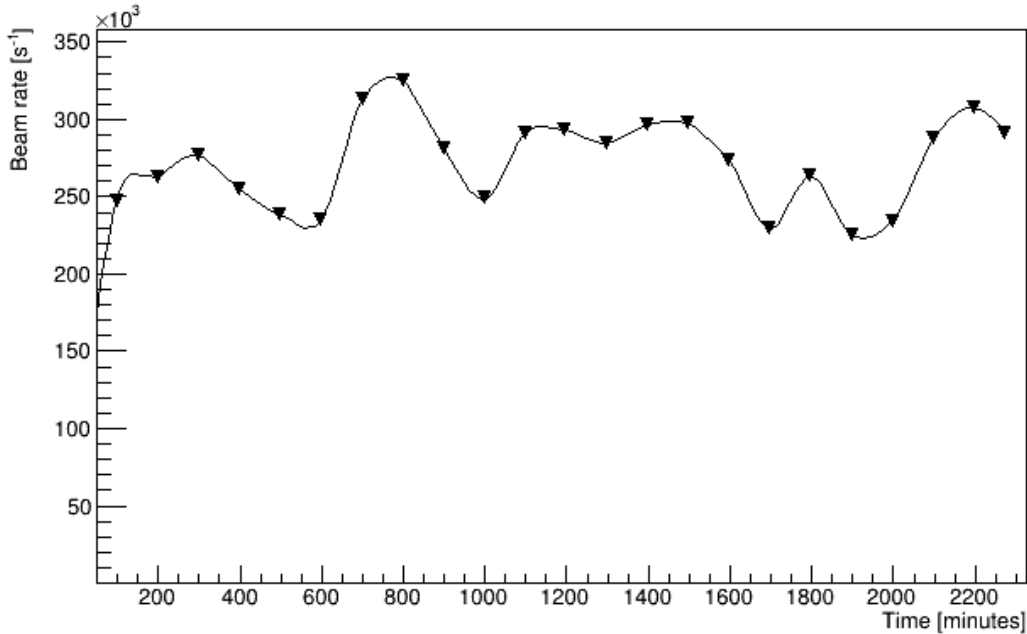


Figure 3.23: Total (all beam species) rate as a function of time over the experiment. Uncertainties are statistical, and too small to be seen.

using targets manufactured in identical fashions [Feb17]. Therefore, the target thickness corresponds to  $8.6 \pm 0.9 \times 10^{19}$  deuterons/cm<sup>2</sup>.

Rate-limiting gas detectors in the S800 restrict the ability to capture all of the <sup>85</sup>Se recoils. The momentum spread of the beam, together with the similarity in magnetic rigidity between the beam and the recoil, necessitates a blocker in front of the S800 focal plane so as to not overwhelm these detectors with the unreacted beam. This results in a fraction of the recoils of interest also being blocked. It is, therefore, critical to quantify the acceptance of the S800, to normalize the yield to an absolute differential cross section.

To calculate the S800 acceptance, the particle singles data (no recoil coincidence required) was compared to the S800 coincidence data. This was done using data from SIDAR, as the background is smallest at large scattering angles. A background subtraction was applied to the particle singles data using the scaled CH<sub>2</sub> data, and a

comparison of the yields was made. Figure 3.24 shows this for both the recoil coincident, and non-coincident data.

The largest peak of states at  $\sim 0$  MeV Q value can be used to calculate the S800 acceptance, via a Gaussian fit for the background-subtracted and S800-coincident data. Forcing the widths of the background-subtracted and S800-coincidence peaks to be consistent with each other, the S800 acceptance is calculated to be  $26.9\% \pm 4.3\%$ . The uncertainty comes from the best fit uncertainty of the amplitude of the two Gaussian fits. A cross check of the S800 acceptance can be calculated by integrating the counts between the ground-state Q value (2.312 MeV) and the neutron separation energy (-2.225 MeV) for both the S800 coincident and background-subtracted data. This yields the S800 acceptance to be  $24.7\% \pm 4.5\%$ . The uncertainty was calculated to include statistical uncertainties from the S800 coincidence and non-coincidence  $\text{CD}_2$  data, and the background  $\text{CH}_2$  data. The livetime of the S800 is inherently included in calculations of the S800 acceptance, and so does not need to be additionally included.

Due to the “kick” the proton gives the recoil nucleus, it is necessary to check that the S800 acceptance was azimuthally symmetric. Calculating the ratio of S800-coincident events to non-coincident events as a function of azimuthal angle yielded no asymmetries within statistical uncertainties.

Table 3.4: Experimental normalization parameters

Normalization parameter	value
Target thickness	$8.6 \pm 0.9 \times 10^{19}$ deuterons/cm <sup>2</sup>
Integrated beam	$3.21 \pm 0.02 \times 10^{10}$ particles
S800 acceptance	$26.9\% \pm 4.3\%$

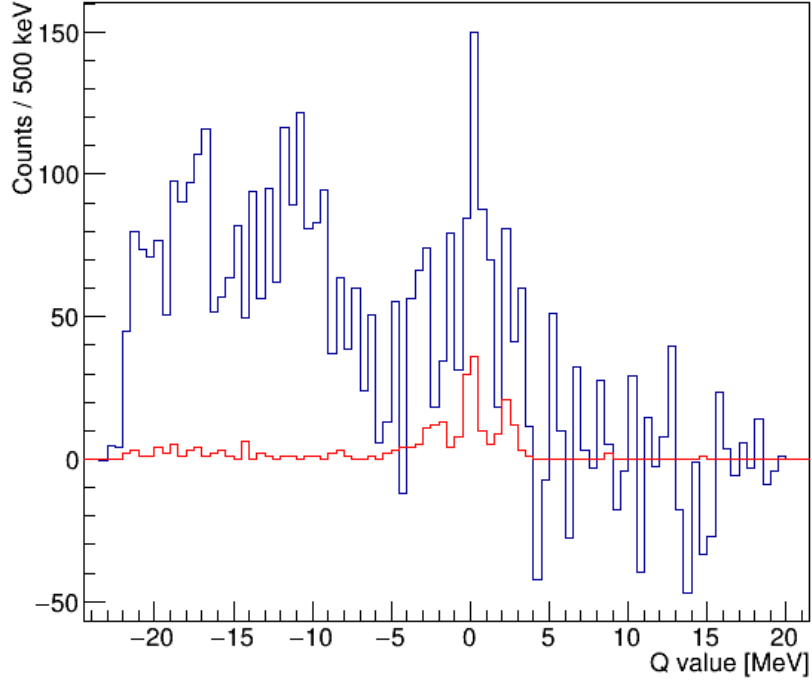


Figure 3.24: Q value spectrum in SIDAR for background subtracted particle singles (blue) and S800 coincident events (red).

### 3.1.7 Differential cross sections

The normalized cross sections were then extracted for each angular range. Figures 3.25 and 3.26 show the observed differential cross section for the  $5/2^+$  ground state and  $1/2^+$  first excited state. Due to the relatively low statistics present for the two transfer cross sections, only four angular bins were used: One each for SIDAR and the upstream ORRUBA barrel, and two bins in the downstream ORRUBA barrel. Finite-Range ADWA calculations assuming  $2d_{5/2}$  and  $3s_{1/2}$  configurations for the ground- and first-excited state, respectively, were calculated for a range of Woods-Saxon potential parameters,  $r_0$  and  $a$  to fit the observed differential cross section. The fits to the data were performed using a least squares minimization technique.

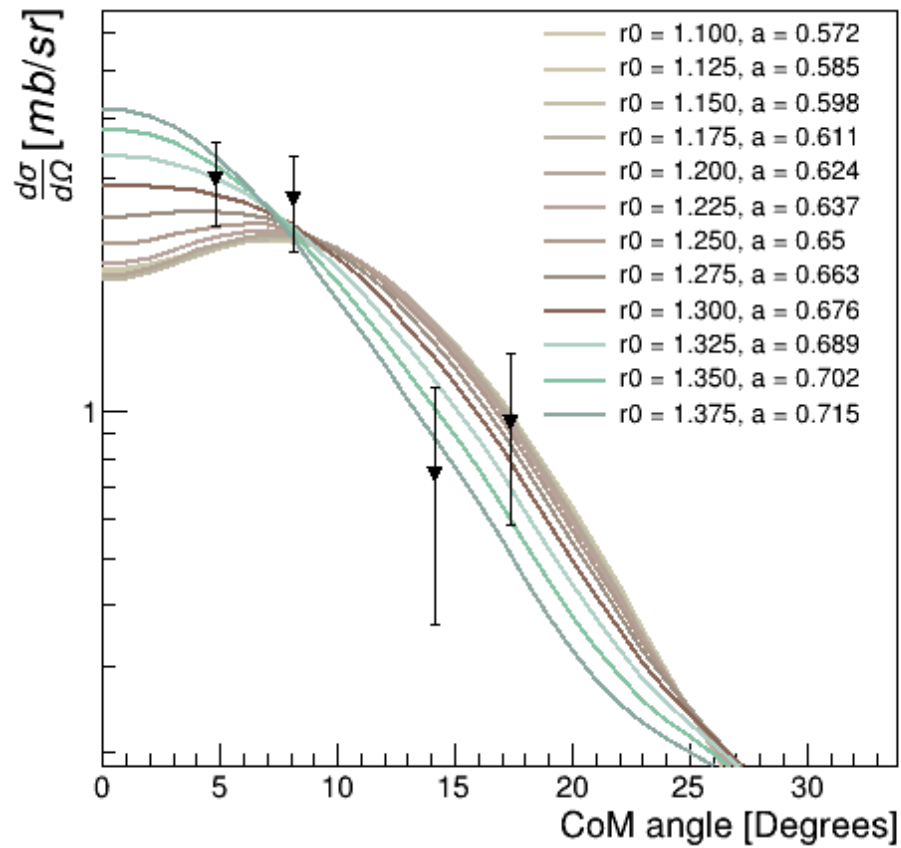


Figure 3.25: Absolute differential cross section as a function of center-of-mass angle for the  $^{84}\text{Se}(d,p)^{85}\text{Se}(\text{g.s.})$  reaction at 45 MeV/u (points) with normalized FR-ADWA calculated cross sections for a range of bound-state parameters.

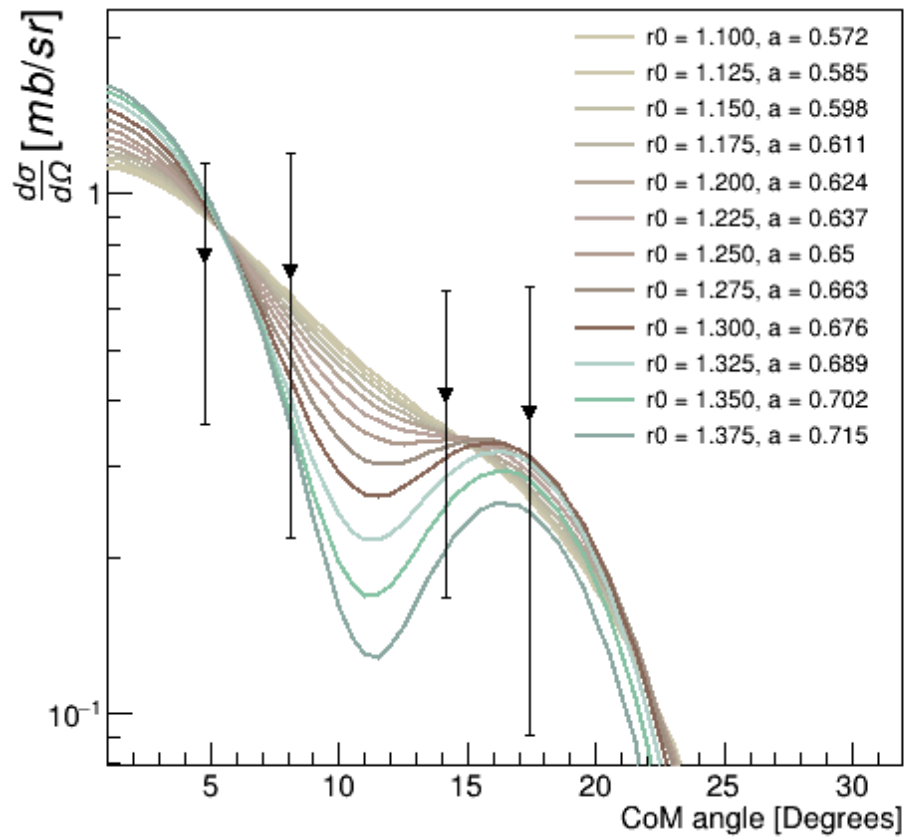


Figure 3.26: Absolute differential cross section as a function of center-of-mass angle for the  $^{84}\text{Se}(d,p)^{85}\text{Se}(\text{1st Ex} - 0.462 \text{ MeV})$  reaction at 45 MeV/u (points) with normalized FR-ADWA calculated cross sections for a range of bound-state parameters.

### 3.2 $^{84}\text{Se}(\text{d,p})^{85}\text{Se}$ at 4.5 MeV/u

The previous measurement of  $^{84}\text{Se}(\text{d,p})$  by Thomas *et al.* [Tho07] was also performed in inverse kinematics, but at 4.5 MeV/u using radioactive beams of  $^{84}\text{Se}$  produced at the Holifield Radioactive Ion Beam Facility (HRIBF) at Oak Ridge National Laboratory. The beam impinged on a  $200 \mu\text{g}/\text{cm}^2$   $\text{CD}_2$  target for 10 days, where ejected protons were detected using SIDAR and a radially-segmented S1 detector covering angles between  $105^\circ$  and  $150^\circ$ , and  $160^\circ$  and  $170^\circ$  in the laboratory frame, respectively. Recoil  $^{85}\text{Se}$  ions were detected in coincidence using an ion chamber located downstream of the target.

Angular distributions were extracted for the ground state, and the first three excited states (including a doublet at 1.44 MeV). Definitive  $J^\pi$  assignments could only be made for the ground state and the first-excited state, due to the relatively undistinctive shape of the angular distributions. Thomas *et al.* extracted the many-body ANC for the two states using the standard DWBA formalism, with standard bound-state potential parameters  $r_0=1.25$  fm,  $a=0.65$ fm. To remain consistent with, and enable comparisons to the high-energy measurement, a re-analysis of the low-energy data using FR-ADWA calculations was performed.

Experimentally observed angular distributions, overlaid with theoretical calculations for transfers to the ground state and first-excited state are shown in Figures 3.27 and 3.28. The single-particle information extracted using both the DWBA fit from Thomas *et al.*, and FR-ADWA fits are shown in Table 3.5. All calculations used to produce Table 3.5 were performed using the standard values for  $r_0$  and  $a$  (1.25 fm, 0.65 fm respectively). The DWBA ( $\chi^2/\text{DOF} = 1.90$ ) fits the data better than the FR-ADWA ( $\chi^2/\text{DOF} = 6.17$ ) fits for the ground state. However, the first excited state is better fit

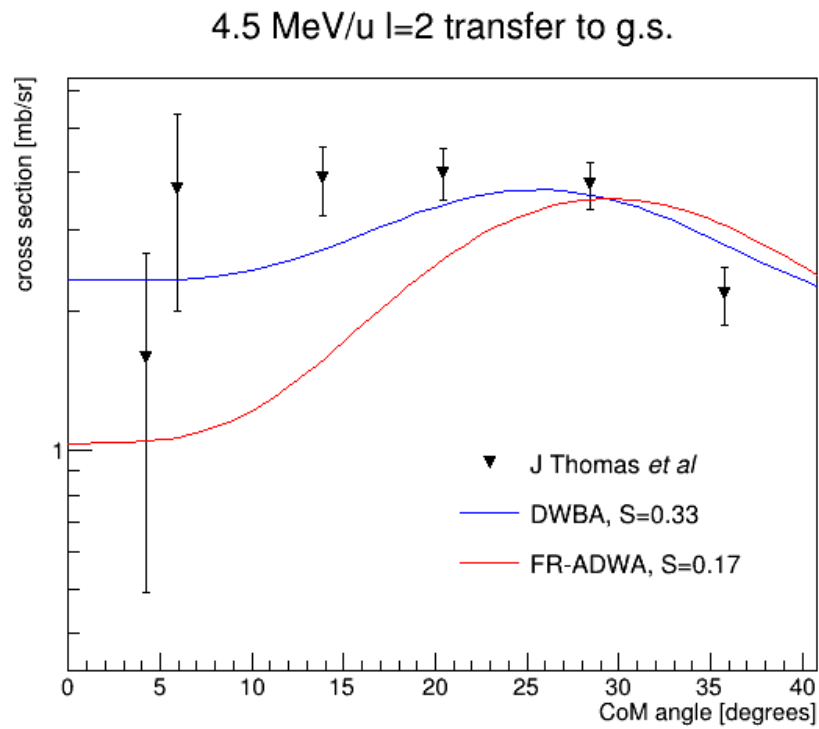


Figure 3.27: Absolute differential cross section for the  $^{85}\text{Se}$  ground state (points) with normalized FR-ADWA (red) and DWBA (blue) calculated cross sections for  $^{84}\text{Se}(d,p)$  at 4.5 MeV/u. Data taken from Ref [Tho07].  $\chi^2/\text{degree of freedom (DOF)}$  is 1.90 for the DWBA fit, and 6.17 for the ADWA fit.

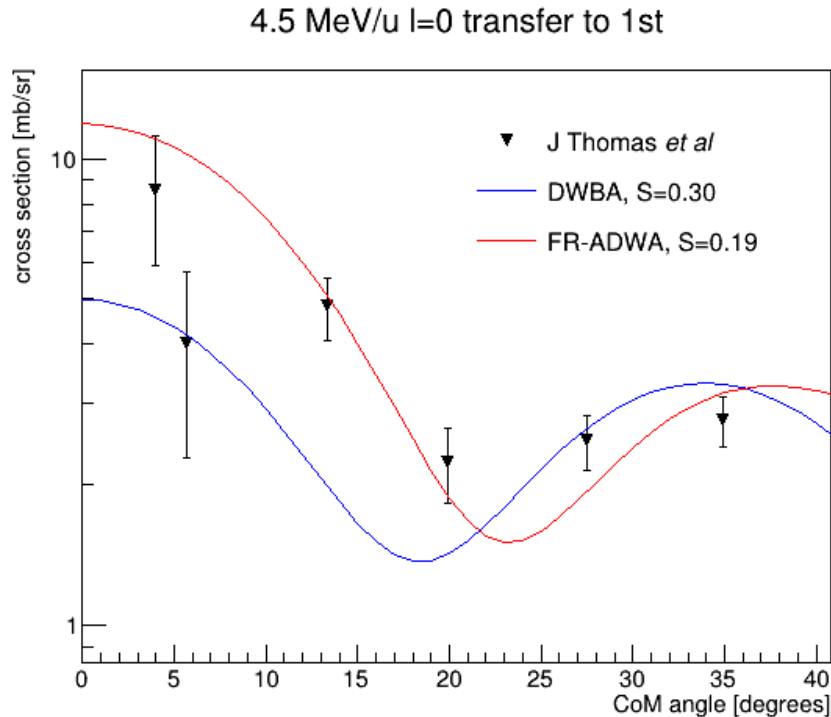


Figure 3.28: Same as Figure 3.27 but for the  $^{85}\text{Se}$  first excited state at 0.462 MeV.  $\chi^2/\text{degree of freedom (DOF)}$  is 4.60 for the DWBA fit, and 1.57 for the ADWA fit.

with the FR-ADWA ( $\chi^2/\text{DOF} = 1.57$ ) than with DWBA ( $\chi^2/\text{DOF} = 4.60$ ).

Large uncertainties on the two data points closest to zero degrees show that the shape in this region is not, however, well constrained. Data showing the energy - angle (detector strip) systematics for SIDAR and the S1 detector are shown in Figure 3.29.

Due to the low statistics, and poor separability of the states observed in the S1 detector, the extracted spectroscopic information was checked by *combining* the cross sections of the ground and first-excited state. An analysis assuming an “unresolved” doublet was performed, fitting the combined ground- and first-excited states observed cross section using some fractional combination of the FR-ADWA predicted cross sections. A minimization fit of the  $\chi^2$  was performed, to determine the contribution of

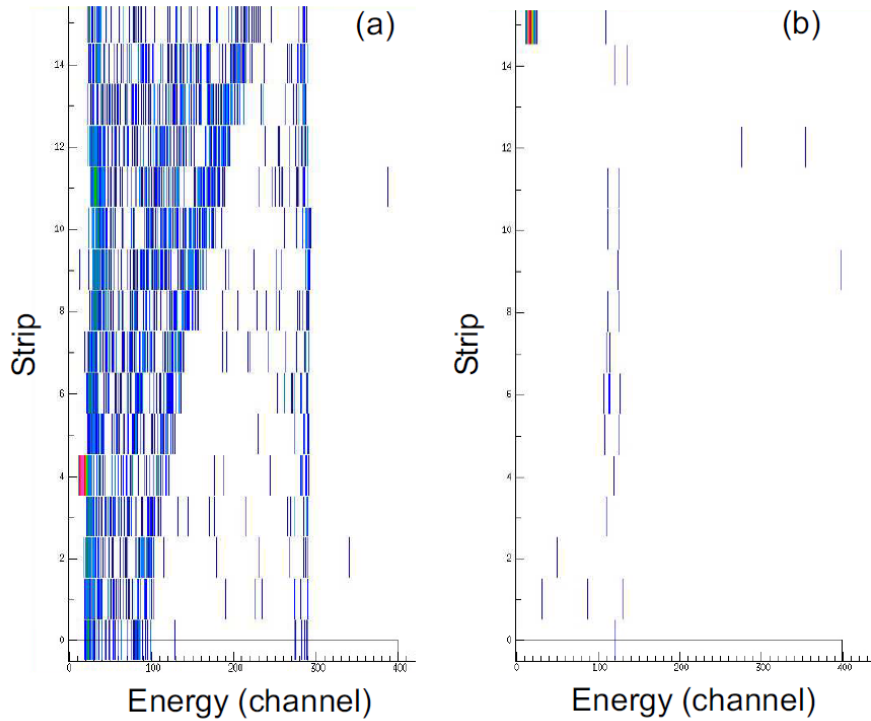


Figure 3.29: Energy - detector strip systematics for  $^{84}\text{Se}(d,p)$  at 4.5 MeV/u. Data taken from SIDAR (a) and the S1 detector (b). Figure taken from Ref [Tho07].

each state. The cross-section components from the fit are shown individually, and combined along with the observed unresolved cross section to the ground- and first-excited states in Figure 3.30. The  $\chi^2$  as a function of the ground- and first-excited state's spectroscopic factors is shown in Figure 3.31.

Tables 3.5 and 3.6 give the values extracted using the standard  $(r_0, a)$  parameters for the bound-state potential. Uncertainties were calculated to include a 15% uncertainty in the target thickness, 19% uncertainty due to ignorance of the bound state geometry, and an uncertainty of 7% for the choice in optical model. The stated uncertainty from Thomas *et al.* in the choice of optical model was 17%, as a result of the increased sensitivity in cross section to optical model choice for DWBA calculations - shown in section 2.1. The many-body ANCs extracted using FR-ADWA are lower than those

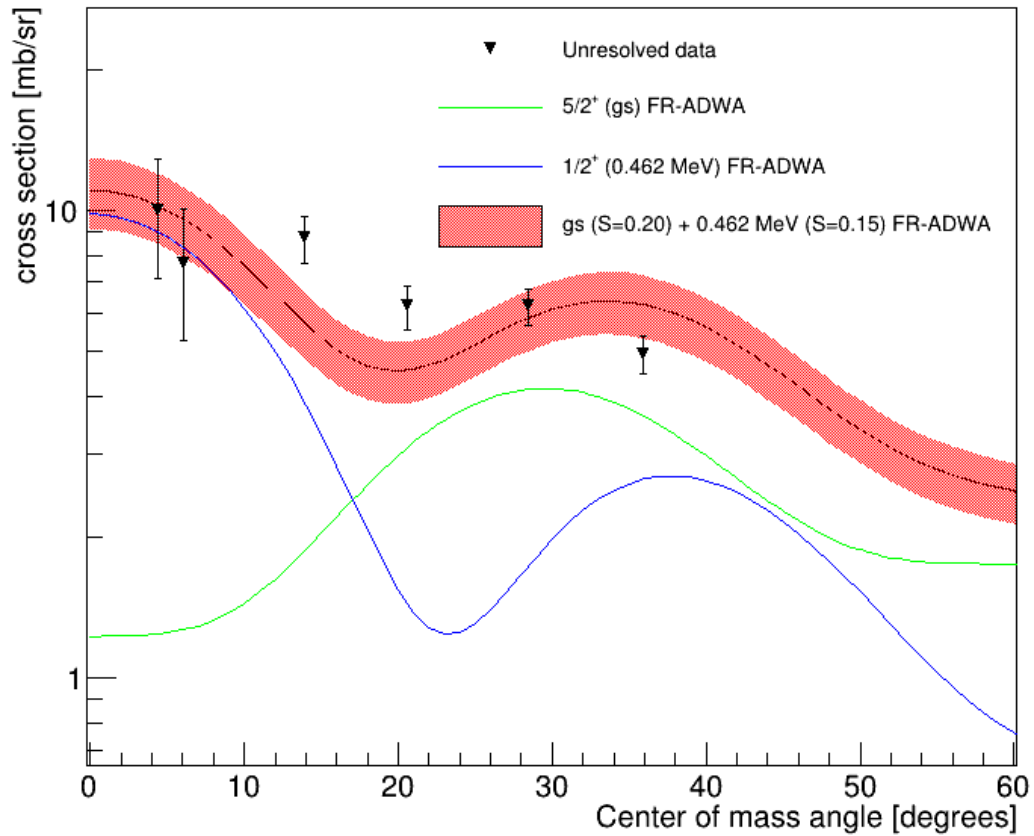


Figure 3.30:  $^{84}\text{Se}(d,p)$  at 4.5 MeV per nucleon observed differential cross section assuming unresolved ground and first excited (0.462 MeV) states (points). A  $\chi^2$  minimization of the total FR-ADWA predicted cross sections to that observed yields the spectroscopic factor for each state. The individual predicted cross sections are also included to show the relative contributions. The red band represents the uncertainty in the deduced spectroscopic factors.

Table 3.5: Extracted single particle information from the measurement at 4.5 MeV/u for the ground and first excited (0.462 MeV) states in  $^{85}\text{Se}$  using DWBA formalism, as in Ref [Tho07].

[Tho07] DWBA			
$E_x$ [MeV]	$J^\pi$	$S$	$C_{\ell_j}^2$ [ $fm^{-1}$ ]
0.0	$5/2^+$	$0.33\pm 0.10$	$6.11\pm 1.43$
0.462	$1/2^+$	$0.30\pm 0.09$	$25.3\pm 5.9$

Table 3.6: Extracted single particle information from the measurement at 4.5 MeV/u for the ground and first excited (0.462 MeV) states in  $^{85}\text{Se}$  using ADWA formalism. Individual fits to the cross sections are used, as well as a fit assuming the ground- and first-excited states are unresolved.

This work					
$E_x$ [MeV]	$J^\pi$	FR-ADWA <sup>1</sup>		Unresolved FR-ADWA <sup>2</sup>	
		$S$	$C_{\ell_j}^2$ [ $fm^{-1}$ ]	$S$	$C_{\ell_j}^2$ [ $fm^{-1}$ ]
0.0	$5/2^+$	$0.17\pm 0.04$	$3.1\pm 0.8$	$0.20\pm 0.06$	$3.8\pm 1.1$
0.462	$1/2^+$	$0.30\pm 0.09$	$25.3\pm 5.9$	$0.19\pm 0.05$	$15.3\pm 4.0$
$0.15\pm 0.05$	$12.6\pm 4.2$				

<sup>1</sup> Individual fits to the ground state and first excited states.

<sup>2</sup> From fits to the ground and first excited states, assuming an unresolved doublet.

found through DWBA formalism, concurring with the work of Schmitt *et al.*. This is a result of the ADWA formalism consistently predicting a larger cross section than DWBA, as discussed in section 2.1.

Fitting the cross section as an unresolved doublet rather than the individual cross sections maintains a good shape for the fit; however the uncertainty associated with the fit increases - as the introduction of a second fitting variable introduces degeneracies in spectroscopic factors which produce similar  $\chi^2$  values. The spectroscopic factors deduced through the fit to the unresolved data are consistent with the individually fit cross sections, within uncertainties. This indicates that both methods provide statistically-compatible fitting results.

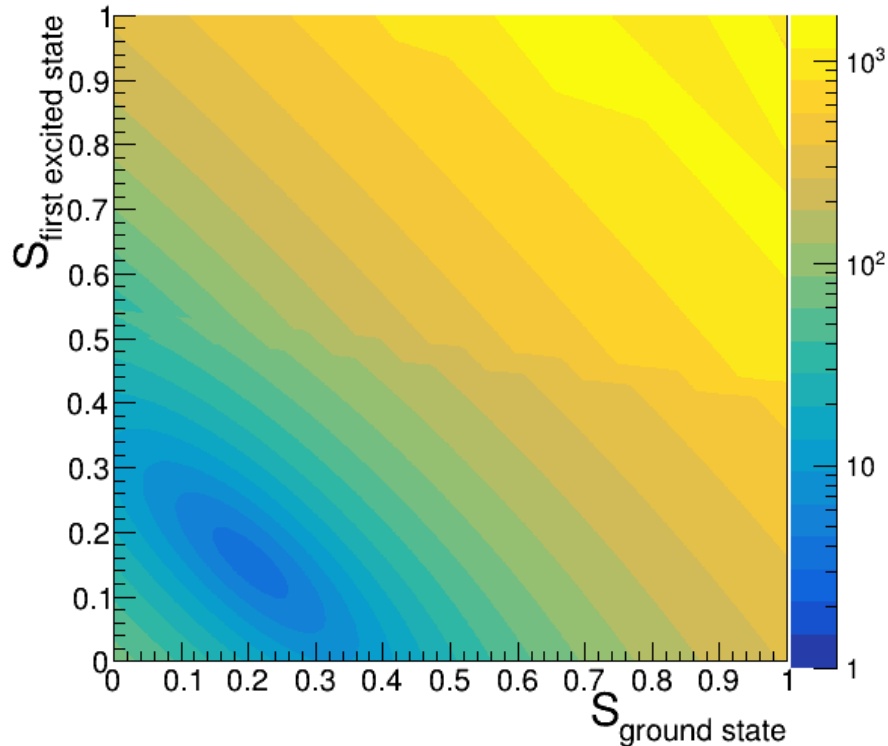


Figure 3.31:  $\chi^2/\text{D.o.F.}$  produced for each combination of spectroscopic factors when fitting the unresolved ground and first excited states.

From this point on, extracted ANCs and spectroscopic factors from the low energy measurement were calculated using individual fits to the ground and first excited (0.462 MeV) state. The fit to the unresolved data was used as a cross check throughout the spectroscopic analysis. The predicted differential cross sections for the range of  $r_0$  and  $a$  values given in Table 2.4 are shown in Figure 3.32 for both the individual fit and unresolved fit analyses.

At this low energy, the reaction probes the periphery of the wavefunction, therefore the many-body ANCs calculated from the 4.5 MeV/u data are robust and have reduced sensitivity to the choice of single-particle ANC compared to higher-energy probes. Combining the low-energy with the higher-energy, less-peripheral measurement will therefore allow for a constraint on the bound-state potential parameters to be made.

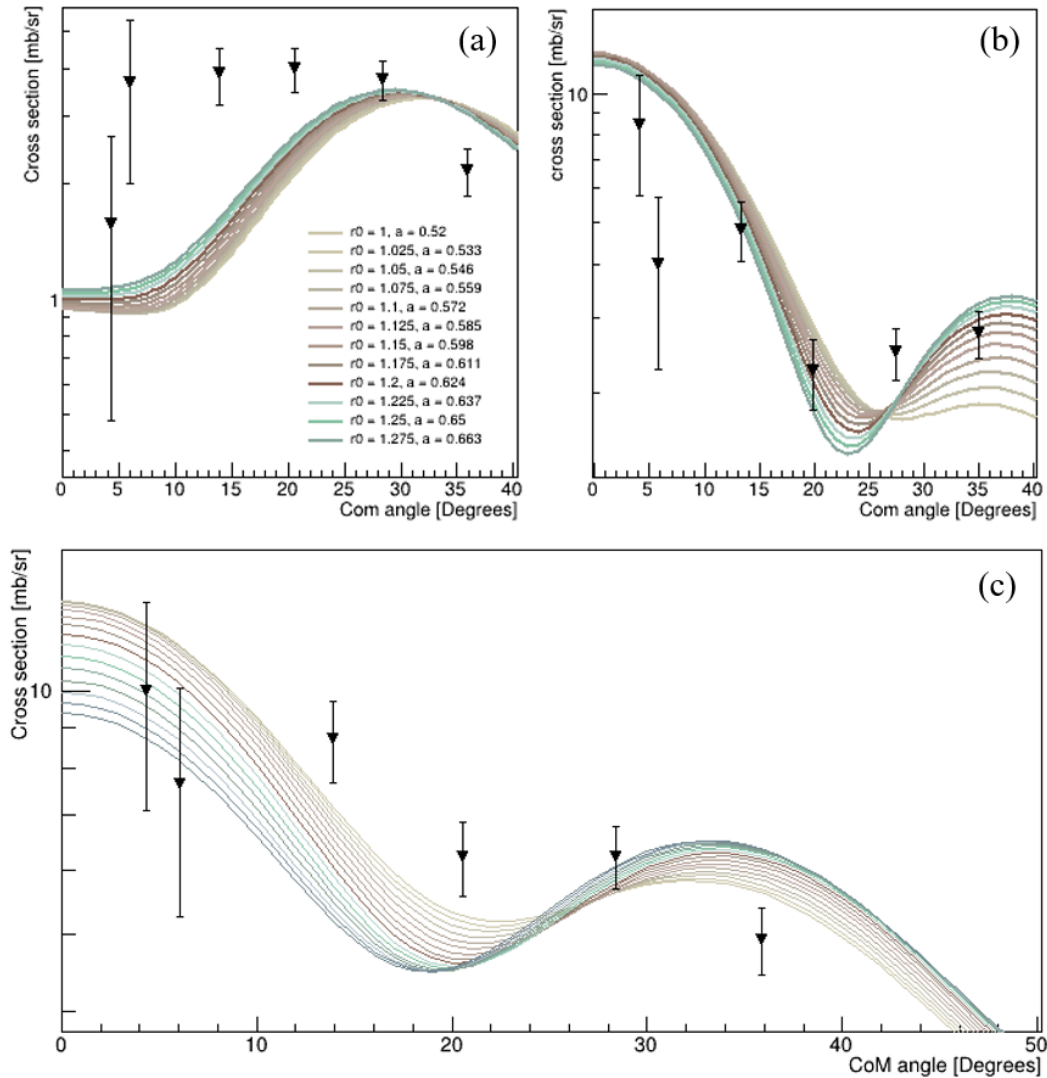


Figure 3.32: (a)  $^{84}\text{Se}(d,p)$  transfer to  $^{85}\text{Se}$  ground state at 4.5 MeV/u, with normalized FR-ADWA predicted cross sections calculated with a range of bound state geometries. (b) Same as (a), but for the  $^{85}\text{Se}$  first excited (0.462 MeV) state. (c) Transfer cross sections to the “unresolved” ground and first excited state, with two-component normalized FR-ADWA predicted cross sections overlaid. The range of  $r_0, a$  values used for each analysis is shown in the (a) legend. Data taken from Ref [Tho07].

### 3.3 Constraining the single-particle ANC, $b_{\ell j}$

To constrain the bound-state potential for the single-particle wavefunctions for the  $^{85}\text{Se}$  ground and first-excited (0.462 MeV) states, thereby reducing the uncertainties in the extracted spectroscopic factors, the *combined method* was deployed as outlined in section 2.4. Spectroscopic factors were deduced for the range of single-particle ANCs  $b_{\ell j}$  corresponding to choices of the bound-state geometry  $(r_0, a)$  listed in Table 2.4, using equation 2.1. Many-body ANCs  $C_{\ell j}$  for the  $^{85}\text{Se}$  ground state and first-excited state were deduced through equation 2.3 at both reaction energies. Deduced  $S$  and  $C_{\ell j}$  as a function of  $b_{\ell j}$  are shown in Figures 3.33 and 3.34 for the ground state and first-excited state, respectively.

For the low-energy measurement (using the resolved data) in Figures 3.33 and 3.34, the error bars are the combination in quadrature of the statistical uncertainty in the fitting to the observed differential cross section, and an uncertainty of 15% in the target thickness calculation. For the higher-energy measurement, the error bars are a combination in quadrature of the statistical fitting uncertainty, and the uncertainties in the normalization parameters, as described in Table 3.4.

As expected for the many-body ANC  $C_{\ell j}$ , the  $^{85}\text{Se}$  ground state and first-excited state remain relatively constant over different values of  $b_{\ell j}$  for the low-energy measurement, consistent with the expectations of a peripheral reaction. The higher-energy measurement probes more of the nuclear interior; therefore  $C_{\ell j}$  depends on the choice of  $(r_0, a)$ .

Many-body ANCs and spectroscopic factors are both properties of the nucleus. If the adoption of a single-particle state within the reaction model works well, it follows

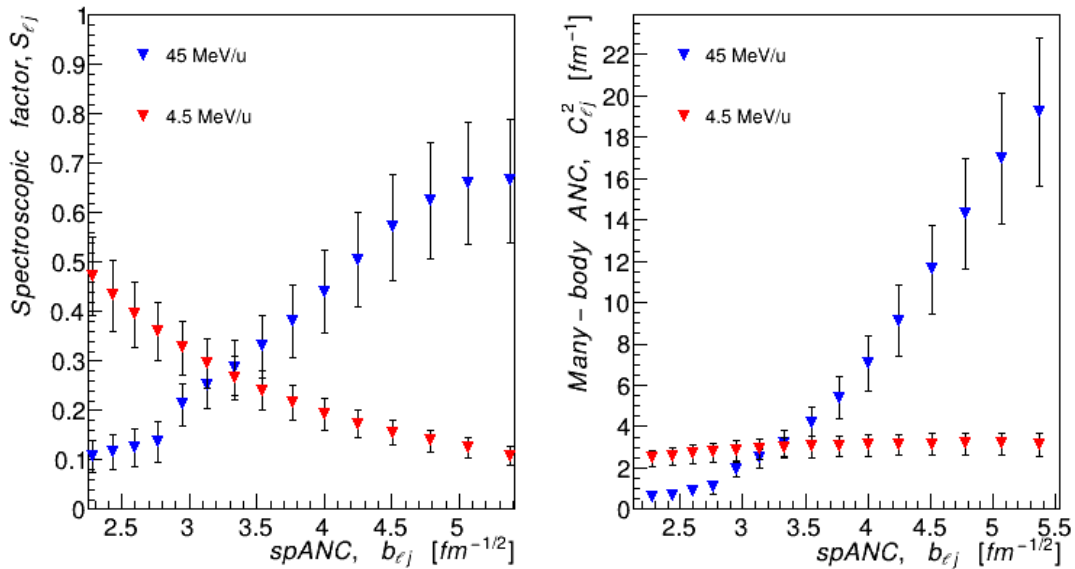


Figure 3.33: FR-ADWA analysis results for the  $^{85}\text{Se}$   $5/2^+$  ground state at 4.5 MeV/u (red) and 45 MeV/u (blue) using Koning-Delaroche optical model parameters for the theoretical calculations. (a) Spectroscopic factors as a function of single particle ANC. (b) Many body ANC as a function of single particle ANC. Error bars in the low energy measurement include the target thickness and fitting uncertainties, but not the uncertainties due to the choice in optical model. The high energy error bars are a combination in quadrature of the systematic uncertainties stated in Table 3.4, and the statistical uncertainty of the fitting analyses.

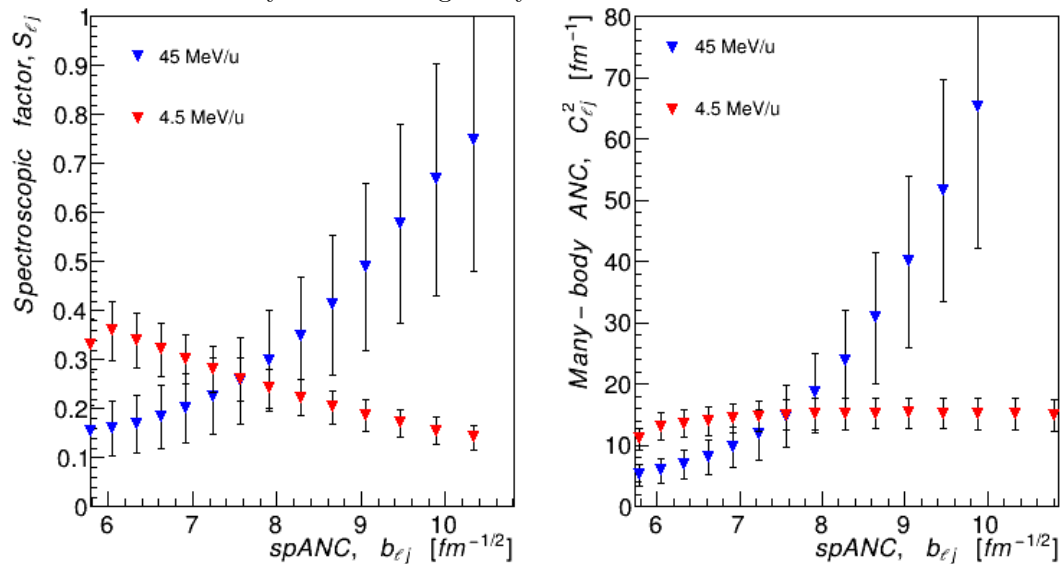


Figure 3.34: Same as Figure 3.33, but for the first excited state in  $^{85}\text{Se}$ .

that there exists a bound-state potential geometry that, when used to calculate the differential cross section, deduces a consistent value for  $C_{\ell j}$  and  $S_{\ell j}$  - regardless of the reaction energy. This corresponds to the points where the low- and high-energy measurements cross on Figures 3.33 and 3.34. This gives the extracted spectroscopic factors and many body ANCs for the ground state and first excited state shown in Table 3.7. Re-analyzing both the low- and high-energy data using Chapel Hill optical model parameters, as an alternative to Koning-Delaroche, informs the sensitivity of the extracted spectroscopic information to the chosen optical model parameters. The extracted spectroscopic information using both sets of optical model parameters is shown in Table 3.7.

It is interesting to note that the spectroscopic factors obtained here using both Koning-Delaroche and Chapel Hill OMPs are compatible with the results from the DWBA analysis using standard bound-state potential parameters from Reference [Tho07]. This is because the FR-ADWA analysis reduces the spectroscopic factors as a function of single-particle ANC, and the non-standard crossing point between the high- and low-energy reactions actually increases the extracted spectroscopic factor. These two effects are working against each other in this instance, leaving the extracted spectroscopic factor similar to that found in Reference [Tho07].

To better understand uncertainties due to the above analysis methods, spectroscopic factors are also extracted via two additional analysis methods: a DWBA interpretation of the theoretical cross sections, and an ADWA analysis treating the ground- and first-excited states as unresolved for the low-energy measurement (as discussed in section 3.2). Radius and diffuseness parameters were once again varied within the range given in Table 2.4. This will check the reaction formalisms, and fitting analyses for consistency.

Table 3.7: Extracted spectroscopic factors  $S$  and many body ANCs  $C_{\ell j}$  calculated using the constrained single-particle ANC  $b_{\ell j}$  for the  $^{85}\text{Se}$  ground state and first excited (0.462 MeV) state, using both Koning-Delaroche and Chapel Hill optical model parameters. No optical model or bound-state geometry uncertainties are included.

Koning-Delaroche				
$E_x$ [MeV]	$J^\pi$	$b_{\ell j}$ [ $fm^{-1/2}$ ]	$C_{\ell j}^2$ [ $fm^{-1}$ ]	$S$
0.0	$5/2^+$	$3.28 \pm 0.30$	$2.97 \pm 0.50$	$0.28 \pm 0.04$
0.462	$1/2^+$	$7.57 \pm 0.81$	$15.0 \pm 3.4$	$0.26 \pm 0.06$
Chapel Hill				
$E_x$ [MeV]	$J^\pi$	$b_{\ell j}$ [ $fm^{-1/2}$ ]	$C_{\ell j}^2$ [ $fm^{-1}$ ]	$S$
0.0	$5/2^+$	$3.40 \pm 0.31$	$3.56 \pm 0.48$	$0.31 \pm 0.05$
0.462	$1/2^+$	$7.56 \pm 0.81$	$16.7 \pm 4.3$	$0.29 \pm 0.06$

For the DWBA analysis, a zero-range approximation with Daehnick [Dae80] optical model parameters was chosen for the entrance channel, and both Koning-Delaroche and Chapel Hill optical model parameters for the exit channel. Note that the DWBA analysis of the first excited state using Koning-Delaroche optical model parameters yielded no crossing point between the high- and low-energy measurements within the range of  $(r_0, a)$  listed in Table 2.4 - such that no single-particle ANC could be constrained. Figure 3.28 shows the DWBA predicted cross section for the first-excited state assuming canonical values for the radius and diffuseness. The peak at zero degrees for this  $\ell=0$  transfer should be the most reliable part of the predicted angular distribution. Clearly the DWBA calculation is under-predicting the first peak, resulting in smaller spectroscopic factors. This pushes the crossing point of the low- and high-energy data to unphysical values for the single-particle ANC. Deduced spectroscopic factors are displayed in Figures 3.35 and 3.36.

Sensitivities to the choice in optical model were determined from the FR-ADWA analysis in Figures 3.35 and 3.36 where results from Koning-Delaroche and Chapel Hill OMPs are compared. The extracted spectroscopic factors summarized in Table 3.8 come from the FR-ADWA analysis with Koning-Delaroche OMPs and using the resolved

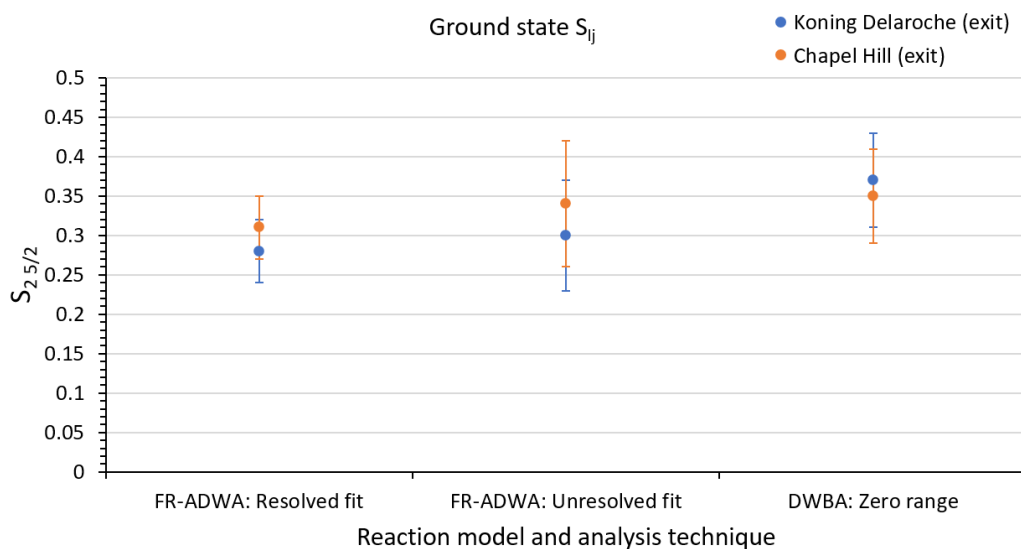


Figure 3.35: Comparison of deduced spectroscopic factors, using FR-ADWA calculated cross sections with the resolved low energy data, FR-ADWA fits treating the low energy data as unresolved, and DWBA fits to the individual cross sections for both the low- and high-energy data. These were calculated using both Koning-Delaroche (blue), and Chapel Hill (orange) optical model parameters.

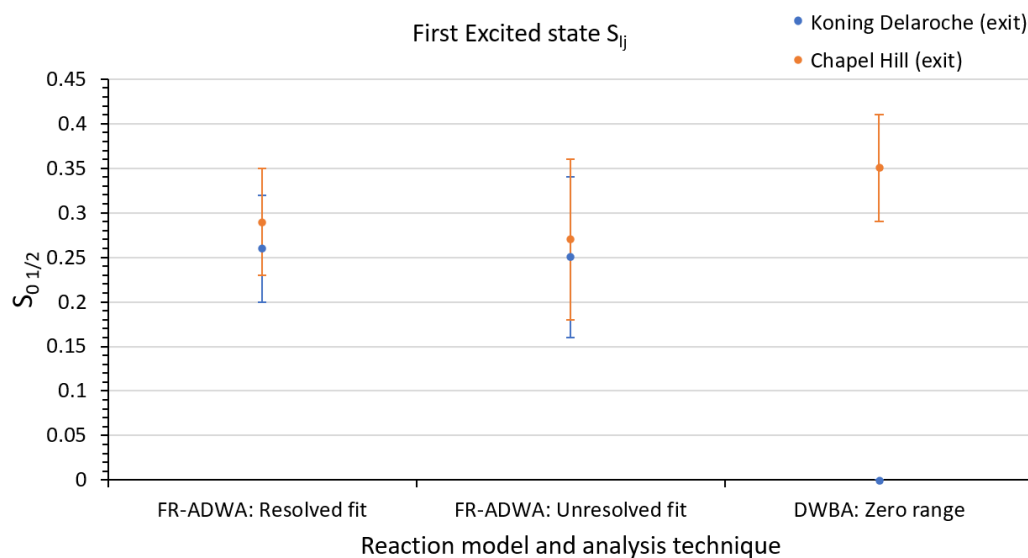


Figure 3.36: Same as Figure 3.35, but for the first excited (0.462 MeV) state in  $^{85}\text{Se}$ .

4.5 MeV/u data. The uncertainties in the spectroscopic factors include uncertainties from the choice in OMP in the FR-ADWA analysis, as well as uncertainties in deducing the crossing in Fig. 3.30 and 3.31 to constrain the single-particle ANC.

Table 3.8: Final deduced spectroscopic factors for the ground- and first-excited states in  $^{85}\text{Se}$ . FR-ADWA calculations were used for both the high- and low-energy data, and the resolved ground- and first-excited states were analyzed for low energy data. Koning-Delaroché optical model parameters are used. Uncertainties include the uncertainty in optical model (calculated using Figures 3.35 and 3.36).

Ex [MeV]	$J^\pi$	$S_{\ell j}$
0.0	$5/2^+$	$0.28 \pm 0.05$
0.462	$1/2^+$	$0.26 \pm 0.07$

### 3.3.1 Expanding the parameter space in $(r_0, a)$

The constrained single-particle ANC was deduced within the set of  $(r_0, a)$  listed in Table 2.4. However, the radius and diffuseness parameters are not individually constrained, due to the degeneracy in  $(r_0, a)$  pairs that produce the same values of  $b_{\ell j}$ .

To demonstrate this, the many-body ANCs and spectroscopic factors were calculated for a 2D parameter space in  $r_0$  and  $a$ . Figures 3.37 and 3.38 show the spectroscopic factors and many-body ANCs as a function of both  $r_0$  and  $a$ . The original sets of parameters used in Table 2.4 and Figures 3.33 and 3.34, where  $r_0$  and  $a$  are scaled proportionally together, are given by the red triangles overlaid on the surfaces. The range of  $(r_0, a)$  parameters that exist in the crossing region between the high- and low-energy surfaces, shown as the red line, highlights the  $(r_0, a)$  parameters that all produce a consistent spectroscopic factor for both the high- and low-energy reaction - satisfying the criteria for the constrained bound-state potential geometry. For both states, an increased sensitivity can be seen in the single-particle ANC to the radius parameter, rather than the diffuseness. This is apparent from the steeper gradient observed in the

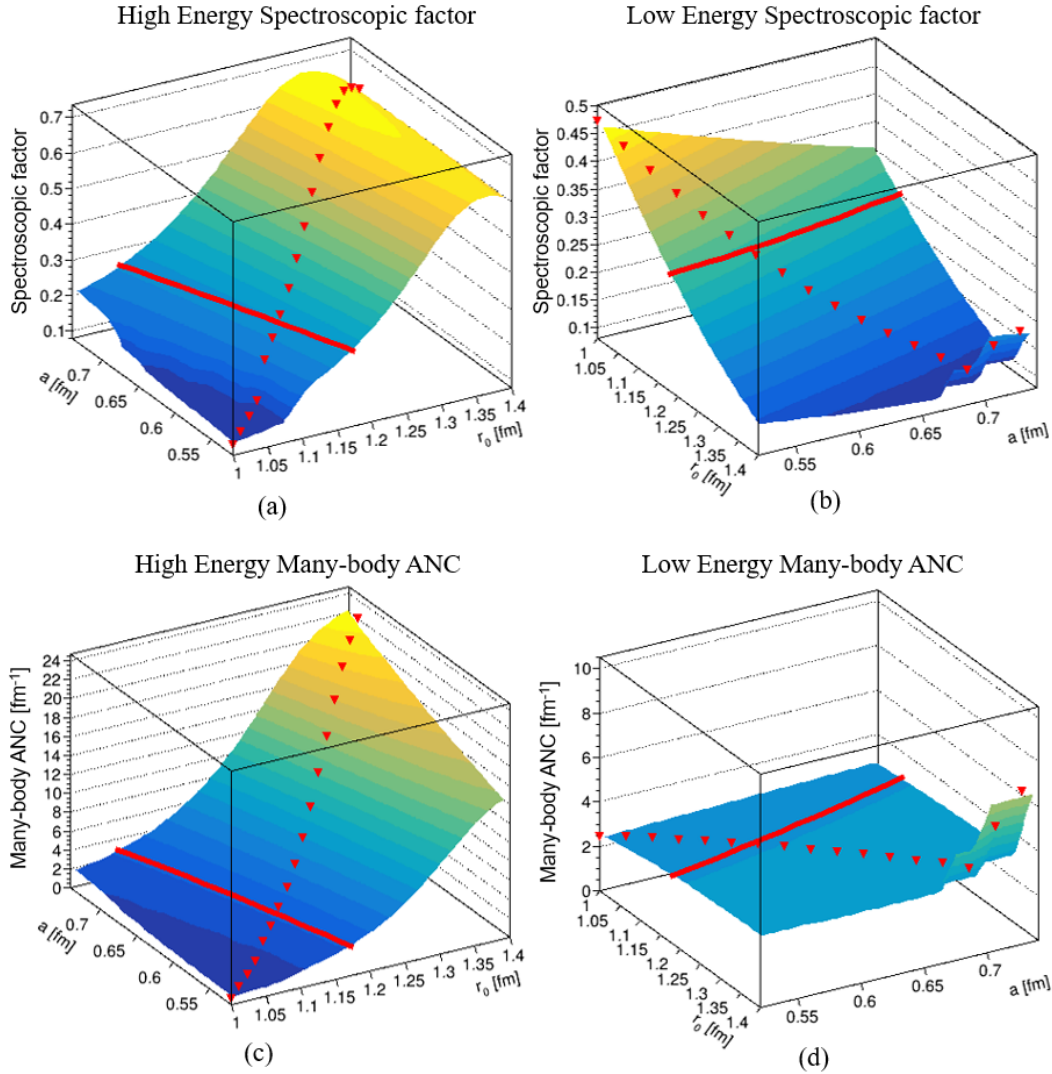


Figure 3.37: Spectroscopic factor  $S_{\ell j}$ , and ANC  $C_{\ell j}^2$  surfaces as a function of both bound state radius  $r_0$  and diffuseness  $a$  parameters for the  $^{84}\text{Se}(d,p)^{85}\text{Se}$  ground state ( $5/2^+$ ) reaction. (a) and (b) Spectroscopic factors for the high and low energy reaction respectively. (c) and (d) Many-body ANC for the high and low energy reaction respectively. Where the surfaces of the high- and low-energy reactions cross is given by a red line. The points from the proportionally varying  $(r_0, a)$  parameters (shown in Table 2.4, and used to calculate the crossing values in Figure 3.33) are denoted as red triangles.

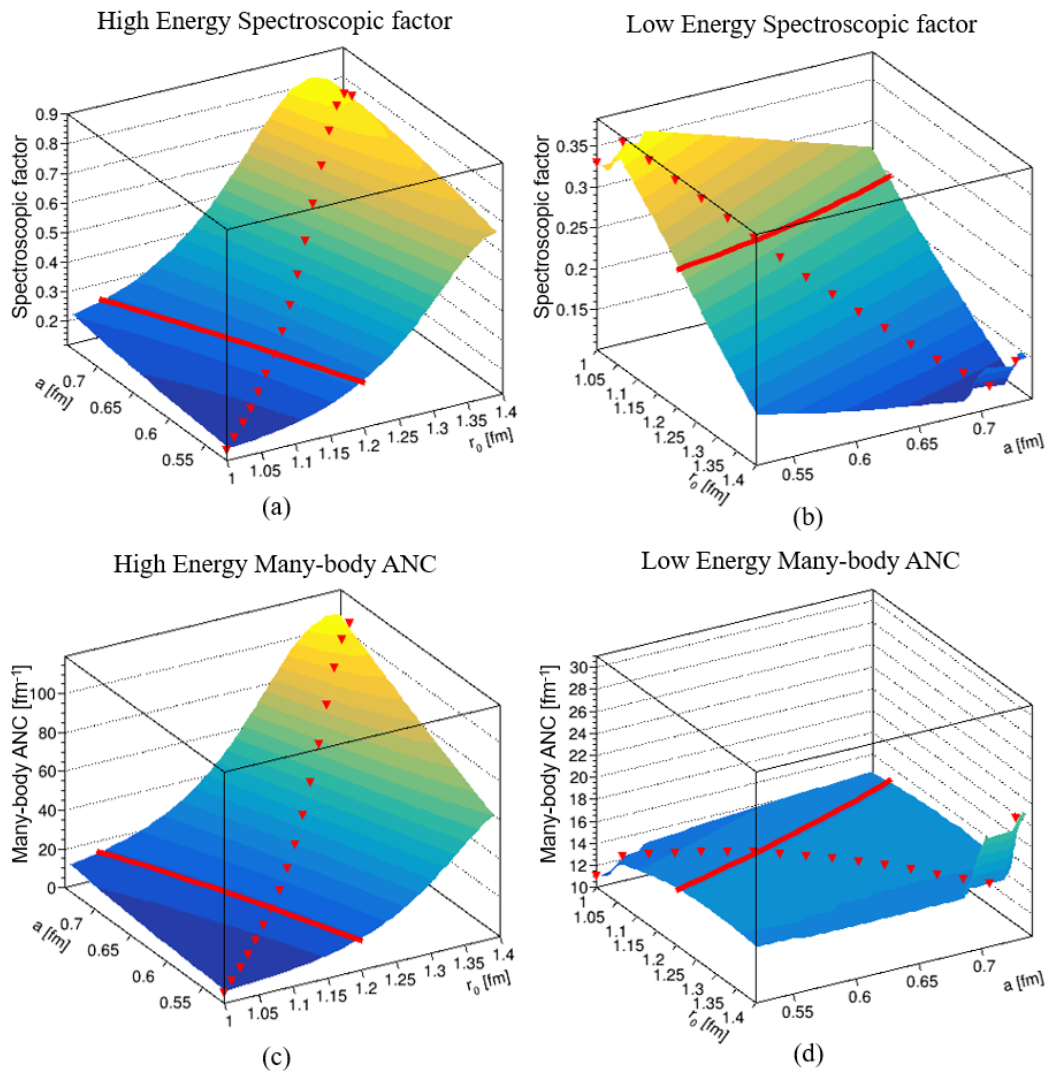


Figure 3.38: Same as Figure 3.37, but for the  $^{85}\text{Se}$  first excited state (0.462 MeV).

$r_0$  axis compared to the  $a$  axis. A change in the radius parameter for the bound-state potential has a much larger effect on the tail of the wave function than the diffuseness does, directly affecting the single-particle ANC.

The constrained region of  $(r_0, a)$  is also shown in Figures 3.39 and 3.40, where the single-particle ANC is given as a function of the radius parameter  $r_0$ , overlaid with lines of constant diffuseness  $a$ . Both the constrained surface of  $(r_0, a)$  values, and the value from the combined method with proportionally varying  $(r_0, a)$  parameters are included. These figures highlight the constrained value for the single-particle ANC for the ground and first-excited states, respectively. The combined method using proportionally varying  $(r_0, a)$  parameters in Figures 3.33 and 3.34 is demonstrated to be sufficient to constrain the single-particle ANC, as the values deduced from the constrained surface of the  $(r_0, a)$  space (shown in Figures 3.37 and 3.38) lie within the uncertainty of the single-particle ANC value deduced using the proportionally varying  $(r_0, a)$  parameters.

The same result is also shown in the parameter space  $b_{\ell j}(r_0, a)$ , to show more directly the values of  $r_0$  and  $a$  that produce a consistent spectroscopic factor at both reaction energies. Figures 3.41 and 3.42 show the single-particle ANC as a function of  $r_0$  and  $a$  for the ground and first-excited state. The combined-method point using proportional values and constrained surfaces analyses are also shown.

Table 3.9: Deduced radius and diffuseness of the ground- and first-excited (0.462 MeV) state in  $^{85}\text{Se}$  from the combined method using proportionally varying parameters.

Ex [MeV]	$J^\pi$	$b_{\ell j}$ [ $\text{fm}^{-1/2}$ ]	$r_0$ [fm]	$a$ [fm]
0.0	$5/2^+$	$3.28 \pm 0.30$	$1.14^{+.04}_{-.06}$	$0.59^{+.02}_{-.03}$
0.462	$1/2^+$	$7.57 \pm 0.81$	$1.16^{+.06}_{-.09}$	$0.60^{+.04}_{-.04}$

The radius and diffuseness deduced from the combined method, as shown in Table 3.9, are lower than the canonical values,  $r_0 = 1.25$  fm and  $a = 0.65$  fm. This

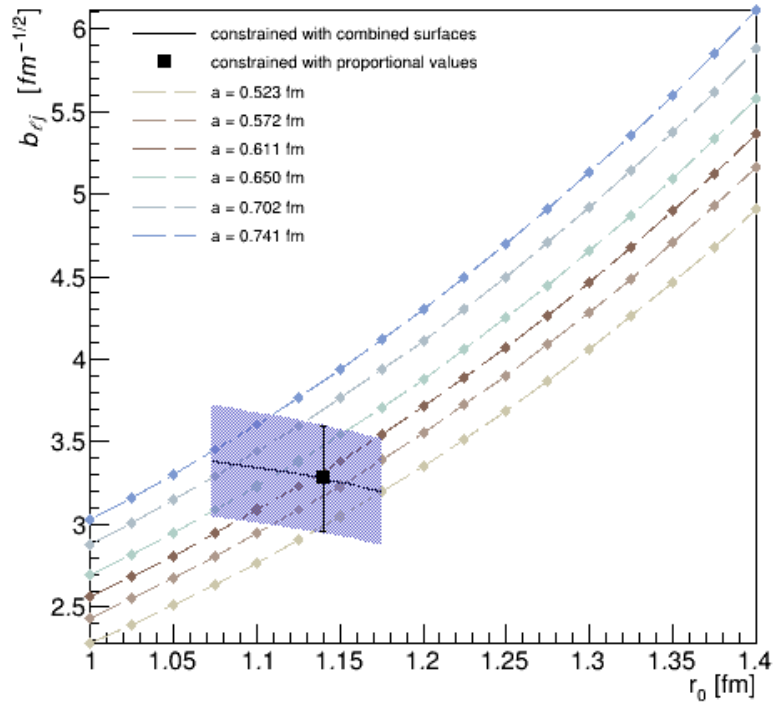


Figure 3.39: Single-particle ANC  $b_{\ell j}$  for the  $5/2^+$  ground state as a function of bound state radius parameter  $r_0$ . Lines of constant diffuseness are overlaid. The shaded region is the constrained  $(r_0, a)$  surface crossing deduced in Figure 3.37, and the black square is the crossing value that is constrained using proportionally varying  $(r_0, a)$  parameters, as in Figure 3.33. The uncertainty in the “proportional value” point corresponds to the uncertainty calculated for the constrained  $b_{\ell j}$ .

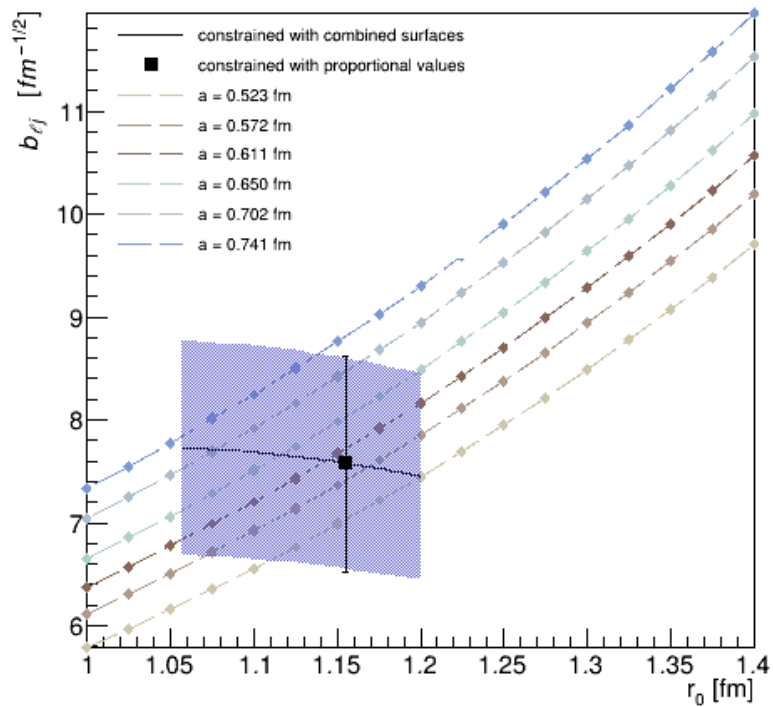


Figure 3.40: Same as Figure 3.39, but for the  $^{85}\text{Se}$  first excited state (0.462 MeV).

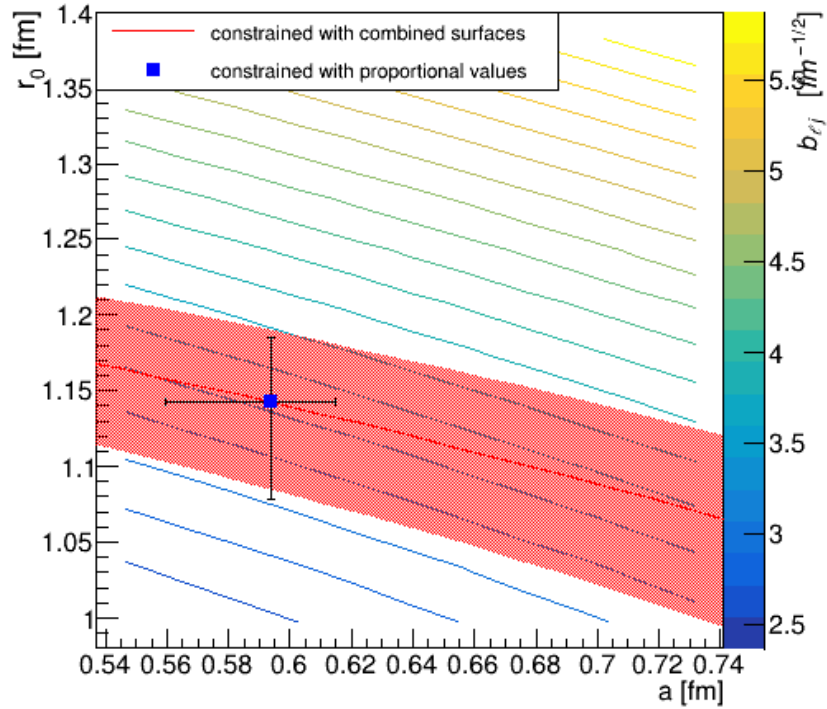


Figure 3.41: Single-particle ANC  $b_{\ell j}$  for the  $5/2^+$  ground state (color scale) as a function of bound state radius  $r_0$  and diffuseness  $a$  parameters. The constrained surface between the high and low energy measurements is shown, as well as the  $(r_0, a)$  of the extracted spectroscopic factor using the combined method. The uncertainty in the “proportional value” point corresponds to the uncertainty calculated for the constrained  $b_{\ell j}$ .

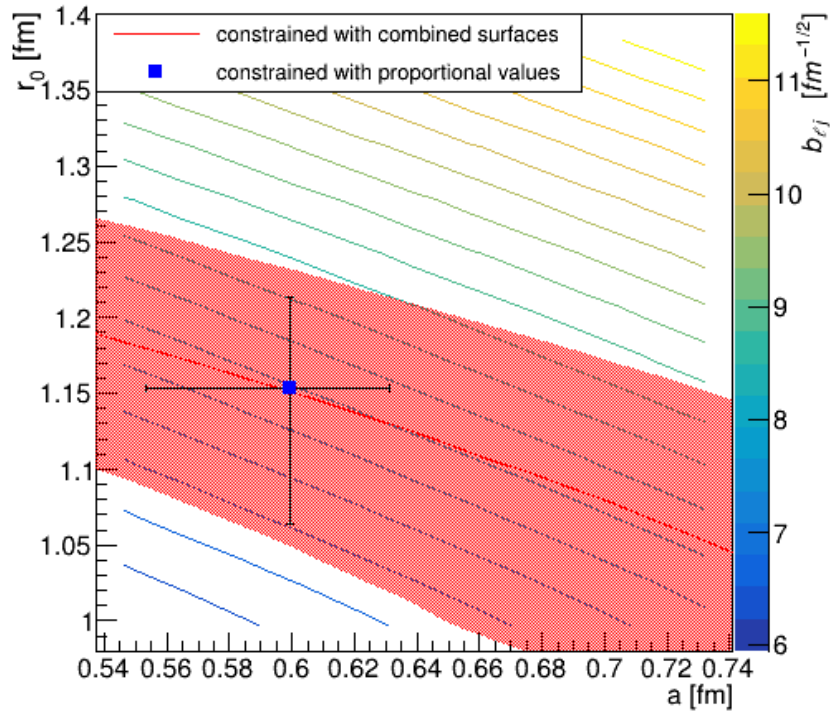


Figure 3.42: Same as Figure 3.41, but for the first excited state.

demonstrates the necessity of the combined method for nuclei where the bound state geometry is unknown, particularly away from stability. Due to the higher sensitivity of  $b_{\ell j}$  to  $r_0$ , it can be appropriate to discuss only the radius when considering the degree of deviation from canon, rather than the diffuseness. Indeed, some studies *only* vary the radius when considering the uncertainty due to ignorance of the bound state potential, eg Ref [Jon11]. The ground and first excited state radii are within 9% and 7% of the standard value, respectively. This is a larger deviation than the  $1\sigma$  uncertainties placed on the values. The extracted spectroscopic factors using the various analysis methods discussed in this chapter are summarized in Table 3.10.

Table 3.10: Extracted spectroscopic factors for the  $5/2^+$  ground state and  $1/2^+$  first-excited state at 0.462 MeV using various analyses. Spectroscopic factors deduced through the combined method, and individually for the 4.5 and 45 MeV/u reactions (using standard bound-state potential parameters) are shown. Both DWBA and ADWA formalisms are used.

$J^\pi$	$S_{\ell j}$ Combined method		$S_{\ell j}$ 4.5 MeV/u		$S_{\ell j}$ 45 MeV/u	
	DWBA	ADWA	DWBA	ADWA	DWBA	ADWA
$5/2^+$	$0.37 \pm 0.06$	$0.28 \pm 0.04$	$0.33 \pm 0.05$	$0.17 \pm 0.03$	$0.56 \pm 0.11$	$0.51 \pm 0.10$
$1/2^+$	N/A	$0.26 \pm 0.06$	$0.30 \pm 0.05$	$0.18 \pm 0.03$	$0.40 \pm 0.15$	$0.49 \pm 0.17$

### 3.4 Direct neutron capture calculations

Spectroscopic factors influence the neutron-capture rate of r-process nuclei, affecting final abundance patterns. Astrophysical reaction rates can therefore be calculated using the newly deduced spectroscopic factors. The spins and parities of the first two states in  $^{85}\text{Se}$  implies that the neutron direct capture component proceeds via  $s$ - and  $d$ -wave capture with a magnetic dipole ( $M1$ ) transition, or  $p$ -wave capture with an electric dipole ( $E1$ ) transition. In addition to direct capture, reactions can proceed via the giant dipole resonance (GDR) during *semi-direct* neutron capture. The  $^{84}\text{Se}(n,\gamma)$  cross

section was calculated using the direct-semi direct (DSD) model with the program CUPIDO [Par95]. Optical model potentials used were those of Koning-Delaroche (to remain consistent with the (d,p) measurement), with GDR parameters taken from RIPL [Bel03].

Reaction rates were calculated using the proportionally constrained values of  $r_0$  and  $a$  deduced in this work (shown in Table 3.9), as well as the canonical values for comparison, as shown in Figure 3.43. The smaller constrained radius and diffuseness parameters reduce the DSD cross section.

The sum of the DSD  $^{84}\text{Se}(n,\gamma)$  cross section to the ground- and first excited (0.462 MeV) states is also displayed, with the semi-direct component turned on/off. The semi-direct component of neutron capture interferes destructively with the direct capture on  $^{84}\text{Se}$ , reducing the total cross section by  $\sim 10\%$ .

Neutron-capture cross sections to the ground- and first-excited states were also calculated by Thomas *et al.* [Tho07], using the spectroscopic factors deduced from the 4.5 MeV/u measurement analyzed with canonical values of  $r_0$  and  $a$ . Only the real part of the Koning-Delaroche global optical potential was used as the scattering potential. In this work, the imaginary component of the potential is also included. These differences amount to a 74% difference in the peak of the DSD cross sections between Reference [Tho07] and this work. The difference in the parameterization of the bound-state potentials accounts for 33% of this difference (as shown in Figures 3.43(a) and 3.43(b)), and the lower spectroscopic factors deduced in this work reduce the DSD cross sections by 23%. The use of a complex scattering potential instead of purely real accounts for  $\sim 42\%$  of the difference.

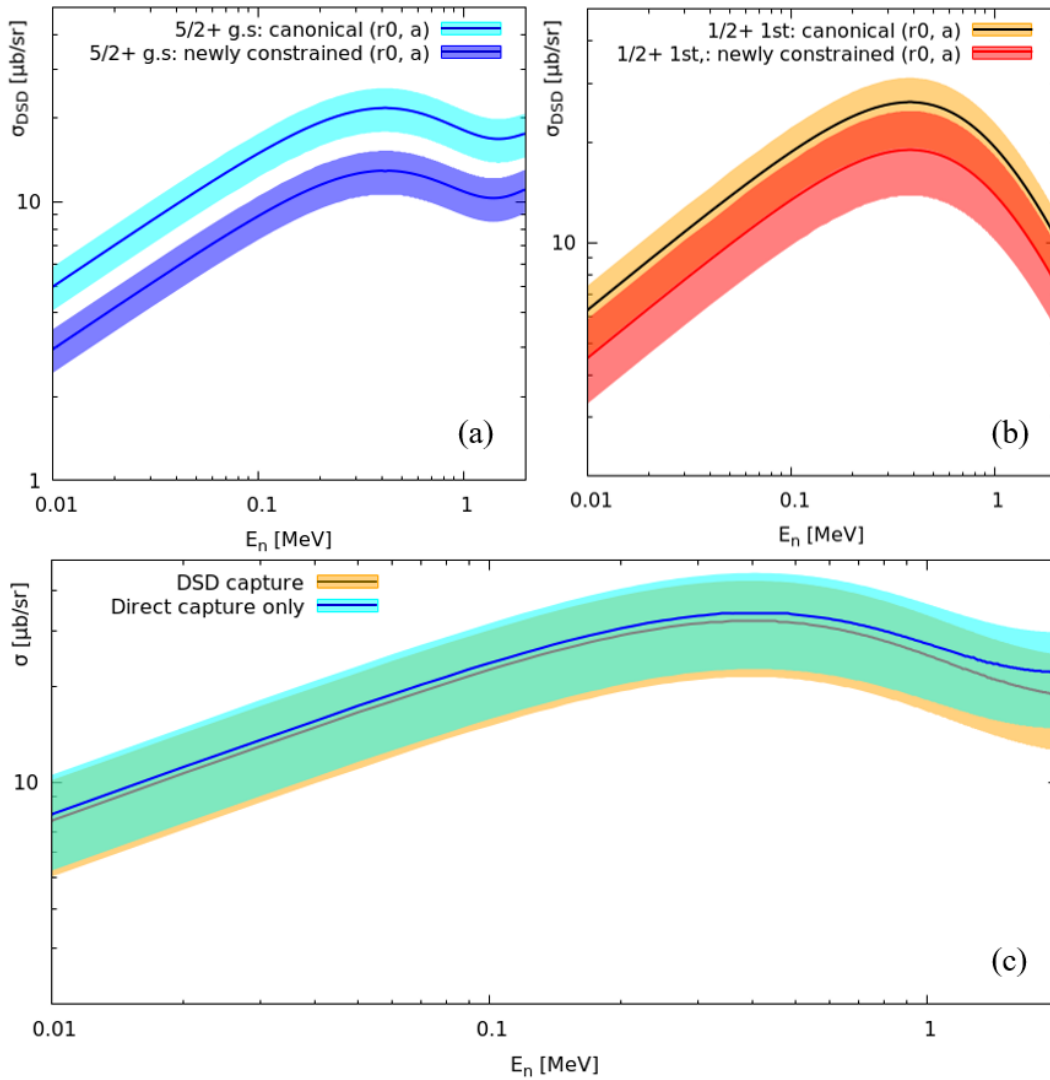


Figure 3.43: (a) Individual DSD reaction rates for  $^{84}\text{Se}(n,\gamma)$  to the  $5/2^+$  ground state, using both the canonical (light blue) and newly constrained (dark blue) ( $r_0, a$ ) parameters (as seen in Table 3.9) for the bound-state potential. (b) The same as (a), but for the  $1/2^+$  first excited (0.426 MeV) state - orange is canonical, and red is newly constrained ( $r_0, a$ ) parameters. (c) Sum of  $^{84}\text{Se}$  neutron capture cross sections to the ground- and first excited-states for direct-semi direct capture (orange), and direct capture only (cyan) using the newly constrained values for ( $r_0, a$ ). All uncertainties represent the uncertainty in the deduced spectroscopic factors.

### 3.5 Summary

The  $^{84}\text{Se}(d,p)^{85}\text{Se}$  reaction was measured at the National Superconducting Cyclotron Laboratory at 45 MeV/u in inverse kinematics. ORRUBA was used together with the S800 magnetic spectrograph to detect reaction protons in coincident with the  $^{85}\text{Se}$  recoil. This measurement was analyzed with a previous measurement at 4.5 MeV/u by Thomas *et al.* within the finite-range ADWA formalism, to constrain the bound-state geometry of the ground- and first-excited (0.462 MeV) states in  $^{85}\text{Se}$ .

Significant challenges were faced in the NSCL experiment. Firstly, a lack of recoil-coincident statistics due to an initially conservative placement of the S800 beam blocker. As a result of this, only four angular bins could be used - reducing the ability to constrain the shape of the differential cross section.

The production and separation of radioactive  $^{84}\text{Se}$  has some dispersion in the beam momentum, along with angular and positional dispersion at the target position. The largely angle-dependent kinematics encountered in high-energy inverse-kinematic measurements causes any uncertainty in the proton scattering angle to translate directly into an uncertainty in the center of mass energy. With the beam spot estimated to be approximately 6mm in diameter, beam tracking would have significantly improved our ability to separate excited states.

Absolute differential cross sections were extracted for the  $5/2^+$  ground state and the  $1/2^+$  first-excited state. The general shapes of the angular distributions matched the angular momentum transfers to the predicted single-particle states of  $2d_{5/2}$  and  $3s_{1/2}$ , consistent with the  $J^\pi$  assignments of  $5/2^+$  and  $1/2^+$ . Spectroscopic factors were extracted for a range of single-particle ANCs, by varying the bound-state potential

radius and diffuseness parameters used in a set of FR-ADWA calculations. Comparing the spectroscopic factor and many-body ANC from this 45 MeV/u measurement to that of the same reaction at 4.5 MeV/u constrained the single-particle ANCs, producing spectroscopic factors with reduced uncertainties. These were deduced to be  $0.24 \pm 0.05$  and  $0.27 \pm 0.07$  for the ground- and first-excited states, respectively.

To inform the weak r-process nucleosynthesis, direct-semi direct (DSD) neutron capture calculations were performed with CUPIDO using the proportionally constrained values for the bound-state potentials radius and diffuseness. Of course, though DSD neutron capture is expected to dominate in this nearly-closed-shell nucleus, it is still important to consider statistical  $(n,\gamma)$  capture via a compound nucleus. Work to constrain compound neutron capture in neutron-rich nuclei using ORRUBA has used gamma-ray spectroscopy in coincidence with charged-particle spectroscopy, to deduce  $(n,\gamma)$  cross sections via a surrogate reaction:  $(d,p\gamma)$ . These coincident measurements (eg,  $^{95}\text{Mo}(d,p\gamma)^{96}\text{Mo}$  and  $^{134}\text{Xe}(d,p\gamma)^{135}\text{Xe}$ ) have been performed using the Gammasphere/GRETINA - ORRUBA Dual Detectors for Experimental Structure Studies (GODDESS).

## Chapter 4

### $^{80}\text{Ge}(\text{d,p})^{81}\text{Ge}$ and preparation for Day-1 FRIB

This chapter will discuss the motivation and preparation for a  $^{80}\text{Ge}(\text{d,p})^{81}\text{Ge}$  reaction experiment, to be measured at 45 MeV/u for direct comparison to the previously measured reaction at 3.9 MeV/u by Ahn *et al.* [Ahn13; Ahn19].

$^{81}\text{Ge}$  has one hole in the neutron closed N=50 shell, and four valence protons above the Z=28 closed shell. The ground state is observed to be  $9/2^+$ , consistent with our expectations from a simple shell-model perspective. Due to the notoriously large energy required to excite a valence nucleon above a shell gap, one would expect hole excitations within the 28-50 neutron shell to dominate low-lying excited states, producing excited states with negative parity. In contrast, it has been observed that the first excited J = 1/2 and 5/2 states at 679 keV and 711 keV both have positive parity [Hof81]. The energy of the N=50 shell gap for Ge isotopes was measured to be  $\Delta = S_{2n}(^{82}\text{Ge}) - S_{2n}(^{84}\text{Ge}) = 3.15$  MeV [Hak08], so from a simple shell-model perspective, the positive parity states should be much higher in excitation. These are therefore *intruder states*, resulting from residual interactions between the valence protons and neutrons reducing the size of the shell gap. As these intruder states are dependent on the valence proton - neutron interactions within the nucleus, the effect is most extreme in mid-shell nuclei.

Figure 1.3 shows that final (weak) r-process abundance patterns are sensitive to the direct neutron-capture cross sections of this N=48, Z=32 nucleus. The direct-capture

cross sections are directly related to the spectroscopic factors of states in  $^{81}\text{Ge}$ . Spectroscopic factors with reduced uncertainties are therefore necessary to further constrain r-process nucleosynthesis in this neutron-rich,  $A \approx 80$  region of the chart of nuclides. A lack of knowledge of the bound-state geometry for the potential of the single-neutron wavefunction introduces uncertainties in the calculated differential cross sections, and hence, the extracted spectroscopic factors themselves. The combined method will therefore be adopted to compare the high- and low-energy data, constraining the single-particle ANC and therefore reducing uncertainties on the extracted spectroscopic factors.

#### 4.1 $^{80}\text{Ge}(\text{d,p})^{81}\text{Ge}$ at 3.9 MeV/u

The recent measurement by Ahn *et al.* [Ahn19] was the first transfer reaction to study these low lying intruder states in  $^{81}\text{Ge}$  through  $^{80}\text{Ge}(\text{d,p})$  at 3.9 MeV/u. Similar to the motivation for the  $^{84}\text{Se}(\text{d,p})$  reaction described in Chapter One, the goal of this experiment was to determine spectroscopic factors of the  $1/2^+$  and  $5/2^+$  low lying states at 679 keV and 711 keV, respectively, to inform direct neutron capture on  $^{80}\text{Ge}$  for r-process nucleosynthesis.

To determine these spectroscopic factors, a  $^{80}\text{Ge}$  beam at 3.875 MeV/u bombarded a  $174 \mu\text{g}/\text{cm}^2$ -thick  $\text{CD}_2$  target at the Holifield Radioactive Ion Beam Facility (HRIBF). Multiple silicon detector types surrounded the target, including Micron S1, SX3 and BB15 detectors as well as one SIDAR detector. A fast ionization chamber was placed downstream of the target to identify different beam components, and for beam normalization. See reference [Ahn19] for more details on the experimental setup.

The separation of these states is significantly smaller than the center of mass energy resolution of this configuration, and therefore must be analyzed as an unresolved

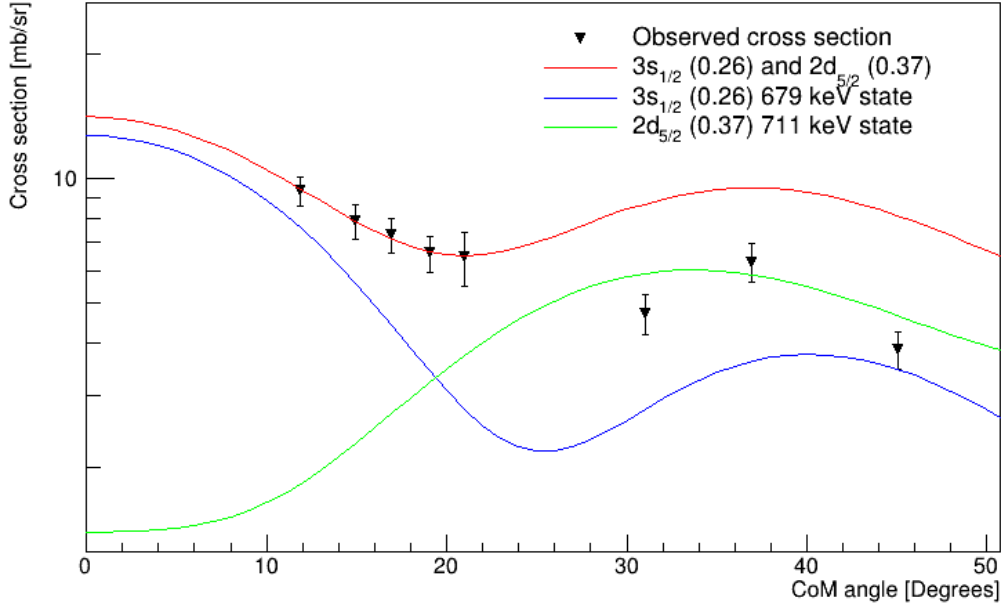


Figure 4.1:  $^{80}\text{Ge}(d,p)$  transfer cross section to the unresolved doublet at 700 keV compared to FR-ADWA predictions assuming  $3s_{1/2}$  and  $2d_{5/2}$  configurations for the 679 keV and 711 keV states, respectively. Fits are to the first 5 data points only. Data from [Ahn19].

doublet. Ahn *et al.* used this technique to analyze the doublet within the FR-ADWA theoretical framework, assuming the canonical values of  $r_0$  and  $a$ , as shown in Figure 4.1. In general, calculated transfer cross sections better represent the data at the first peak in the angular distribution. Therefore, fits to the data were only applied to the five most forward-angle data points. The plotted error bars are purely statistical in nature.

In preparation for the higher energy measurement, these data have now been analyzed for the same range of radius and diffuseness parameters as described in Table 2.4. This is shown in Figures 4.2 and 4.3.

The deduced spectroscopic factors and many-body ANCs as a function of single-particle ANCs are shown in Figure 4.3. The plotted error bars represent the statistical best-fit uncertainty, and uncertainties in target thickness (13%) and detector setup

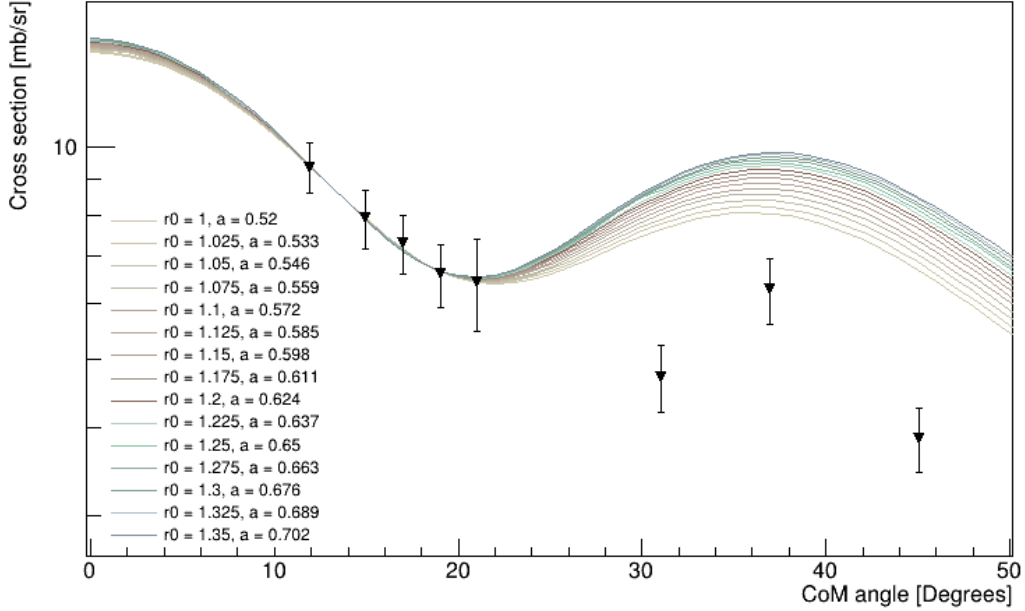


Figure 4.2:  $^{80}\text{Ge}(d,p)$  transfer cross section to the unresolved doublet at 700 keV compared to FR-ADWA predictions assuming  $3s_{1/2}$  and  $2d_{5/2}$  configurations for a range of radius and diffuseness parameters. Fits are only to the first 5 data points.

geometry (10%) [Ahn19].

The deduced many-body ANC shows little dependence on the single-particle ANC, and therefore, the radius and diffuseness of the bound state potential. This concurs with our expectations of a peripheral probe of the nuclear wavefunction. The deduced spectroscopic factors, however, vary by a factor of three across the range of single-particle ANCs (corresponding to a 30% variation in  $r_0$  and  $a$ ). Measuring this reaction at a higher beam energy (45 MeV/u) will enable a constraint to be made on the single-particle ANCs, significantly reducing the uncertainties due to the unknown bound-state geometry.

## 4.2 Preparation for $^{80}\text{Ge}(d,p)^{81}\text{Ge}$ at 45 MeV/u

To address the uncertainties due to the unknown bound-state potential geometry, the  $^{80}\text{Ge}(d,p)$  reaction at 45 MeV/u was proposed and approved to run at the National

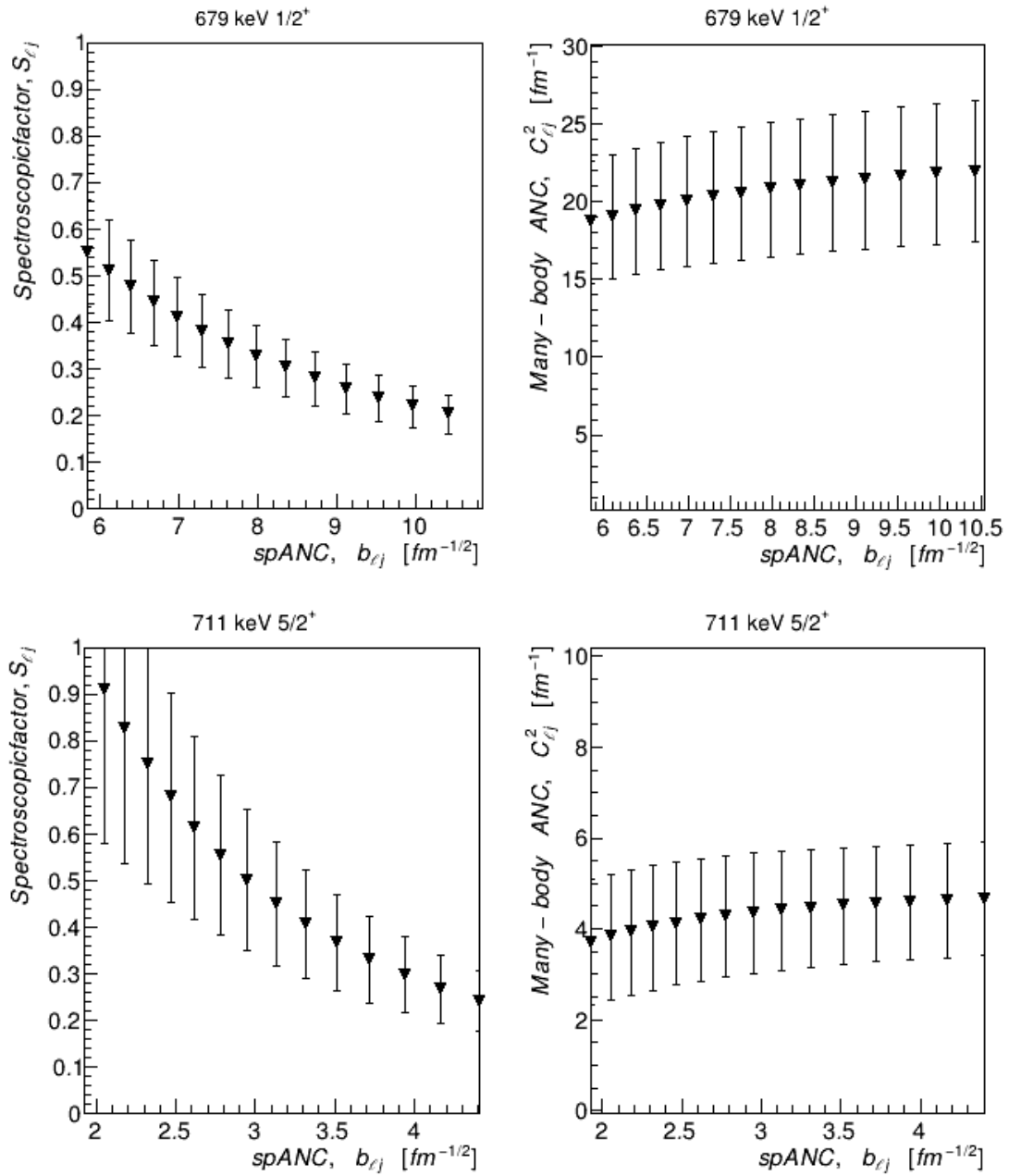


Figure 4.3: Deduced spectroscopic factors and many-body ANCs from the  $^{80}\text{Ge}(\text{d},\text{p})$  measurement at 3.787 MeV/u as a function of single-particle ANC for the  $1/2^+$  and  $5/2^+$  states at 679 keV and 711 keV respectively.

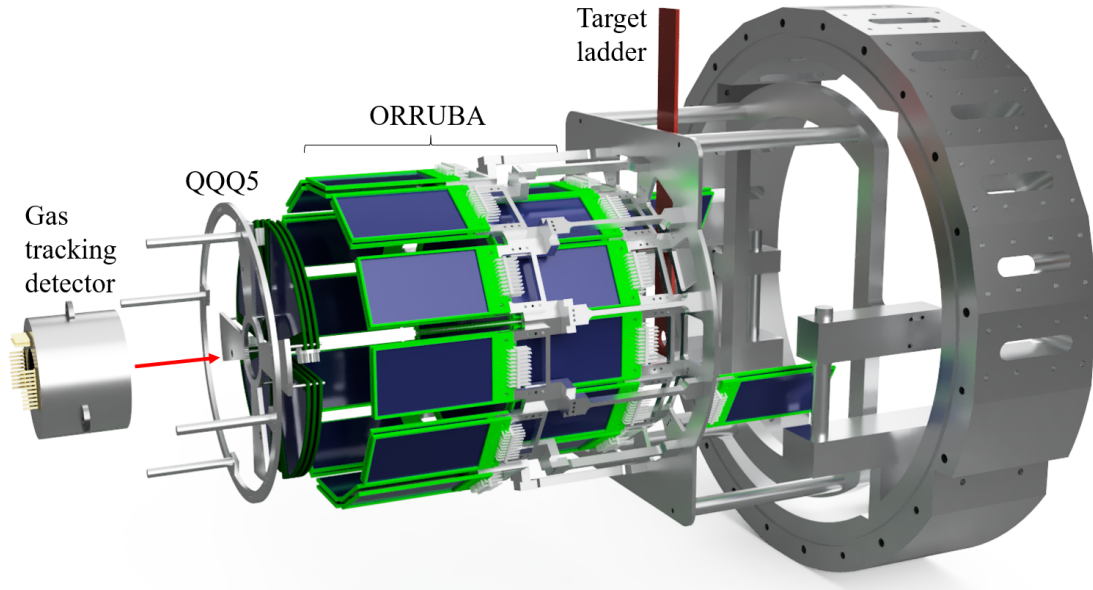


Figure 4.4: Proposed setup for the  $^{80}\text{Ge}(d,p)$  reaction at 45 MeV/u. ORRUBA and QQQ5 detectors surround the target at backward angles, with two ORRUBA detectors upstream for elastic scattering monitoring. All detectors will be deployed in a dE-E configuration. Beam direction is left to right.

Superconducting Cyclotron Laboratory in November of 2020.

#### 4.2.1 Experimental setup

The experimental setup to be used is shown in Figure 4.4. This will once again use ORRUBA to detect reaction protons in coincidence with the heavy ion recoil detected in the S800 focal plane. At the largest scattering angles, QQQ5 detectors will be deployed instead of SIDAR. This lends several advantages for the setup. Firstly, the inner radius of the QQQ5 detectors is smaller than the YY1 detectors that populate SIDAR. Reaction protons can therefore be measured to even larger angles in the laboratory, corresponding to very small angles in the center-of-mass frame. This will help constrain the fit of the FR-ADWA predicted cross sections for the s-wave transfer which peaks at zero degrees in the center of mass frame. Secondly, the QQQ5 detectors have 32 graduated radially-segmented strips on the front side. This is double the number of

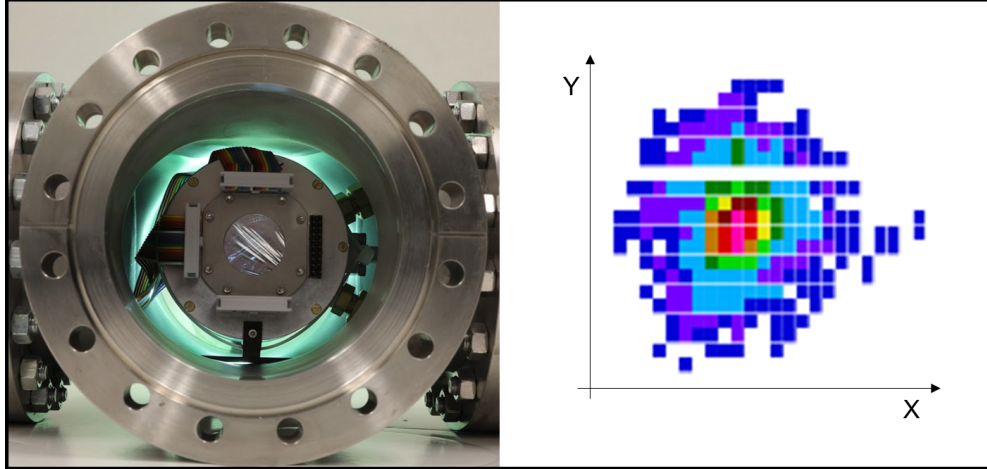


Figure 4.5: (*left*) Photograph of Gas Tracking Detector from the beam's perspective (Courtesy of Steve Pain). (*right*) Position reconstruction from wire grid anodes.

radial strips present in the YY1 detectors (16), significantly increasing the polar angle resolution. Finally, back-side segmentations of  $23^\circ$  provides finer segmentation (SIDAR has  $60^\circ$  segmentations) in the azimuthal scattering angle. This becomes important when implementing beam tracking to deduce the interaction point between the beam and the target, as an azimuthal measurement of the scattering angle is necessary to deduce the actual scattering angle - particularly if the beam is not perfectly on-axis.

For the  $^{84}\text{Se}$  measurement at 45 MeV/u, the Multi Channel Plate (MCP) detectors provided no position sensitivity due to difficulties in tuning the magnetic field to guide the electrons to the MCP face. The large size of the MCP setup also restricts the detector geometries that they can be mounted to. Therefore for this measurement, beam tracking will be implemented using newly developed gas tracking detectors.

An ionizable gas (P10, isobutane or  $\text{CF}_4$ ) is circulated through a small cylindrical chamber (2" long, 3" diameter) at a pressure of approximately 50 Torr. As the beam passes through and ionizes the gas, two perpendicular gold-plated (0.0007" diameter) wire grids of anodes spaced 2 mm apart detect the electrons to provide a position

reconstruction in the x-y plane. Sub-grid resolution can be achieved by comparing the signal from two adjacent wires. These have a significantly smaller x-y profile than the MCP, and can be mounted in a 4" diameter beam pipe. They therefore can be used with substantially smaller detector geometries, which is particularly important when also using auxiliary detectors (such as gamma-ray detector arrays: GRETINA or Gammasphere). The simplicity of operation of these detectors also increases the probability of a successful measurement. For the  $^{84}\text{Se}(d,p)$  measurement with MCPs, a substantial amount of the setup time was spent fine-tuning the setup to try and achieve position sensitivity.

The S800 magnetic spectrograph will once again be used to detect the heavy-ion recoil in coincidence with ejected protons. During the previous measurement of  $^{84}\text{Se}(d,p)$  at 45 MeV/u, the rate-limited gas detectors necessitated a beam blocker to stop the unreacted  $^{84}\text{Se}$ . This also blocked  $\sim 73\%$  of the  $^{85}\text{Se}$ . To maximize the transmission of  $^{81}\text{Ge}$  through the S800, it is possible to turn off the rate-limiting detectors (CRDCs and ionization chamber). Instead, the timing signal between the S800 scintillator and the ORRUBA detectors could be used to suppress the background from beam-target interactions. As a result of this, the beam blocker could be pulled further out - increasing the proton- $^{81}\text{Ge}$  coincident statistics.

This will, however, sacrifice the ability to separate ions that make it to the S800 focal plane, relying only on the timing signal from the S800 scintillator. Differences between the Q value spectrum generated from coincidences with  $^{85}\text{Se}$  identified in the S800 PID, and just timing coincidence with the S800 scintillator are negligible between the ground-state Q value and the neutron separation energy. At large, negative Q value (corresponding to very high in excitation energy  $\sim 20$  MeV), some background from

the  $^{84}\text{Br}$  beam contaminant (with similar magnetic rigidities to the recoil of interest) contributes to the timing-coincident Q-value spectrum. This is outside of the region that can be analyzed to extract spectroscopic factors in  $^{85}\text{Se}$ , and therefore can be ignored.

### 4.2.2 Simulations

To optimize the  $^{80}\text{Ge}(\text{d},\text{p})$  experimental setup, a range of Monte-Carlo simulations were performed with VIKAR4.2 [Pai18a]. VIKAR calculates the ejected proton energies and angles, based upon experimental configurations such as target thickness, beam characteristics and detector location. Figure 4.6 shows the predicted Q value resolution as a function of target thickness for a range of different beam momentum dispersions with beam tracking switched on/off. This was calculated for the ORRUBA barrels and the QQQ5 detectors.

Figure 4.6 clearly demonstrates that beam tracking is most critical for the ORRUBA barrel. This is due to the increased Q-value sensitivity to the angular measurement at these scattering angles. The momentum dispersion of the beam is determined using collimating slits. Pulling the slits out increases the beam transmission, but also increases the spread in beam energy at the point of interaction with the target - influencing the Q value resolution. The finite thickness of the target also introduces uncertainties in reaction energies, due to the energy loss of the beam in the target. To a first order approximation, the relationship between momentum acceptance of the beam, and the number of beam particles on target is linear. The momentum spread of the beam at the target position is simulated in Figure 4.7 using LISE++. The fraction of expected statistics relative to 1%  $\text{dp}/\text{p}$  momentum acceptance and  $1\text{ mg}/\text{cm}^2$  target thickness is

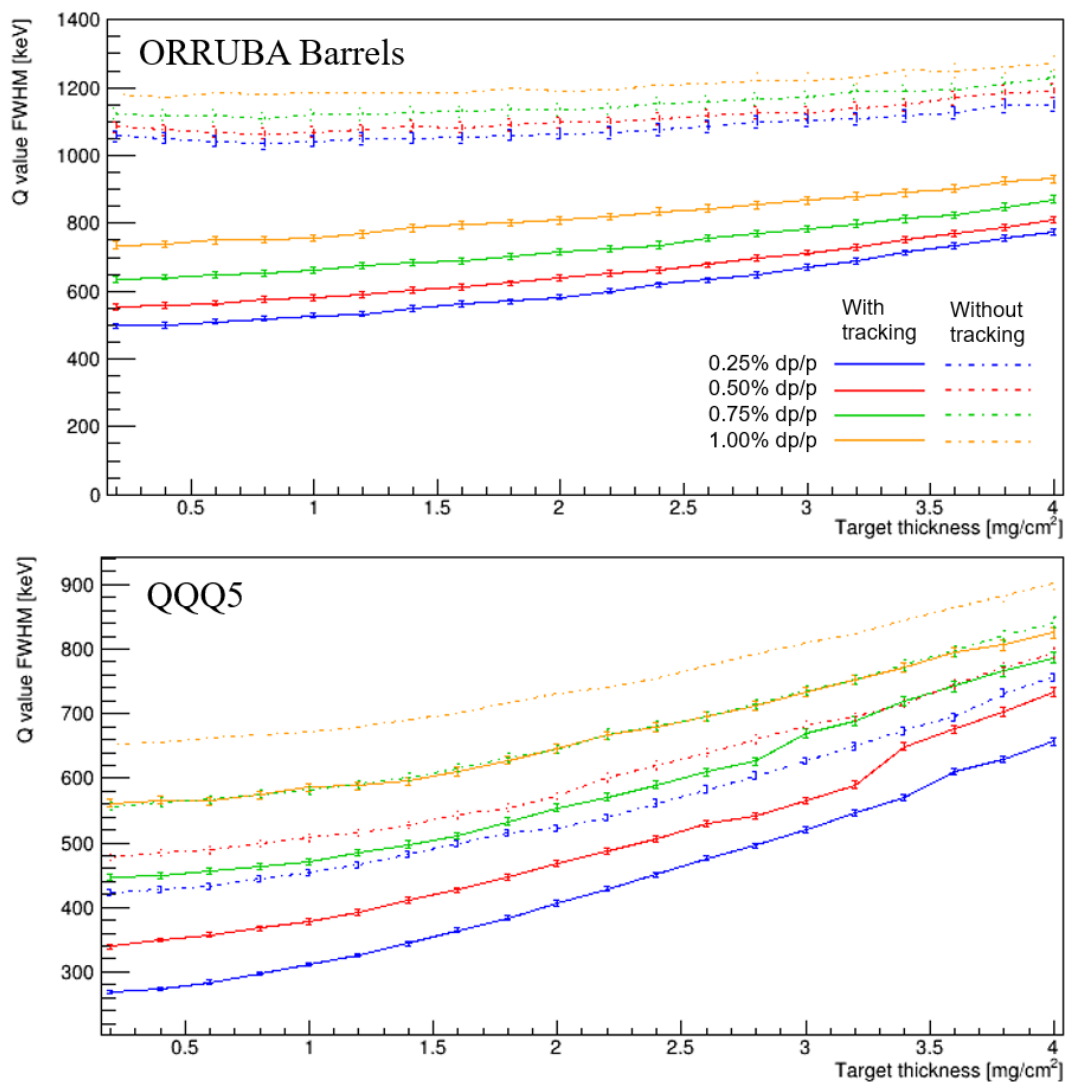


Figure 4.6: (*Top*) FWHM of the 679 keV state as a function of target thickness for a variety of momentum dispersions with and without beam tracking implemented for the ORRUBA barrels. (*Bottom*) Same as the top, but for the QQQ5 detectors.

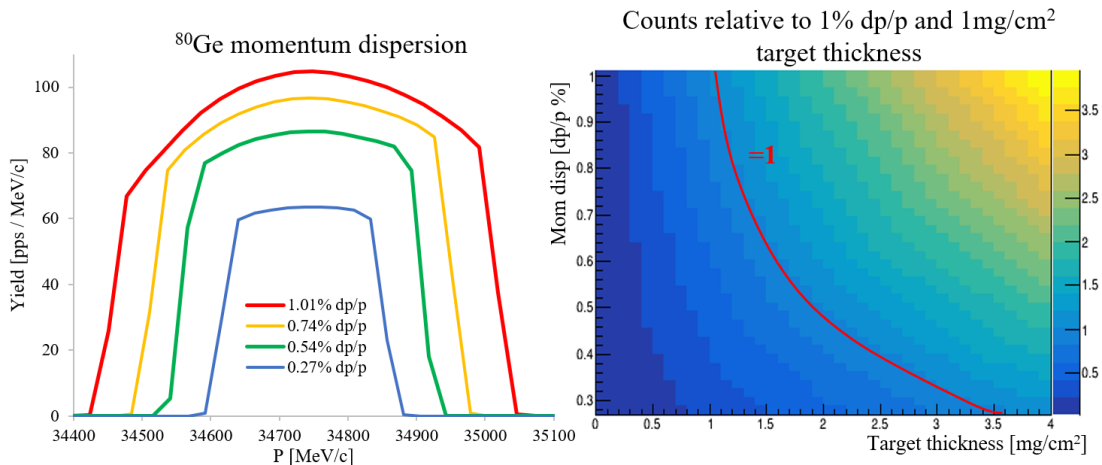


Figure 4.7: (*Left*) Predicted momentum spread of  $^{80}\text{Ge}$  at the target as a function of momentum acceptance, calculated using LISE++. (*Right*) Fraction of expected counts relative to 1% dp/p momentum acceptance and 1 mg/cm<sup>2</sup> target thickness.

also displayed.

Analyzing the predicted resolution and relative counts as a function of these parameters is extremely useful in configuring these experimental setups, balancing the quality of data with the statistics. To ensure separation from the next excited state at 1241 keV, a resolution of approximately  $\sim 500\text{-}600$  keV is necessary. Figures 4.6 and 4.7 therefore informs the configuration that maximizes statistics within these constraints, increasing the probability for a successful measurement.

### 4.3 Coupling ORRUBA with GRETINA and Day-1 FRIB

Further measurements of spectroscopic information on neutron-rich nuclei away from stability are necessary to accurately calculate neutron-capture rates of r-process nuclei. However, measurements become significantly more challenging moving further from stability, primarily due to low radioactive ion beam (RIB) rates. To address the current lack of available neutron-rich beams, the Facility for Rare Isotope Beams (FRIB) will

come online at Michigan State University in 2022. FRIB will provide unprecedented rates of unstable and neutron-rich RIBs, many of which have never previously been produced at an accelerator facility at energies appropriate for direct reactions.

The highest RIB rates will only be available as “fast beams”, as stopping and re-accelerating beams significantly reduces the delivered intensity. For Day-1 FRIB, the large solid-angle High Purity Germanium (HPGe) gamma-ray tracking array GRETINA [Cro15] will be installed in front of the S800 magnetic spectrograph in the fast-beam area. GRETINA is constructed of two hemispheres of detector modules, split in the plane of the beam and the vertical axis. The  $\sim 2$  keV energy resolution (at  $E_\gamma \approx 1.33$  MeV) of HPGe detectors [Kno10] can separate high densities of states, which, when measured together with charged-particle spectroscopy, provides significant advantages in measuring the spectroscopic information of neutron-rich nuclei.

The Gammasphere - ORRUBA: Dual Detectors for Experimental Structure studies (GODDESS) [Pai17] setup was developed to achieve this using the Gammasphere HPGe detector array [Lee90]. GODDESS was commissioned in 2015 using stable heavy ion beams accelerated through the Argonne Tandem Linear Accelerator System (ATLAS) to Gammasphere. ORRUBA was mounted at the Gammasphere target position for charged-particle spectroscopy. Commissioning experiments included (d,p) reactions on beams of  $^{134}\text{Xe}$  and  $^{95}\text{Mo}$ , as well as a measurement of the  $^{16}\text{F}(^3\text{He,t})^{19}\text{Ne}$  reaction in normal kinematics ( $^3\text{He}$  as the beam).

More recently, GODDESS has been deployed using GRETINA to detect gamma-rays in coincidence with charged particles for measurements of the  $^{56}\text{Fe}(p,p')$ ,  $^{134}\text{Te}(d,p\gamma)^{135}\text{Te}$  and  $^{30}\text{P}(d,p\gamma)^{31}\text{P}$  reactions on the ATLAS beamline. The  $^{56}\text{Fe}(p,p')$  reaction was measured in normal kinematics, using a stable proton beam. The

$^{134}\text{Te}(d,p\gamma)^{135}\text{Te}$  reaction was measured in inverse kinematics, using a radioactive beam of  $^{134}\text{Te}$ , produced using the CALifornium Rare Isotope Breeder Upgrade (CARIBU) [Par07]. The  $^{30}\text{P}(d,p\gamma)^{31}\text{P}$  reaction was measured using an in-flight developed beam of  $^{30}\text{P}$  (primary beam  $^{29}\text{Si}$ ) from RAISOR [dickerson].

These experiments used the same target chamber that was developed for GODDESS with Gammasphere. GRETINA has a smaller internal radius (178 mm) than Gammasphere does, resulting in GRETINA not being able to fully close around the ORRUBA chamber that was designed for use with Gammasphere. If GRETINA was fully populated with detector modules, the curved detectors that lie along the split of the hemispheres reduces the effective radius of a chamber that can be closed-upon by GRETINA to 160.2 mm. The currently sparse population of GRETINA detectors allowed for their positioning to be away from the split, such that there was minimal interference between the ORRUBA chamber and the GRETINA detectors. This allowed for GRETINA to be as close as possible to the ORRUBA chamber, though still not fully closed - reducing the geometric efficiency of the  $\gamma$ -detector array. The inherently small ( $\sim 11\%$ ) intrinsic efficiency associated with HPGe detectors indicates the importance of maximizing the geometric efficiency.

To address this, GODDESS has been redesigned for use with GRETINA, as well as allowing capabilities to run with the upgraded (and fully populated) GRETA. A 3D rendering of the newly designed GODDESS setup is displayed in Figures 4.8 and 4.9. The setup consists of a custom chamber designed to house the gas-tracking detectors described in section 4.2.1, as well as a new scattering chamber that allows GRETINA to fully close around ORRUBA. The designs of the scattering chamber are shown in Figures 4.10 and 4.11.

The main design change from the old Gammasphere chamber is the smaller internal radius, and the cylindrical mid-section. The cylindrical mid-section reduces the effective radius of the scattering chamber in the plane of the hemispheres, allowing for GRETINA to fully close around the ORRUBA charged-particle array. Reducing the size of the ORRUBA array to fit inside of GRETINA brings the silicon detectors closer to the target - reducing the charged-particle resolution. Detecting gamma-rays in coincidence, however, helps with the analysis of excitation spectra.

For the gas-tracking chamber (shown in Figure 4.12), the dimensions were chosen such that GRETA will still be able to fully close. Smaller HPGe detector modules (triplet-crystal modules instead of quads) can be placed at the positions closest to the beam axis, to allow for a beam pipe with approximately a 10 cm diameter to enter the array from the upstream side. The gas-tracking chamber will allow the gas-tracking detectors to be installed as close as possible to the target position, without interfering with the GRETINA detectors. This is important to improve the angular resolution of the charged-particle detectors, especially since they are moved closer to the target in this configuration.

This setup was originally designed for the  $^{80}\text{Ge}(d,p\gamma)$  measurement at 45 MeV/u at the NSCL. However, due to COVID-19 shutdowns, the experiment had to be postponed until after GRETINA had left the NSCL for a campaign at Argonne National Laboratory. If the  $^{80}\text{Ge}(d,p)$  measurement gets delayed further (past the shutdown of the Coupled Cyclotron Facility - once FRIB is online), this setup could be used to measure  $^{80}\text{Ge}(d,p\gamma)$ , to increase the resolution of the measured excitation energies.

The  $(d,p\gamma)$  reaction has recently been validated [Rat19] as a surrogate for  $(n,\gamma)$  reactions that proceed via a compound nucleus (CN). The equilibrated CN “forgets” its

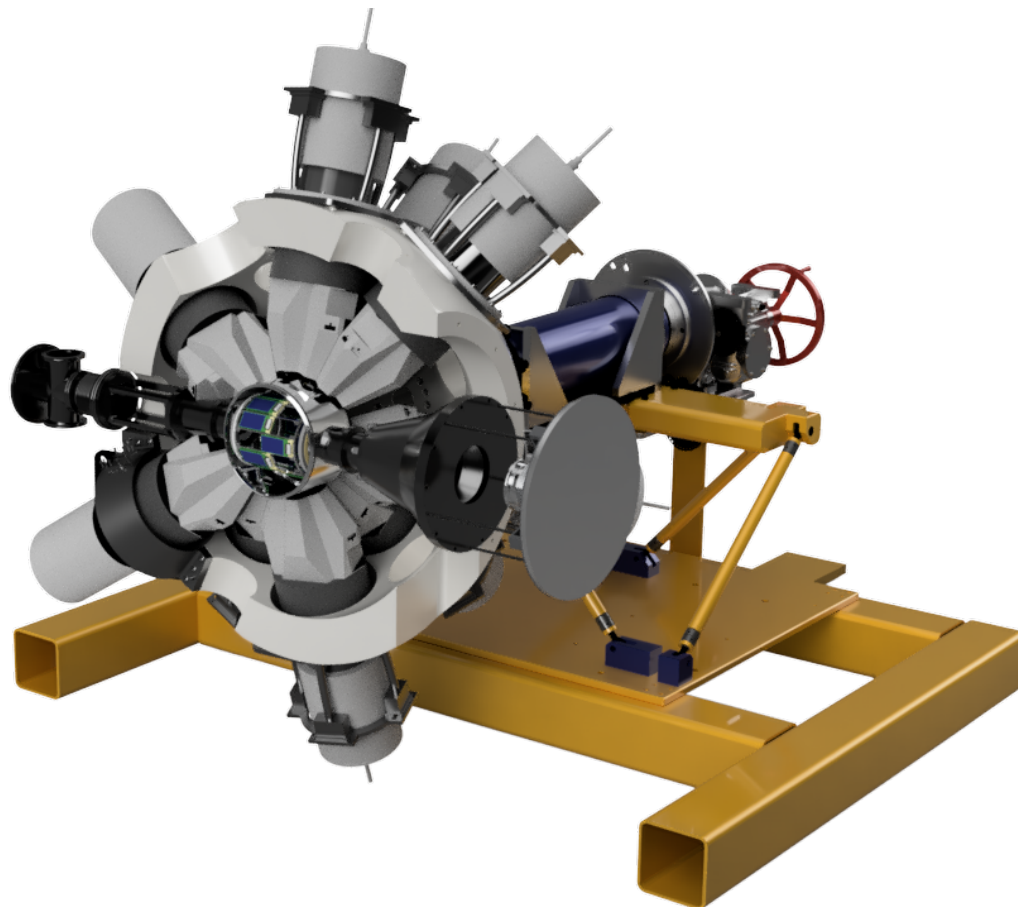


Figure 4.8: 3D rendering of GODDESS, full view. Beam direction is left to right. GRETINA surrounds ORRUBA inside a new custom scattering chamber, with a custom pipe designed to house gas tracking detectors located immediately upstream.

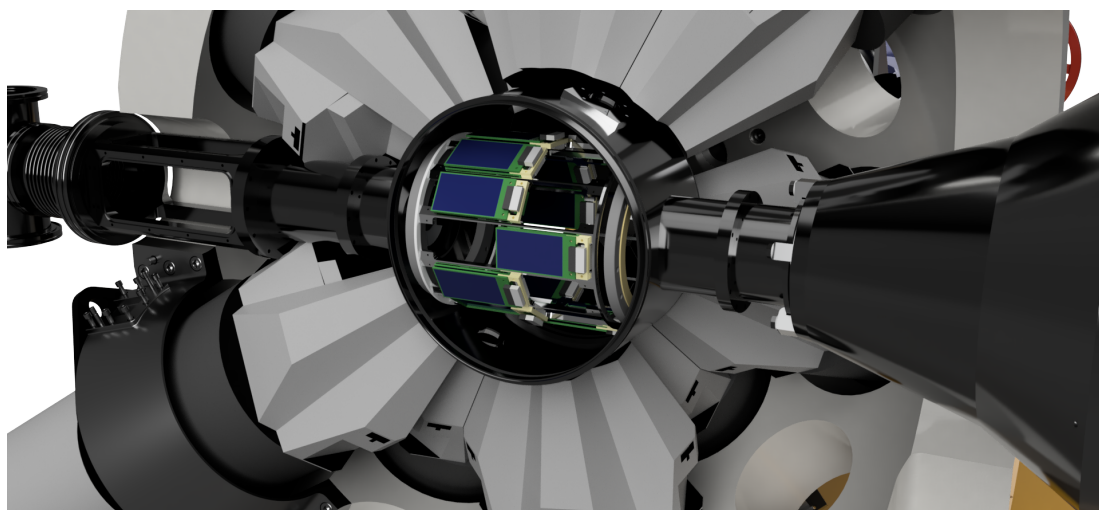


Figure 4.9: 3D rendering of GODDESS, zoomed in on the ORRUBA barrel. Beam direction is left to right.

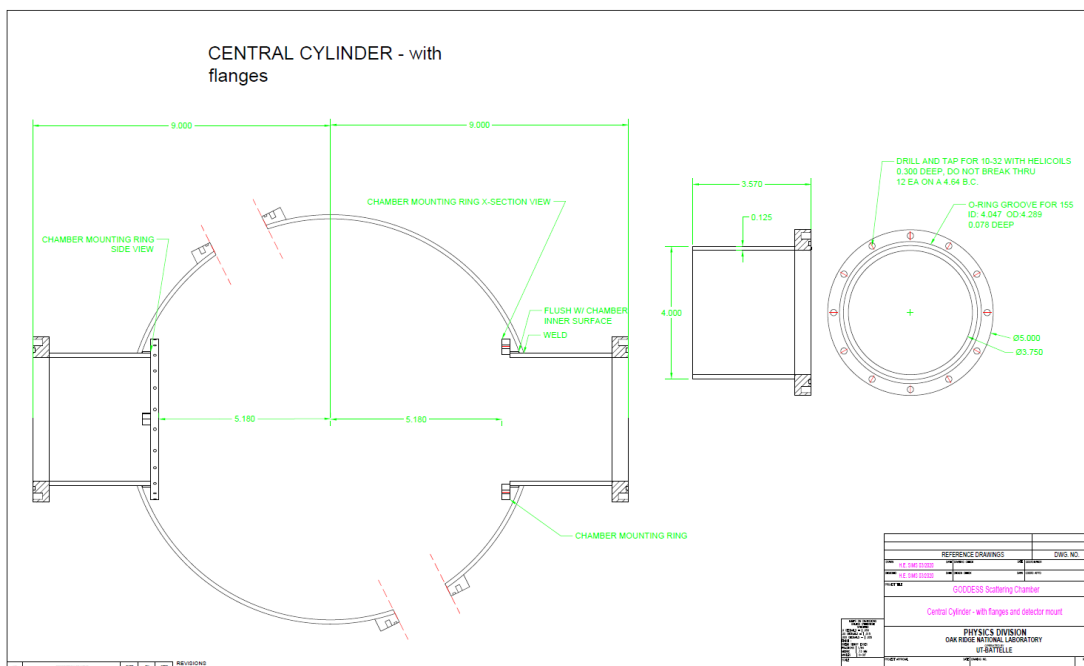


Figure 4.10: Machine-shop drawing of newly designed GODDESS chamber - side view, with connecting flanges and detector mounting ring shown.

formation process, such that the decay probabilities of the CN can then be measured. This is used with the theoretically calculated formation cross section to deduce the CN ( $n, \gamma$ ) cross section. This surrogate method could therefore be used to deduce the CN ( $n, \gamma$ ) cross section on  $^{80}\text{Ge}$ , as well as the DSD cross section, if GRETINA were available for the measurement. This would be more challenging than the previous surrogate measurement on  $^{95}\text{Mo}$ , due to the lack of a strong collecting transition in  $^{81}\text{Ge}$ .

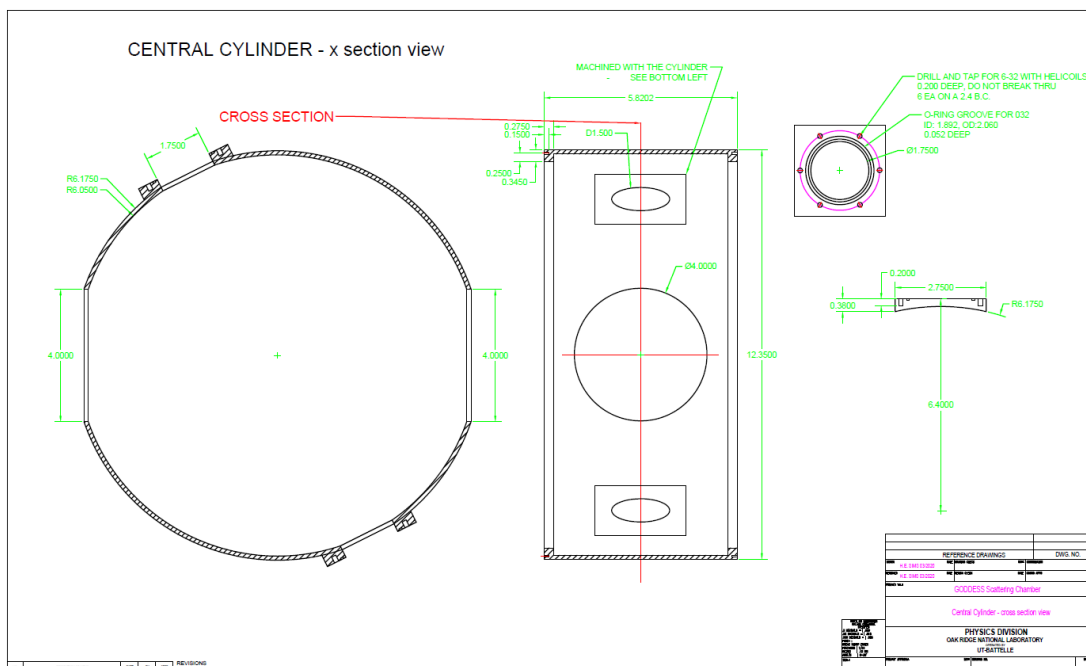


Figure 4.11: Machine-shop drawing of newly designed GODDESS chamber - cross section view.

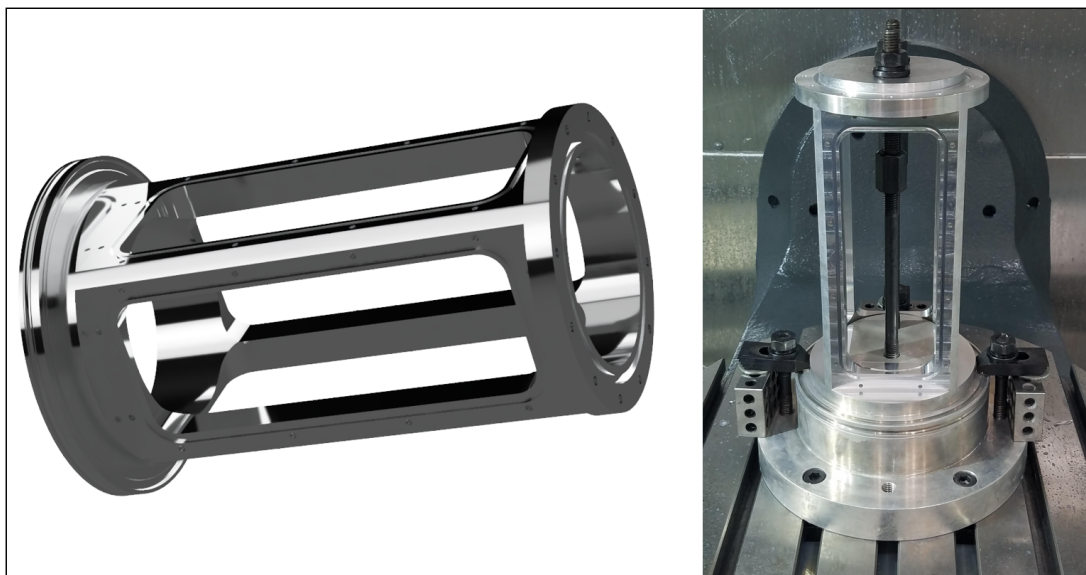


Figure 4.12: (Left) 3D rendering of the custom chamber designed to house gas tracking detectors upstream of the target. (Right) Photo of the gas tracking chamber being manufactured using a 5-axis machine at the University of Tennessee.

## Chapter 5

### Summary, Conclusions and Future work

The  $^{84}\text{Se}(d,p)^{85}\text{Se}$  reaction was measured at 45 MeV/u at the National Superconducting Cyclotron Laboratory (NSCL) for direct comparison to the same reaction at 4.5 MeV/u, to constrain the bound-state potential for the ground- and first-excited (0.462 MeV) states in  $^{85}\text{Se}$ . This significantly reduced the uncertainties in the deduced spectroscopic factors, as the dominating uncertainty in their extraction is the unknown bound-state geometry.

This study has deduced the angular differential cross sections for the  $^{84}\text{Se}(d,p)^{85}\text{Se}$  reaction at 45 MeV/u to the ground- and first excited-state, and compared to theoretical predictions using Finite-Range ADiabatic Wave Approximation (FR-ADWA) framework. The reaction at 4.5 MeV/u was also re-analyzed within the same theoretical framework. From the peripheral measurement, the many-body ANCs were deduced to be  $2.97\pm 0.50$  and  $15.0\pm 3.4$  for the ground- and first-excited states, respectively. The deduced single-particle ANCs were constrained within the combined method formalism to be  $3.55\pm 0.33 \text{ fm}^{-1/2}$  and  $7.37\pm 0.81 \text{ fm}^{-1/2}$  for the ground- and first-excited states, respectively. Through Equation 2.3, the spectroscopic factors of the ground- and first-excited states are therefore deduced to be  $0.28\pm 0.05$  and  $0.26\pm 0.07$ , respectively. Uncertainties include the statistical fitting uncertainty, uncertainty due to the choice in optical model, and systematic uncertainties in the normalization, as listed in

Table 3.4. The same analysis was also conducted using a Distorted Wave Born Approximation (DWBA) theoretical interpretation, yielding larger spectroscopic factors than those deduced through the FR-ADWA interpretation.

Using the newly constrained spectroscopic factors for the ground- and first-excited states, Direct-Semi Direct (DSD) neutron capture calculations were performed using the code CUPIDO. Comparisons were made between DSD cross sections using the newly constrained bound-state potential radius and diffuseness parameters and those using canonical values (Figure 3.43). The reduced spectroscopic factors, and bound-state radius and diffuseness parameters used in these calculations reduced the DSD cross section by  $\sim 42\%$  compared with calculations using canonical  $(r_0, a)$  values for the bound-state potential and spectroscopic factors from reference [Tho07].

Continuing the spectroscopic study of  $A \approx 80$  nuclei near the r-process path, the  $^{80}\text{Ge}(d,p)$  reaction at 45 MeV/u is scheduled to be measured in November 2020 at the NSCL. ORRUBA will be used with QQQ5 end-cap detectors to measure reaction protons in coincidence with the  $^{81}\text{Ge}$  recoil nucleus, detected using the S800 magnetic spectrograph. In preparation for this measurement, multiple Monte-Carlo simulations have been performed with different setup parameters, in order to guide the optimization of the experimental setup.

A previous study of the  $^{80}\text{Ge}(d,p)$  reaction at 3.875 MeV/u was conducted Ahn *et al.* [Ahn19] in inverse kinematics using a radioactive beam of  $^{80}\text{Ge}$  produced at the Holifield Radioactive Ion Beam Facility (HRIBF). The doublet of states at  $\sim 700$  keV has been analyzed within the FR-ADWA formalism for a range of bound-state radius and diffuseness parameters, as shown in Figure 4.3. To constrain the single-particle ANC and reduce uncertainties in the extracted spectroscopic factors, the combined

method will be deployed; comparing the many-body ANC and spectroscopic factors as a function of single-particle ANC for both the high- and low-energy reactions.

As FRIB comes online and neutron-rich beams even further from stability become available, additional  $(n,\gamma)$  rates on sensitive r-process nuclei can be deduced. Indeed, one of the more sensitive nuclei in the  $A\approx 80$  region is  $^{87}\text{Se}$ , as can be seen in Figure 1.3 [Sur14]. Currently, this isotope cannot be produced in substantial quantities and at appropriate energies for direct reactions. The estimated fast-beam rates for  $^{87}\text{Se}$  on FRIB day-1 are  $2.68 \times 10^5$  particles per second (pps), with an increase to  $2.15 \times 10^7$  expected as the ultimate rate. Measuring  $(d,p\gamma)$  on this nucleus using GODDESS would inform the DSD  $(n,\gamma)$  cross section, as well as statistical  $(n,\gamma)$  via a compound nucleus using the surrogate method described in Section 4.3. There is currently no level scheme associated with  $^{88}\text{Se}$ , therefore measuring gamma rays will help determine excitation energies, and the measured angular distributions of the reaction protons will infer spin-parities.

## Bibliography

- [Abb17] B. P. Abbott et al. “Multi-messenger Observations of a Binary Neutron Star Merger”. In: *The Astrophysical Journal* 848.2 (Oct. 2017), p. L12. DOI: 10.3847/2041-8213/aa91c9.
- [Ahn13] Sunghoon Ahn. “The study of nuclear structure of neutron-rich  $^{81}\text{Ge}$  and its contribution in the r-process via the neutron transfer reaction  $^{80}\text{Ge}(d,p)$ .” PhD thesis. University of Tennessee, 2013.
- [Ahn19] S. Ahn et al. “Direct neutron capture cross section on  $^{80}\text{Ge}$  and probing shape coexistence in neutron-rich nuclei”. In: *Phys. Rev. C* 100 (4 Oct. 2019), p. 044613. DOI: 10.1103/PhysRevC.100.044613. URL: <https://link.aps.org/doi/10.1103/PhysRevC.100.044613>.
- [Arc11] A. Arcones and G. Martinez-Pinedo. “Dynamical r-process studies within the neutrino-driven wind scenario and its sensitivity to the nuclear physics input”. In: 83.4, 045809 (Apr. 2011), p. 045809. DOI: 10.1103/PhysRevC.83.045809. arXiv: 1008.3890 [astro-ph.SR].
- [Bar01] D. W. Bardayan et al. “Destruction of  $^{18}\text{F}$  via  $^{18}\text{F}(p,\alpha)^{15}\text{O}$  burning through the  $E_{c.m.} = 665$  keV resonance”. In: *Phys. Rev. C* 63 (6 May 2001), p. 065802. DOI: 10.1103/PhysRevC.63.065802. URL: <https://link.aps.org/doi/10.1103/PhysRevC.63.065802>.

- [Bel03] T. Belgya. *Reference Input Parameter Library (Phase-II)*. 2003. URL: <https://www-nds.iaea.org/RIPL-2/>.
- [Beu08] J Beun et al. “Neutron capture on  $^{130}\text{Sn}$  during  $r$ -process freeze-out”. In: *Journal of Physics G: Nuclear and Particle Physics* 36.2 (Nov. 2008), p. 025201. DOI: 10.1088/0954-3899/36/2/025201. URL: <https://doi.org/10.1088/0954-3899/36/2/025201>.
- [Cas00] R. F. Caston. *Nuclear Structure from a Simple Perspective*. Oxford science publications. Oxford University Press, 2000. ISBN: 9780198507246. URL: <https://books.google.com/books?id=WgKTQoX13MUC>.
- [Chi08] S. Chiba et al. “Direct and semi-direct capture in low-energy ( $n, \gamma$ ) reactions of neutron-rich tin isotopes and its implications for  $r$ -process nucleosynthesis”. In: *Phys. Rev. C* 77 (1 Jan. 2008), p. 015809. DOI: 10.1103/PhysRevC.77.015809. URL: <https://link.aps.org/doi/10.1103/PhysRevC.77.015809>.
- [Cow06] John J. Cowan and Christopher Sneden. “Heavy element synthesis in the oldest stars and the early Universe”. In: *Nature* 440.7088 (Apr. 2006), pp. 1151–1156. ISSN: 1476-4687. DOI: 10.1038/nature04807. URL: <https://doi.org/10.1038/nature04807>.
- [Cro15] M Cromaz. “The GRETINA Spectrometer”. In: *Journal of Physics: Conference Series* 606 (May 2015), p. 012016. DOI: 10.1088/1742-6596/606/1/012016. URL: <https://doi.org/10.1088/1742-6596/606/1/012016>.

- [Dae80] W. W. Daehnick, J. D. Childs, and Z. Vrcelj. “Global optical model potential for elastic deuteron scattering from 12 to 90 MeV”. In: *Phys. Rev. C* 21 (6 June 1980), pp. 2253–2274. DOI: 10.1103/PhysRevC.21.2253. URL: <https://link.aps.org/doi/10.1103/PhysRevC.21.2253>.
- [Dob96] J. Dobaczewski et al. “Mean-field description of ground-state properties of drip-line nuclei: Pairing and continuum effects”. In: *Phys. Rev. C* 53 (6 June 1996), pp. 2809–2840. DOI: 10.1103/PhysRevC.53.2809. URL: <https://link.aps.org/doi/10.1103/PhysRevC.53.2809>.
- [Feb17] M. Febbraro et al. “Improved technique for preparation of deuterated-polyethylene targets”. In: *Nucl. Instrum. Meth., Phys. Res. B* 410 (Nov. 2017), pp. 53–59. DOI: 10.1016/j.nimb.2017.07.036.
- [For53] Kenneth W. Ford. “The First Excited States of Even-Even Nuclei”. In: *Phys. Rev.* 90 (1 Apr. 1953), pp. 29–44. DOI: 10.1103/PhysRev.90.29. URL: <https://link.aps.org/doi/10.1103/PhysRev.90.29>.
- [Hak08] J. Hakala et al. “Evolution of the  $N = 50$  Shell Gap Energy towards  $^{78}\text{Ni}$ ”. In: *Phys. Rev. Lett.* 101 (5 July 2008), p. 052502. DOI: 10.1103/PhysRevLett.101.052502. URL: <https://link.aps.org/doi/10.1103/PhysRevLett.101.052502>.
- [Har70] K. Haravu et al. “ $^{86}\text{Kr}(d,p)^{87}\text{Kr}$  Reaction”. In: *Phys. Rev. C* 1 (3 Mar. 1970), pp. 938–944. DOI: 10.1103/PhysRevC.1.938. URL: <https://link.aps.org/doi/10.1103/PhysRevC.1.938>.

- [Hau52] Walter Hauser and Herman Feshbach. “The Inelastic Scattering of Neutrons”. In: *Phys. Rev.* 87 (2 July 1952), pp. 366–373. DOI: 10.1103/PhysRev.87.366. URL: <https://link.aps.org/doi/10.1103/PhysRev.87.366>.
- [Hof81] P. Hoff and B. Fogelberg. “Properties of strongly neutron-rich isotopes of germanium and arsenic”. In: *Nuclear Physics A* 368.2 (1981), pp. 210–236. ISSN: 0375-9474. DOI: [https://doi.org/10.1016/0375-9474\(81\)90683-7](https://doi.org/10.1016/0375-9474(81)90683-7). URL: <http://www.sciencedirect.com/science/article/pii/0375947481906837>.
- [Joh04] Karen E. Johnson. “From Natural History to the Nuclear Shell Model: Chemical Thinking in the Work of Mayer, Haxel, Jensen, and Suess”. In: *Phys. perspect.* 6 (2004), pp. 295–309. DOI: DOI10.1007/s00016-003-0203-x.
- [Joh70] R. C. Johnson and P. J. R. Soper. “Contribution of Deuteron Breakup Channels to Deuteron Stripping and Elastic Scattering”. In: *Phys. Rev. C* 1 (3 Mar. 1970), pp. 976–990. DOI: 10.1103/PhysRevC.1.976. URL: <https://link.aps.org/doi/10.1103/PhysRevC.1.976>.
- [Joh74] R.C. Johnson and P.C. Tandy. “An approximate three-body theory of deuteron stripping”. In: *Nuclear Physics A* 235.1 (1974), pp. 56–74. ISSN: 0375-9474.
- [Jon10] K. L. Jones et al. “The magic nature of  $^{132}\text{Sn}$  explored through the single-particle states of  $^{133}\text{Sn}$ ”. In: *Nature* 465.7297 (2010), pp. 454–457. DOI: 10.1038/nature09048.

- [Jon11] K. L. Jones et al. “Direct reaction measurements with a  $^{132}\text{Sn}$  radioactive ion beam”. In: *Phys. Rev. C* 84 (3 Sept. 2011), p. 034601. DOI: 10.1103/PhysRevC.84.034601. URL: <https://link.aps.org/doi/10.1103/PhysRevC.84.034601>.
- [Kno10] G.F. Knoll. *Radiation Detection and Measurement*. Wiley, 2010. ISBN: 9780470131480. URL: <https://books.google.com/books?id=4vTJ7UDel5IC>.
- [Kon03] A.J. Koning and J.P. Delaroche. “Local and global nucleon optical models from 1 keV to 200 MeV”. In: *Nuclear Physics A* 713.3 (2003), pp. 231–310. ISSN: 0375-9474. DOI: [https://doi.org/10.1016/S0375-9474\(02\)01321-0](https://doi.org/10.1016/S0375-9474(02)01321-0). URL: <http://www.sciencedirect.com/science/article/pii/S0375947402013210>.
- [Lee90] I-Yang Lee. “The GAMMASPHERE”. In: *Nuclear Physics A* 520 (1990). Nuclear Structure in the Nineties, pp. c641–c655. ISSN: 0375-9474. DOI: [https://doi.org/10.1016/0375-9474\(90\)91181-P](https://doi.org/10.1016/0375-9474(90)91181-P). URL: <http://www.sciencedirect.com/science/article/pii/037594749091181P>.
- [Loh74] J.M. Lohr and W. Haeberli. “Elastic scattering of  $9\hat{a}^{13}$  MeV vector polarized deuterons”. In: *Nuclear Physics A* 232.2 (1974), pp. 381–397. ISSN: 0375-9474. DOI: [https://doi.org/10.1016/0375-9474\(74\)90627-7](https://doi.org/10.1016/0375-9474(74)90627-7). URL: <http://www.sciencedirect.com/science/article/pii/0375947474906277>.
- [Man19] B. Manning. “Informing direct neutron capture on tin isotopes near the  $N = 82$  shell closure”. In: *Phys. Rev. C* 99 (4 Apr. 2019), p. 041302. DOI: 10.

- 1103/PhysRevC.99.041302. URL: <https://link.aps.org/doi/10.1103/PhysRevC.99.041302>.
- [Mar68] J B Marion and F C Young. *NUCLEAR REACTION ANALYSIS*. North Holland Publishing Company (c), 1968.
- [May55] Maria Goeppert Mayer and J Hans D Jensen. *Elementary theory of nuclear shell structure*. New York, NY: Wiley, 1955. URL: <https://cds.cern.ch/record/102444>.
- [Muk05] A. M. Mukhamedzhanov and F. M. Nunes. “Combined method to extract spectroscopic information”. In: *Phys. Rev. C* 72 (1 July 2005), p. 017602. DOI: 10.1103/PhysRevC.72.017602. URL: <https://link.aps.org/doi/10.1103/PhysRevC.72.017602>.
- [Muk08] A. M. Mukhamedzhanov, F. M. Nunes, and P. Mohr. “Benchmark on neutron capture extracted from  $(d, p)$  reactions”. In: *Phys. Rev. C* 77 (5 May 2008), p. 051601. DOI: 10.1103/PhysRevC.77.051601. URL: <https://link.aps.org/doi/10.1103/PhysRevC.77.051601>.
- [Ngu10] N. B. Nguyen, F. M. Nunes, and R. C. Johnson. “Finite-range effects in  $(d, p)$  reactions”. In: *Phys. Rev. C* 82 (1 July 2010), p. 014611. DOI: 10.1103/PhysRevC.82.014611. URL: <https://link.aps.org/doi/10.1103/PhysRevC.82.014611>.
- [Pai09] S. D. Pain et al. “Development of the ORRUBA Silicon Detector Array”. In: *AIP Conference Proceedings* 1090.1 (2009), pp. 570–572. DOI: 10.1063/1.3087087. eprint: <https://aip.scitation.org/doi/pdf/10.1063/1.3087087>.

- 1.3087087. URL: <https://aip.scitation.org/doi/abs/10.1063/1.3087087>.
- [Pai17] S.D. Pain et al. “Direct Reaction Measurements Using GODDESS”. In: *Physics Procedia* 90.Supplement C (2017). Conference on the Application of Accelerators in Research and Industry, CAARI 2016, 30 October – 4 November 2016, Ft. Worth, TX, USA, pp. 455–462. ISSN: 1875-3892. DOI: <https://doi.org/10.1016/j.phpro.2017.09.051>. URL: <http://www.sciencedirect.com/science/article/pii/S1875389217302109>.
- [Pai18a] Steve Pain. Feb. 2018. URL: <https://sites.google.com/a/nuclearemail.org/vikar/home>.
- [Pai18b] Steven Pain et al. *Response to technical review of Exp18001 - 80Ge(d,p)*. 2018.
- [Pai20] Steven Pain. personal communication. 2020.
- [Par07] Richard C. Pardo et al. “Radioactive beams from  $^{252}\text{Cf}$  fission using a gas catcher and an ECR charge breeder at ATLAS”. In: *Nuclear Instruments and Methods in Physics Research Section B: Beam Interactions with Materials and Atoms* 261.1 (2007). The Application of Accelerators in Research and Industry, pp. 965–968. ISSN: 0168-583X. DOI: <https://doi.org/10.1016/j.nimb.2007.04.132>. URL: <http://www.sciencedirect.com/science/article/pii/S0168583X07007501>.
- [Par95] W. E. Parker et al. “Fluctuation effects in radiative capture to unstable final states: A test via the  $^{89}\text{Y}(p\rightarrow,\gamma)$  reaction at  $E_p=19.6$  MeV”. In: *Phys. Rev.*

- C* 52 (1 July 1995), pp. 252–266. DOI: 10.1103/PhysRevC.52.252. URL: <https://link.aps.org/doi/10.1103/PhysRevC.52.252>.
- [Per20] Jorge Pereira. Mar. 2020. URL: <https://wikihost.nsl.msui.edu/S800Doc/doku.php>.
- [Pia17] E. Pian, P. D’Avanzo, and S. et al Benetti. “Spectroscopic identification of r-process nucleosynthesis in a double neutron-star merger”. In: *Nature* 551 (2017), pp. 67–70. DOI: 10.1038/nature24298.
- [Qia03] Y. Z. Qian. “The origin of the heavy elements: Recent progress in the understanding of the r-process”. English (US). In: *Progress in Particle and Nuclear Physics* 50.1 (Jan. 2003), pp. 153–199. ISSN: 0146-6410. DOI: 10.1016/S0146-6410(02)00178-3.
- [Rat19] A. Ratkiewicz et al. “Towards Neutron Capture on Exotic Nuclei: Demonstrating  $(d, p\gamma)$  as a Surrogate Reaction for  $(n, \gamma)$ ”. In: *Phys. Rev. Lett.* 122.5 (2019), p. 052502. DOI: 10.1103/PhysRevLett.122.052502. arXiv: 1812.08887 [nucl-ex].
- [Rau98] T. Rauscher et al. “Dependence of direct neutron capture on nuclear-structure models”. In: *Phys. Rev. C* 57 (4 Apr. 1998), pp. 2031–2039. DOI: 10.1103/PhysRevC.57.2031. URL: <https://link.aps.org/doi/10.1103/PhysRevC.57.2031>.
- [Rol89] Claus E. Rolfs, William S. Rodney, and Donald D. Clayton. “Cauldrons in the Cosmos”. In: *American Journal of Physics* 57.2 (1989), pp. 188–189. DOI: 10.1119/1.16074.

- [Rut19] Ernest Rutherford. *Collisions of alpha Particles with Light Atoms. IV. An Anomalous Effect in Nitrogen*. 1919.
- [Sch12] K. T. Schmitt et al. “Halo Nucleus  $^{11}\text{Be}$ : A Spectroscopic Study via Neutron Transfer”. In: *Phys. Rev. Lett.* 108 (19 May 2012), p. 192701. DOI: 10.1103/PhysRevLett.108.192701. URL: <https://link.aps.org/doi/10.1103/PhysRevLett.108.192701>.
- [Sco16] M Scott. *NSCL Charge-Exchange Group Exchanging charge since 2003*. 2016. URL: [https://groups.nsl.msu.edu/charge\\_exchange/resap.html](https://groups.nsl.msu.edu/charge_exchange/resap.html).
- [Sha00] D. Shapira, T.A. Lewis, and L.D. Hulett. “A fast and accurate position-sensitive timing detector based on secondary electron emission”. In: *Nuclear Instruments and Methods in Physics Research Section A: Accelerators, Spectrometers, Detectors and Associated Equipment* 454.2 (2000), pp. 409–420. ISSN: 0168-9002. DOI: [https://doi.org/10.1016/S0168-9002\(00\)00499-X](https://doi.org/10.1016/S0168-9002(00)00499-X). URL: <http://www.sciencedirect.com/science/article/pii/S016890020000499X>.
- [Sto05] A. Stolz et al. “Production of rare isotope beams with the NSCL fragment separator”. In: *Nuclear Instruments and Methods in Physics Research Section B: Beam Interactions with Materials and Atoms* 241.1 (2005). The Application of Accelerators in Research and Industry, pp. 858–861. ISSN: 0168-583X. DOI: <https://doi.org/10.1016/j.nimb.2005.07.168>. URL: <http://www.sciencedirect.com/science/article/pii/S0168583X0501339X>.
- [Sur14] R. Surman et al. “Sensitivity studies for the weak r process: neutron capture rates”. In: *AIP Advances* 4.4 (2014), p. 041008. DOI: 10.1063/1.4867191.

eprint: <https://doi.org/10.1063/1.4867191>. URL: <https://doi.org/10.1063/1.4867191>.

- [Tho06] Ian Thompson. *FRESCO*. 2006. URL: [www.fresco.org.uk](http://www.fresco.org.uk).
- [Tho07] J. S. Thomas et al. “Single-neutron excitations in neutron-rich  $^{83}\text{Ge}$  and  $^{85}\text{Se}$ ”. In: *Phys. Rev. C* 76 (4 Oct. 2007), p. 044302.
- [Tho09] Ian J. Thompson and Filomena Nunes. *Nuclear reactions for astrophysics: principles, calculation and applications of low-energy reactions*. Cambridge University Press, 2009.
- [Tom11] I. Tomandl et al. “Nuclear structure study of semi-magic  $^{125}\text{Sn}$  via  $(n, \gamma)$  and  $(d, p)$  reactions”. In: *Phys. Rev. C* 83 (4 Apr. 2011), p. 044326. DOI: [10.1103/PhysRevC.83.044326](https://doi.org/10.1103/PhysRevC.83.044326). URL: <https://link.aps.org/doi/10.1103/PhysRevC.83.044326>.
- [Tos19] J. A. Tostevin. *TWOFNR - University of Surrey version*. March 2019. URL: <http://www.nucleartheory.net/NPG/code.htm>.
- [Var91] R.L. Varner et al. “A global nucleon optical model potential”. In: *Physics Reports* 201.2 (1991), pp. 57–119. ISSN: 0370-1573. DOI: [https://doi.org/10.1016/0370-1573\(91\)90039-0](https://doi.org/10.1016/0370-1573(91)90039-0). URL: <http://www.sciencedirect.com/science/article/pii/0370157391900390>.
- [Wal18] David Walter. “Spectroscopic factors near the r-process path using combined measurements:  $^{86}\text{Kr}(d,p)^{87}\text{Kr}$  and  $^{84}\text{Se}(d,p)^{85}\text{Se}$ ”. PhD thesis. Rutgers University, 2018.
- [Wal19] D. Walter et al. “Constraining spectroscopic factors near the  $r$ -process path using combined measurements:  $^{86}\text{Kr}(d, p)^{87}\text{Kr}$ ”. In: *Phys. Rev. C* 99 (5

May 2019), p. 054625. DOI: 10.1103/PhysRevC.99.054625. URL: <https://link.aps.org/doi/10.1103/PhysRevC.99.054625>.

- [Wan05] Shinya Wanajo and Yuhri Ishimaru. “The “weak” r-process in core-collapse supernovae”. In: *From Lithium to Uranium: Elemental Tracers of Early Cosmic Evolution*. Ed. by Vanessa Hill, Patrick Francois, and Francesca Primas. Vol. 228. IAU Symposium. Jan. 2005, pp. 435–438. DOI: 10.1017/S1743921305006174.
- [Woo94] S. E. Woosley et al. “The r-Process and Neutrino-heated Supernova Ejecta”. In: 433 (Sept. 1994), p. 229. DOI: 10.1086/174638.